The WISE Extended Source Catalog (WXSC). I. The 100 Largest Galaxies

T. H. Jarrett[1] , M. E. Cluver[2,3] , M. J. I. Brown[4] , D. A. Dale[5] , C. W. Tsai[6] , and F. Masci[7]

[1] Department of Astronomy, University of Cape Town, Rondebosch, South Africa; tjarrett007@gmail.com
[2] Centre for Astrophysics and Supercomputing, Swinburne University of Technology, John Street, Hawthorn 3122, VIC, Australia
[3] Department of Physics and Astronomy, University of the Western Cape, Robert Sobukwe Road, Bellville 7535, South Africa
[4] School of Physics and Astronomy, Monash University, Clayton 3800, VIC, Australia
[5] Department of Physics and Astronomy, University of Wyoming, Laramie, WY 82071, USA
[6] Department of Physics and Astronomy, University of California, Los Angeles, Los Angeles, CA 90095, USA
[7] Infrared Processing and Analysis Center, California Institute of Technology, Pasadena, CA 91125, USA

Abstract

We present mid-infrared photometry and measured global properties of the 100 largest galaxies in the sky, including the well-studied Magellanic Clouds, Local Group galaxies M31 and M33, the Fornax and Virgo galaxy cluster giants, and many of the most spectacular Messier objects (e.g., M51 and M83). This is the first release of a larger catalog of extended sources as imaged in the mid-infrared, called the *Wide-field Infrared Survey Explorer* (*WISE*) Extended Source Catalog (WXSC). In this study, we measure their global attributes, including integrated flux, surface brightness, and radial distribution. The largest of the large are the LMC, SMC, and Andromeda galaxy, which are also the brightest mid-infrared galaxies in the sky. We interrogate the large galaxies using *WISE* colors, which serve as proxies for four general types of galaxies: bulge-dominated spheroidals, intermediate semi-quiescent disks, star-forming (SF) spirals, and AGN-dominated. The colors reveal a tight "sequence" that spans 5 mag in $W2-W3$ color, ranging from early to late types and low to high SF activity; we fit the functional form given by $(W1 - W2) = [0.015 \times e^{\frac{(W2-W3)}{1.38}}] - 0.08$. Departures from this sequence may reveal nuclear, starburst, and merging events. Physical properties and luminosity attributes are computed, notably the diameter, aggregate stellar mass, and dust-obscured star formation activity. To effectively study and compare these galaxy characteristics, we introduce the "pinwheel" diagram, which depicts physical properties with respect to the median value observed for *WISE* galaxies in the local universe. Utilized with the WXSC, this diagram will delineate between different kinds of galaxies, identifying those with similar star formation and structural properties. Finally, we present the mid-infrared photometry of the 25 brightest globular clusters in the sky, of which many are also the largest and brightest objects orbiting the Milky Way, including Omega Centauri, 47 Tucanae, and a number of famed night-sky targets (e.g., M13).

Unified Astronomy Thesaurus concepts: Infrared galaxies (790); Catalogs (205); Sky surveys (1464); Galaxy evolution (594); Galaxy processes (614)

Supporting material: machine-readable tables

1. Introduction

In the realm of our galactic neighbors, the most appropriate distance scale is megaparsecs. At these vast distances, even the nearest of these *island universes* appears faint and low surface brightness. It has been well on 100 yr since they were first identified as distinct objects beyond the Milky Way. Nevertheless, the nearest spiral galaxies have held fascination for centuries—they were somehow different from the wealth of stars and Galactic nebulae. The observations of M51 by Lord Rosse in the 1840s clearly showed spiral arms, the nucleus, and a companion galaxy, all of which were singularly unique to astronomers at the time.

Galaxies such as Andromeda (M31), Triangulum (M33), the Whirlpool (M51), and the Pinwheel (M101) have been the focus of observations since as least the time of Lord Rosse, possibly earlier by medieval Persian astronomers.[8] Their relatively close proximity, less than 10 Mpc, means they are the largest galaxies in angular appearance. Today, the largest galaxies in the sky are still some of the favorite laboratories to study the internal gas and stellar components, dynamics, and

present and historic star formation, and they are also used to construct local analogs of high-redshift systems.

There are a variety of galaxy types that are local to the Milky Way, and as such, they can be studied with the physical resolutions that are necessary to connect the star formation processes, e.g., cloud collapse at the parsec level, to their environment—the galaxy "main sequence" at two orders larger in scale—to the kiloparsec-scale components such spiral arms, bars, and bulges that represent the "skeleton" of the galaxy. These galaxies are important because they not only offer a window into the workings of these individual galaxies but can also serve as proxies for galaxies in the early universe. The most active galaxy-building epoch was between redshifts of 1 and 3 (e.g., Hopkins & Beacom 2006), but even space telescopes cannot access these systems with the detail and fidelity that is (currently only) possible in the local volume, within 10–20 Mpc. To begin to understand the galaxy "ecosystem," you must first study nearby galaxies.

Since the days of Vesto Slipher and Edwin Hubble, nearby galaxies have been carefully studied using a combination of spectroscopy and imaging to decode their nature. We have a wealth of data on tens of thousands of nearby galaxies, fully articulated in archives such as the NASA Extragalactic

---

[8] Notably Abd Al-Rahman Al-Sufi in his "Book of the Fixed Stars," published in 964 AD.

Database (NED) and Lyon-Meudon Extragalactic Database (HyperLEDA), mostly from optical observations in both photographic (e.g., RC3) and CCD imaging (e.g., Sloan Digital Sky Survey (SDSS)), but also in the last four decades from UV and infrared whole-sky surveys of galaxies (e.g., the *Galaxy Evolution Explorer* (*GALEX*), *Infrared Astronomical Satellite* (*IRAS*), Two Micron All Sky Survey (2MASS), and *Wide-field Infrared Survey Explorer* (*WISE*)). Completing the electromagnetic spectrum from the radio to the gamma-ray, the latest surveys hope to provide new and complementary ways of looking at galaxies and unlocking the complex processes of the baryonic cycle: halo accretion, star formation, feedback, and gigayear secular evolution.

One such survey, the *WISE* (Wright et al. 2010), is well suited to the study of galaxy evolution in general and nearby galaxies in particular. The reason is that *WISE* has imaged the entire 4π sky with relatively uniform breadth and depth. The imaging bands are sensitive to both stellar population and interstellar medium (ISM) processes, which can be used to study the past-to-present star formation history (Jarrett et al. 2013). The ALLWISE catalog (Cutri et al. 2012) and the upcoming CATWISE catalog (Eisenhardt et al. 2019) are optimized for point sources, both for Milky Way stars and for high-redshift galaxies. The *WISE* mission did not make provisions for systematically and properly measuring resolved sources; hence, these catalogs are either incomplete or poorly constructed for nearby and resolved galaxies. We estimate that there are at least 2 million resolved galaxies detected in the *WISE* all-sky imaging, similar to the 2MASS Extended Source Catalog (Jarrett et al. 2000). As such, our mission has been to identify and measure resolved galaxies in the *WISE* imaging. We have carried out a systematic study of nearby galaxies, first introduced in the pilot study by Jarrett et al. (2013), that endeavors to build dedicated mosaics for all resolved galaxies, extract and characterize their measurable attributes, and produce uniform catalogs. For those with redshifts or known distances, their physical (global) attributes are derived, including stellar mass and star formation activity. The overarching project is called the *WISE* Extended Source Catalog (WXSC).

The full-sky coverage of *WISE* means that every galaxy in the sky is imaged (to the sensitivity limits of *WISE*; see below), including the largest and most extended objects. Hence, *WISE* has the unique dual capability of adding ancillary infrared data to any survey or observation while also studying the largest objects in the sky. It is this current study that addresses the latter capability. As a first major release, the largest angular extent galaxies in the sky lead the way, which is appropriate given their historical and contemporary importance to galaxy studies. Subsequent releases of the WXSC will include well-known samples, such as the NGC, UGC, and S^{4}G, as well as new galaxies that may be used to target spectroscopic surveys such as TAIPAN (da Cunha et al. 2016) and SDSS-V (Kollmeier et al. 2017). To date, we have measured and cataloged over 70,000 galaxies in the WXSC.

Inspired by the release of the largest 2MASS galaxies (Jarrett et al. 2003), here we present the angular largest 100 *WISE* galaxies in the sky, which includes most of the Local Group (LG) and many of the most famous Messier objects (M81, M51, M83, M101), as well as "exotic" varieties, the starbursts NGC 253 and M82, and the active galactic nucleus (AGN) systems NGC 1068 (M77) and the Circinus Galaxy. Some of

the WXSC data (mosaics and measurements, including large galaxies) have already been used in recent studies, notably neutral hydrogen studies of NGC 253 (Lucero et al. 2015), M83 (Heald et al. 2016), and M33 (Kam et al. 2017; Elson et al. 2019); multiwavelength studies of NGC 6744 (Yew et al. 2017) and M31 (Tomicic et al. 2019); and baryonic Tully–Fisher studies (Ogle et al. 2019) of moderate-sized samples (e.g., HIPASS) that study star formation–stellar mass relations (Hall et al. 2018) and the star formation–gas connection (Korsaga et al. 2018; Parkash et al. 2018, 2019). A number of studies are currently underway using the WXSC, including a complete census of the Coma and Perseus–Pisces galaxy clusters. One of the most important applications of the WXSC comes from Cluver et al. (2017), who derived a new set of star formation rate (SFR) relations using *WISE* and total infrared luminosities from SINGS (Kennicutt et al. 2003) and KINGFISH (Kennicutt et al. 2011). We will be using these SFR relations to characterize WXSC galaxies.

Here we present a uniform set of mosaics and measurements and derive global properties that may be used to study the local volume of galaxies. We compare the measurements of the 100 largest with a statistically significant sample from the local universe, as compiled in the WXSC, to give context and contrast (if any) to the largest angular-sized galaxies. For completeness, we also provide measurements of LG galaxies that do not satisfy the angular size requirement. Finally, measurements for the largest and brightest (Milky Way) globular clusters (GCs) are also included, since they are both large and bright and require similar photometric methods to extract their global fluxes. We note that this current release of the 100 largest galaxies will be directly followed by the periodic release of WXSC galaxies, whose catalog and data products will be fully described in a second paper, hereafter referred to as Paper II.

This paper is organized as follows. An explanation of source measurements and the data are presented in Section 2. The 100 largest galaxy sample is introduced in Section 3. Source properties, such as coordinates, size, shape, and photometry, are presented in Section 4. We derive global physical attributes for the sample and compare with large WXSC samples to assess the nature of the largest galaxies relative to the local universe in Section 5. In Section 6 we introduce a new way to graphically study the physical attributes, which will be used in future releases. Finally, Section 7 presents the photometric measurements for the brightest GCs.

For galaxies without redshift-independent distances, the cosmology adopted throughout this paper is $H_0 = 70\,\mathrm{km\,s^{-1}\,Mpc^{-1}}$, $\Omega_M = 0.3$, and $\Omega_\Lambda = 0.7$. The conversions between luminosity, distance, and redshift use the analytic formalism of Wickramasinghe & Ukwatta (2010) for a flat, dark energy–dominated universe, assuming standard cosmological values noted above. Length and size comparisons are all carried out within the comoving reference frame. All magnitudes are in the Vega system (*WISE* photometric calibration described in Jarrett et al. 2011). Photometric colors are indicated using band names; e.g., *W1–W2* is the [3.4 μm] $-$[4.6 μm] color. The Vega magnitude-to-flux conversion factors are 309.68, 170.66, 29.05, and 7.871 Jy, respectively, for *W1, W2, W3*, and *W4*. We adopt the new *W4* calibration from Brown et al. (2014a), in which the central wavelength is 22.8 μm (hence, we will refer to *W4* as 23 μm), and the magnitude-to-flux conversion factor is 7.871 Jy. It follows that

the conversions from the Vega system to the monochromatic AB system are 2.67, 3.32, 5.24, and 6.66 mag.

2. *WISE* Imaging and Source Characterization

In this section, we describe the data, imaging products, source characterization, and selection of the largest galaxies. All of the data are derived from the *WISE* mission, notably the level 1 individual frames and the ALLWISE source catalogs (Cutri et al. 2012). Mosaics are constructed from the individual-epoch frames, and source characterization commences with both automated pipelines and expert–user interaction. Measurements are carried out on galaxies, roughly 70,000 to date as part of the WXSC, located in the local universe, $z < 0.3$, including the largest known galaxies. Here we report on the 100 largest in the sky, including four, LMC/SMC and M31/M33, that required special processing due to their extreme angular extent.

2.1. WISE *Mission Details*

WISE is a NASA medium-class explorer mission, launched in 2009 December, featuring a 40 cm primary mirror and 1024×1024 pixel Si:As and HgCdTe solid hydrogen–cooled arrays that simultaneously image in four broad spectral bands (Wright et al. 2010). Simply abbreviated as *W1, W2, W3,* and *W4*, the bands are centered on 3.4, 4.6, 12, and 22 μm in the mid-infrared window, with a *W1* point-source sensitivity that reaches ~25 μJy (5σ; Jarrett et al. 2017). As previously noted, the *W4* band has a filter response that is closer to 23 μm (Brown et al. 2014a); hence, we refer to the central wavelength of the *W4* band as 23 μm. This primary "cryogenic" mission fully covered the sky several times (epochs) before the cryogen was exhausted (pre-2011), after which *WISE* began a new post-cryogen phase in which its two short bands (3.4 and 4.6 μm) continued to map the sky with passive thermal cooling, focusing on asteroid science (read all about NEOWISE at http://wise2.ipac.caltech.edu/docs/release/postcryo/).

2.2. Target Galaxies

Building the WXSC is a multiphase project, starting with known, cataloged galaxies and extending to galaxies in the local universe that are resolved by *WISE*. The former involves targeting specific galaxy catalogs (or samples), and the latter involves "blind" detection and characterization to determine the nature of the object: star, galaxy, or otherwise (Jarrett et al. 2017). For the largest galaxies in the sky, we rely on known catalogs, including the optically based RC3/UGC (Nilsson 1973; de Vaucouleurs et al. 1991) and S^{4}G (Sheth et al. 2010) and the databases NED and LEDA, to extract large galaxies. Additionally, since we are building an infrared catalog, specifically using *W1* (3.4 μm) for the size metric, we include a number of infrared galaxy catalogs (e.g., the *IRAS* Revised Bright Galaxy Sample and 2MASS XSC) to construct an initial sample to make sure we collect all of the largest galaxies.

To date, we have measured over 70,000 nearby galaxies, including discrete LG galaxies that are detected by *WISE*. Source characterization provides the *W1* (3.4 μm) $1 - \sigma_{sky}$ isophotal (~23 mag arcsec^{-2}) size, which is used to identify the 100 largest galaxies. Most of these are "normal" galaxies, but there are also some physically notable examples, from M82 (starburst) to the AGN/Seyferts NGC 1068 (M77) and Circinus

Galaxy. In addition to extragalactic sources, we have measured the brightest (Milky Way) GCs, since they are some of the largest and brightest objects in the sky, with at least one of them, Omega Centauri (NGC 5139), considered to be a stripped dwarf galaxy (e.g., Noyola et al. 2008). We describe the characterization process for GCs below; it is similar to that used for the Magellanic Clouds.

2.3. Mosaic Construction

Owing to the relatively small primary mirror, the *WISE* angular resolution is poor compared to *Spitzer*-IRAC, with ~6″–8″ in the short bandpasses and 12″ in the longest bandpass (Jarrett et al. 2012). It is therefore important to work with native-resolution mosaic images when measuring extragalactic sources, especially those that are resolved. Unfortunately, the public-release "Atlas" imaging from the *WISE* mission does not have native resolution—it was smoothed to primarily benefit point-source detection. Hence, we have constructed new mosaics of all galaxies in the WXSC to have native resolution with a field-of-view size, from arcminutes to degrees, capable of measuring both the target galaxy and its local environment (see Jarrett et al. 2013). There is the added benefit of coadding epochs that were not available during the primary ALLWISE mission, with additional data from NEOWISE (Mainzer et al. 2014) in the *W1* and *W2* bands resulting in deeper, more sensitive photometric imaging.

Mosaics feature resampling with 1″ pixels using a "drizzle" technique developed in the software package ICORE (Masci 2013) specifically designed for *WISE* single-frame images; details of the process and performance can be found in Jarrett et al. (2012). All galaxies have this well-sampled (relative to the beam) 1″ pixel scale, except for the LMC, SMC, and M31: they are too large to practically accommodate the resulting extreme image sizes. The details of these galaxy exceptions and their processing are given below. Depending on the total coverage (and hence depth), the typical $1 - \sigma_{sky}$ surface brightness depths are 23.2, 22.1, 18.4, and 15.8 mag arcsec^{-2} (Vega mags), respectively, for the *W1, W2, W3,* and *W4* bands.

Mosaic construction is relatively straightforward for most galaxies. There are some cases that require extra attention, including the highest surface brightness objects, specifically, M82, NGC 253, Circinus, NGC 1068, and NGC 2070 (see below), as well as some of the GCs, all saturated at their cores, notably in the longest bands of *WISE*. Recovery of the lost information was carried out using a technique developed for *Spitzer*-IRAC/MIPS image saturation (by the first author of this paper; see also the IRAC instrument handbooks[9] for more detail), which entails utilizing the point-spread function (PSF) and super-resolution image construction (Jarrett et al. 2012) to recover the core information. The method was utilized successfully for these cases; nevertheless, the resulting core flux has a large uncertainty, 20%–30%, which translates to an extra 3%–5% uncertainty for the global flux.

In addition to the images, which include the signal, uncertainty, and coverage maps per band, we also construct PSFs that are used for star removal (see below).

---

[9] https://irsa.ipac.caltech.edu/data/SPITZER/docs/irac/iracinstrumenth andbook/

2.4. Source Characterization

The goal of source characterization is to extract global parameters and "reduce" an image (or, in this case, four multi-λ images) to a set of standard metrics that can be used to study the nature of the target galaxy. The most important parameters are the integrated flux (or brightness), size and shape (inclination for disk galaxies), surface brightness, and cross-band flux ratios (i.e., colors). There are many other parameters that are measured and cataloged (e.g., nuclear concentration) but otherwise not discussed here; details will be given in Paper II. The basic source characterization pipeline has a heritage that extends from the 2MASS Extended Source Catalog (Jarrett et al. 2000), also used in the *WISE* processing pipeline, and various aspects have been discussed in previous *WISE* work (Jarrett et al. 2011, 2013, 2017; Cluver et al. 2014, 2017). Below, we add some additional detail relevant to large galaxies.

One of the most important first steps is to identify and remove foreground Galactic stars so as not to contaminate the galaxy measurements. This is particularly important for *W1* and *W2*, which are filled with foreground Milky Way stars; hence, particular attention is given to the *W1* and *W2* star-cleaning process. We identify stars using the ALLWISE catalog (Cutri et al. 2012), which has basic point-source characterization, the most important being the fluxes, colors, and profile metrics—notably, the reduced $\chi^2_{\rm reduced}$, which provides an assessment of the point or resolved nature of the object. We use a combination of the source colors and pointlike characteristics to decide if the source should be removed from the image—that is to say, if the source is foreground or associated with the target galaxy.

We have found that sources that are resolved (i.e., galaxies, in most cases) have a *W1* $\chi^2_{\rm reduced}$ value greater than 2 (Jarrett et al. 2011, 2017; Cluver et al. 2014). We use this metric to assess if the source is pointlike (i.e., Galactic star or background distant galaxy) or resolved. If resolved, it may be a piece of the target galaxy (e.g., H II region), in which case we may not want to remove it, especially if it is located on a spiral arm or within the disk, or it may be a blend of two or three stars, necessitating its removal from the cleaned image. An even more powerful discriminant is the *W2*–*W3* color, which is relatively "blue" (low value) for Galactic stars compared to extragalactic sources or star-forming (SF) regions in the target galaxies. In this way, we avoid shredding our target galaxies into multiple pieces, which can be a real challenge for large imaging surveys and automated source extraction. Moreover, and crucially, we visually inspect every galaxy to make sure that stars have been properly identified and removed and that the inverse, shredding, has not occurred in any band. In the case of faint to moderately bright sources, *W1* $\sim$ 15 mag (0.3 mJy), stars are removed from the images by PSF subtraction, and for bright stars, we use a masking process in which pixels are then recovered using the local background. As noted, visual inspection and human intervention are used for difficult cases, especially with source crowding and bright nearby stars, and for overall validation.

Once stars have been removed, the next step is to determine the local background value, which is an iterative—curve of growth, flux convergence—process such that the local background is determined in a centered elliptical annulus whose inner and outer radii are safely (30%–50%) beyond the light coming from the target galaxy. Stars are excluded from the distribution through subtraction and masking. Using the same method as that developed for *WISE* point-source processing, the local background is derived from a mean centered about the pixel value distribution mode of the annulus pixel values (previously cleaned of foreground stars). The rms uncertainty ($\sigma_{\rm sky}$) of this background value is computed from the width of the distribution, as described in the *WISE* Explanatory Supplement (Cutri et al. 2012). For nearly all cases, a simple offset is all that is needed to removed the background emission, but in the case of M31, a tilted plane was used to account for the slight background light gradient (orthogonal to the Galactic latitude axis) across the enormous field area, over 25 deg^2.

The local background, or sky value, is subtracted from the star-cleaned mosaics, and the primary source characterization is then carried out. Shape characterization is derived from the $3 - \sigma_{\rm sky}$ elliptical isophote and held fixed for all measurements; i.e., the source is assumed to be elliptical and axisymmetric. The maximum extent of the galaxy is determined at the $1 - \sigma_{\rm sky}$ elliptical isophote, which then represents the isophotal aperture for integrated flux measurements. The total light, however, is estimated using larger apertures (approaching the asymptotic limit) and by first constructing the radial surface brightness distribution, fitting a double Sérsic function, and extrapolating the extent of the galaxy to three disk scale lengths (based on the Sérsic scale lengths). The resulting "extrapolation" flux represents the "total" flux, although it is not much more (5%–10%) than the isophotal flux, and agrees very well (1%–2%) with the asymptotic flux in most cases; details are in Section 4.1. Finally, integrating radially from the center until 50% of the integrated light is reached, the half-light (or effective) radius and surface brightness are then derived from the total flux.

These are the basic steps that are used to measure resolved galaxies. However, there are four notable exceptions that require further explanation: M31, M33, LMC, and SMC, given below.

2.5. Magellanic Clouds

With the Magellanic Clouds, our challenging aim was to construct a mosaic large enough to encompass both galaxies, thereby revealing the bridge region between them. The LMC and SMC encompass a region of the sky that is $\sim$35° across, mostly along the equatorial axis. This is far too large to accommodate 1″ pixels, and given our primary goal of measuring the global properties of the Clouds, we did not require heavy oversampling. Consequently, we chose a pixel scale that was comparable to the resolution of *WISE*, specifically, 8″ pixels.

The resulting images (four bands) are 18,501 × 10,001 pixels, constructed with an equatorial projection (a galactic projection is not all that different) with the LMC to the east and the SMC to the west. Artifacts from bright stars in the images are manually removed, and the *WISE* bands are combined to form a four-color panorama of the region; see Figure 1. The depth of the images is relatively high for *WISE* because of the proximity to the south ecliptic pole; the resulting high coverage ($>$100 epochs, on average) is good for optimal sensitivity, but the source confusion in *W1* is reaching its peak (explored in detail by Jarrett et al. 2011). So although the longward bands, *W3* and *W4*, have excellent sensitivity in this region, the short bands of *W1* and *W2* are reaching diminishing returns with confusion noise.
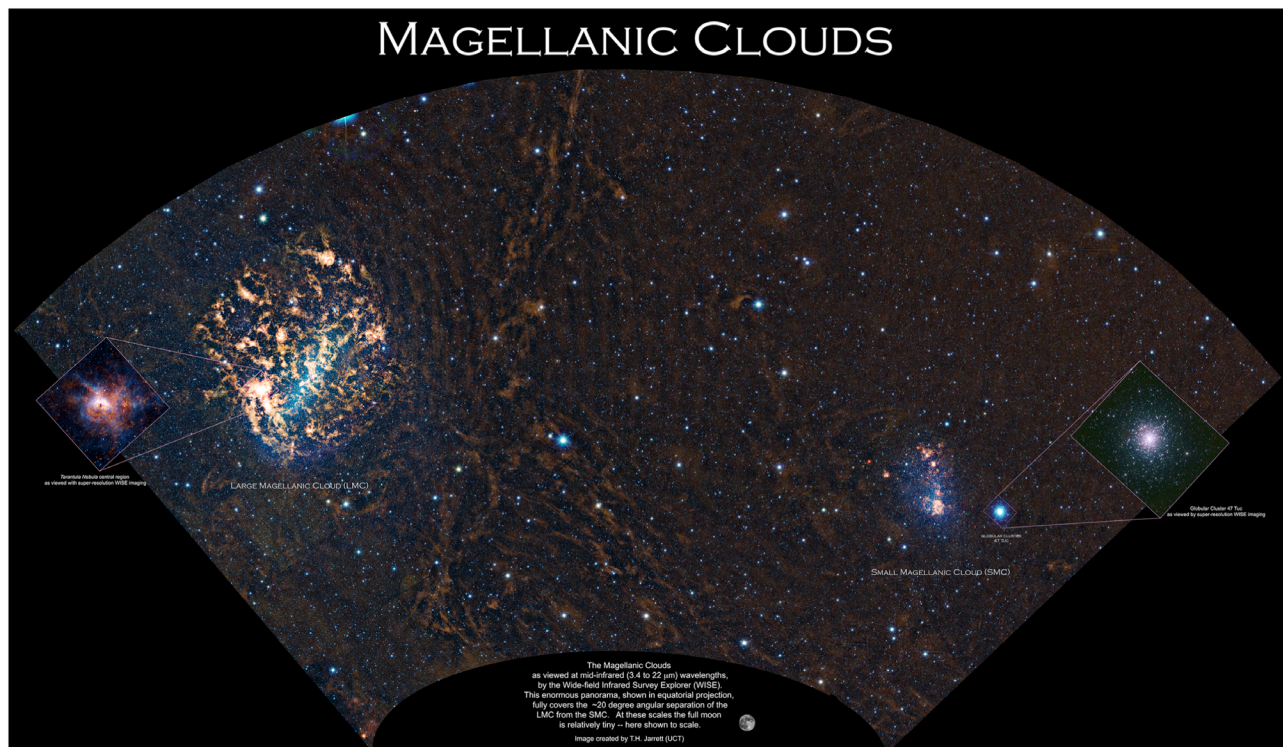
Figure 1. Mid-infrared four-color panorama of the Magellanic Clouds, constructed from *WISE* imaging. This equatorial projection fully covers the $>20°$ separation between the LMC and the SMC. The insets show *WISE* super-resolution mosaics of the Tarantula Nebula (30 Dor) in the LMC and the GC 47 Tuc adjacent to the SMC. Note the long stream of nebulosity running north–south between the clouds; this is real emission, likely associated with the tidal interaction between the Clouds and the Milky Way.

The LMC is graced by the star formation complex 30 Doradus (aka the Tarantula Nebula), which is both spectacular and supremely bright in the mid-infrared, so much so that the central star cluster (NGC 2070) saturates in all four *WISE* bands. The multiple-core saturation was rectified (see Section 2.3), and the restored super-resolution image is shown in Figure 1, with the inset image on the east side. On the west side, the SMC is shadowed by the magnificent GC 47 Tucanae, which was also saturated in the core (*W1* only) and restored using the PSF and super-resolution; see the inset figure showing 47 Tuc.

Source characterization for the Magellanic Clouds is carried out on the large mosaics. Since both objects are large in angular extent compared to the field of Galactic stars, it is not practical to identify stars within the Clouds that may or may not belong to the Milky Way. This is also the case for M31, M33, and, worst case, GCs, since member stars look just like foreground Galactic stars. Hence, we employ a technique developed for measuring GCs in 2MASS (Jarrett et al. 2003), whereby the mean flux of the foreground Galactic stars is measured and subtracted from the target galaxy. The assumption is that the mean flux (per pixel) of the starlight as measured in a patch of sky (annulus centered on the target galaxy) is the same as that within the galaxy. This is statistically robust for faint stars, but clearly there can be fluctuations from bright stars. To minimize this deleterious effect, we identify bright Milky Way stars contained in the ALLWISE catalog from both the target and the sky patch and remove them before statistical measurements are taken.

In the infrared, the LMC displays the well-known stellar bar (appearing blue and elliptical in Figure 1), but it also appears strangely square or "blocky" in the ISM bands. This is not an

artifact of the *WISE* imaging; it is real and can also be seen in the large *Spitzer*-SAGE mosaics of the LMC (Meixner et al. 2006) and in *IRAS* 60 μm dust maps. To measure the global flux of the LMC, we have chosen to use a circular aperture (for simplicity) that fully covers the LMC, extending $10°$ in diameter, encompassing the bar (seen in *W1* and *W2*) and the star formation regions (*W3* and *W4*). For the sky patch, we choose a region that is equally between the LMC and the SMC so that we can use the same mean stellar "sky" flux for both clouds. The sky region is centered on $(03:00:45, -71:42:10)$ and has a radius of $4°.5$. The resulting Galactic foreground mean surface brightness is 21.62, 21.38, 20.41, and 19.10 mag arcsec^{-2} (Vega system) for the sky patch (*W1, W2, W3,* and *W4*, respectively), which is then subtracted from the surface brightness of each pixel in the LMC and SMC.

One final note of interest with the big mosaic: there is a "river" of emission extending from north to south, west of the LMC, that appears to terminate in the Chameleon II SF complex of the Milky Way. It is notably bright in *W3* (hence, orange-reddish in the adopted Figure 1 color scheme), which would suggest that the emission arises from warm dust and polycyclic aromatic hydrocarbon (PAH) emission in the bridge region, or possibly a closer projection from the Milky Way itself. Although you can clearly see "ringing" artifact features throughout this large mosaic of the Magellanic clouds, the north–south filament is in fact real. You can see the exact correspondence in deep optical imaging (Besla et al. 2016; using a wide-field luminance filter imaging), *IRAS* maps, the so-called Galactic cirrus filaments—perfectly consistent with *WISE* 12 μm imaging—and even Planck 353 GHz polarization maps The large-scale feature may be related to the tidal interaction between the Clouds and the Milky Way or simply a
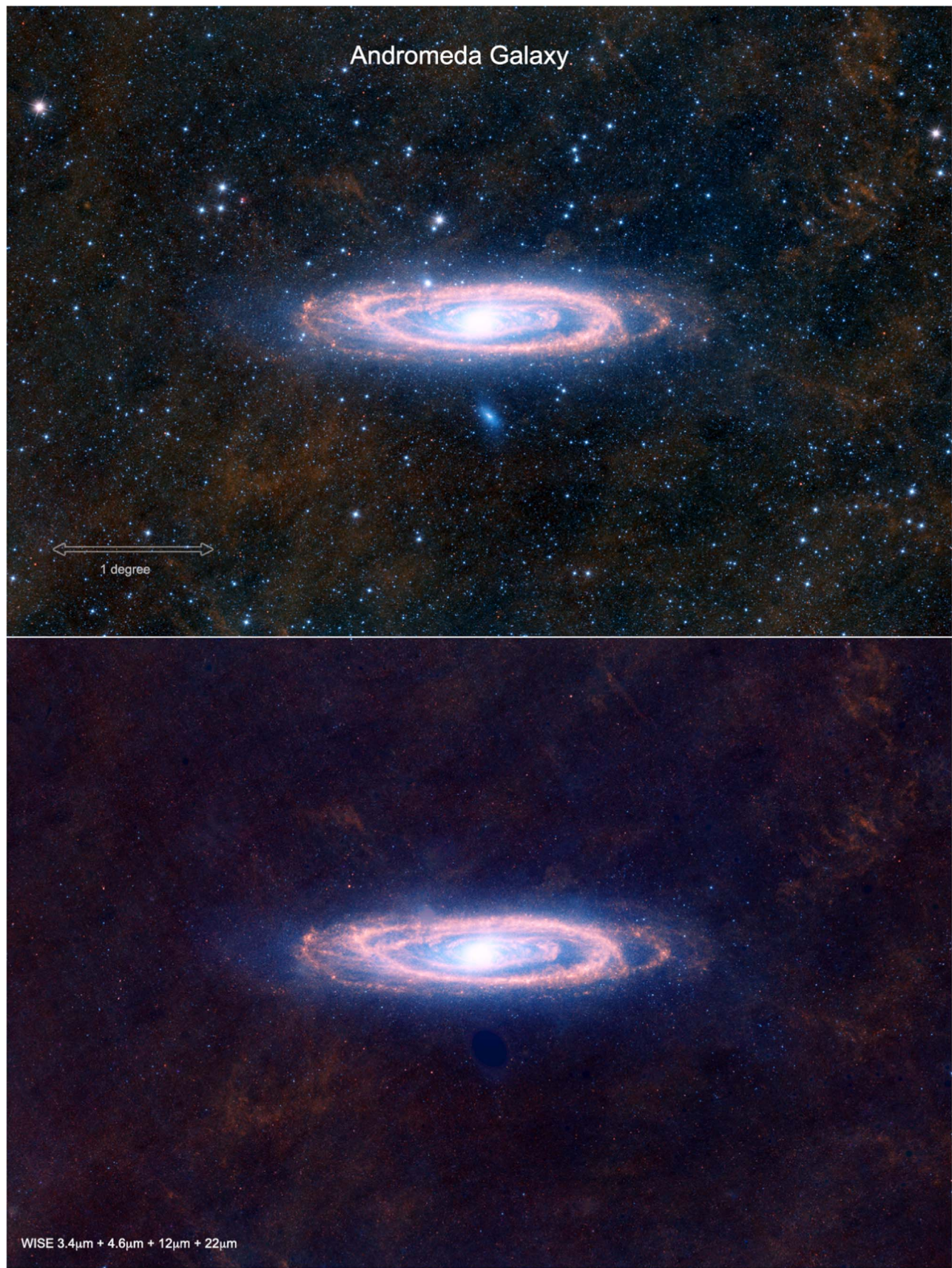
Figure 2. *WISE* four-color view of the Andromeda (M31) galaxy, projected in the ecliptic (spacecraft) orientation. The top panel shows the galaxy, its satellite galaxies (M32 and M110), and foreground Galactic stars, while the bottom panel shows only the galaxy, with stars and satellites removed. The outstanding feature with the infrared is that spiral arms embedded with molecular clouds and SF activity are in emission, as compared to absorption at optical wavelengths.

nearby magnetic field–collimated dust filament that is unrelated to the Magellanic Clouds. In any case, it is a very interesting feature for further investigation.

2.6. M31 and M33

The extreme angular size of M31 and M33 required using a larger pixel scale (to conserve CPU memory, for example); here we construct with 1″5 pixels. The necessary angular extent of the images was first estimated by using the *W1* stellar number density from the ALLWISE catalog, computed in shells that extended from the center of M31 out to large radii. In close proximity to M31, the number density is high, while at large radii, the value settles to the Milky Way mean value corresponding to about 3° from the center of M31 (Chauke 2013). In this way, we determined that a 6° mosaic of M31 would be sufficient to measure the galaxy in the *WISE* bands; although M31 may yet extend beyond this range, we are not able to measure it relative to the field outside a radius of approximately 3°. Moreover, since M31 is fairly inclined and its orientation is diagonal in equatorial projection, we decided to construct the mosaic in *WISE* spacecraft mapping orientation (ecliptic). In this way, the M31 disk appears horizontal, which is the optimal projection for minimizing the size of the required mosaic. In the case of M33, since the galaxy is not nearly as large, we used the standard equatorial projection with a 2° extension along the north–south axis.

It is not as straightforward to identify foreground Galactic stars from actual M31 sources due to the angular size of M31 and the large foreground Galactic population (the center of M31 is located at Galactic coordinates $l = 121°2$, $b = -21°6$). The method we developed was part of a Masters dissertation (Chauke 2013), and it uses a combination of the stellar number density, proximity to the M31 disk, and photometric properties of the ALLWISE sources to determine the nature of the source. It is a statistical method that determines the likelihood that a source belongs to M31 or the Milky Way. For example, well beyond the nucleus of M31, $>2°7$, the field is completely dominated by Galactic stars, and the *W1* star counts and colors (*W1*–*W2*, *W2*–*W3*) have a signature of the Galactic population at the longitude and latitude of M31. In closer proximity to the disk of M31, the source counts rise and the photometric properties begin to change; e.g., more faint stars are seen from M31 itself, and the colors redden because the K/M-giant populations are the only extragalactic stars detected because of the distance of M31 relative to Milky Way stars. Hence, evolved and luminous stars appear much fainter (the distance modulus of M31 is about 24 mag). Exploiting these differences, we determine the most likely Galactic foreground population, which is then removed from the M31 cleaned mosaic.

The total number of foreground stars within the influence of M31 is impressive: in an 11 deg^2 region centered on M31, over 100,000 foreground stars are identified. We should note that near the nuclear bulge of M31, the density of sources is so high that confusion and crowding render any source identification impossible, and Galactic stars will remain in the bulge region. Nevertheless, this is a relatively small area, and the estimated flux of the total number of Galactic sources in the bulge is still less than 1% of the total flux of M31 itself. So, with the sources that are identified as Galactic, they are removed from the image using the techniques of PSF and area masking, described earlier. The resulting mosaic of M31 is shown in Figure 2.

The same statistical method for star identification is used for M33, although it is not as challenging, since M33 is considerably smaller ($\sim$1/3) relative to M31 and is located further from the Galactic plane (coordinates: $l = 133°6$, $b = -31°3$). Crowding is also much less of a problem, as M33 has a weak stellar bulge. The cleaned mosaic of M33 is shown in Figure 3.

3. The Largest Galaxies in the Sky

We choose as the primary metric for angular size the *WISE W1* (3.4 μm) $1\sigma_{sky}$ isophotal radius (that is, the semimajor axis of the disk or triaxial stellar distribution). The *W1* spectral window is sensitive to starlight from evolved stars, characterized by the stellar "bump" that peaks in the *H* band (1.6 μm) and extends into the mid-infrared through the Rayleigh–Jeans (R-J) tail. Similar to using the *K* band (2.2 μm) as a tracer of the host galaxy stellar mass, the *W1* band has been shown to be an excellent proxy for the stellar component of the baryonic mass (Jarrett et al. 2013; Cluver et al. 2014; Meidt et al. 2014; Ponomareva et al. 2017; Hall et al. 2018; Kettlety et al. 2018).

In terms of surface brightness, *WISE* is relatively sensitive because it is space-based and has large native pixels (2″5). Consequently, in the *W1* band, the typical rms per pixel is about 23 mag arcsec^{-2} (Vega), and faint depths are reached with axisymmetry typically averaging 25 (Vega) or $\sim$28 mag arcsec^{-2} (AB), similar to those achieved with S^{4}G's *Spitzer*-IRAC (Sheth et al. 2010). These depths are considerably fainter than those of the K_s band in 2MASS, which typically reaches 20 mag arcsec^{-2}, so *W1* has much larger radii, ranging from two to five times larger than those measured by the 2MASS K_s band (Cluver et al. 2014). Moreover, as will be shown below, the "total" integrated flux in the *W1* channel is 95% contained within the isophotal aperture; hence, the *W1* $1 - \sigma_{sky}$ isophote is both robustly measured and a good tracer of the size and mass of the galaxy.

Based on the *WISE W1* angular radius, we present the largest 100 galaxies in the sky in Table 1. The table is sorted by isophotal radius and includes the Hubble type, axis ratio (b/a), position angle orientation (east of north), and integrated fluxes, quoted in flux density and Vega magnitudes. These parameters represent only a small subset of the full characterization that is completed for each galaxy (e.g., surface brightnesses, total fluxes, etc.). These additional data will be made available online with the full WXSC data release.

Not surprisingly, the largest galaxies in the sky are the Magellanic Clouds (Figure 1), followed by the other LG galaxies M31 and M33 (Figures 2 and 3). These galaxies have extents that can be measured in degrees, whereas the remaining galaxies in the universe have sizes in the arcminute and arcsecond range. We should note that it is challenging to measure the actual extent of these galaxies due to their sheer size relative to the imaging focal plane that they are measured with, thus requiring extremely large mosaic constructions. Moreover, in the case of the Magellanic Clouds, they do not have well-defined shapes; the LMC has an elliptical bar and a squarish ISM (see Figure 1), while the SMC is irregular in shape and extent. Hence, the infrared size quoted here, 10° diameter for the LMC and 5°6 for the SMC, has considerable uncertainty, $>$10%.

The general galaxy properties and measured photometry are listed in Table 1. The first column (iS) indicates the radial size order, and the second column (iB) is the order based on the *W1*
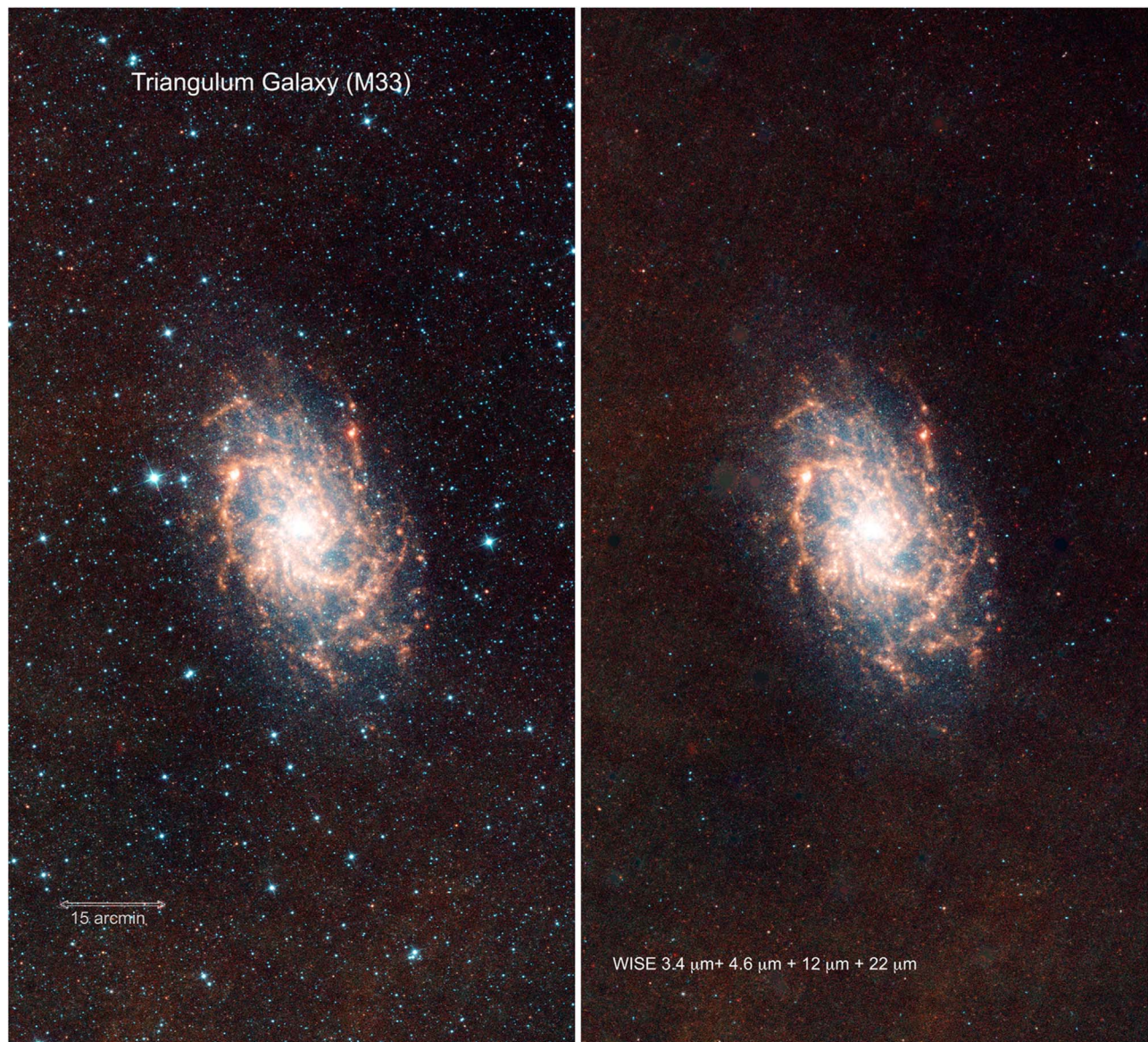
Figure 3. *WISE* four-color view of the Triangulum (M33) galaxy. The left panel shows the galaxy and foreground Galactic stars, while the right panel shows only the galaxy. Because it is relatively face-on and presents parsec-scale SF regions for an entire range of spiral arm radii and environments, M33 is one of the best targets in the sky to study.

integrated flux. The rank of the radius and integrated brightness correlates, as shown in Figures 5 and 6. The LMC is the brightest galaxy in the sky in terms of its integrated flux: 1828, 1064, 2377, and 5728 Jy, respectively, for the four bands of *WISE*. Next is Andromeda: 285, 152, 175, and 143 Jy, which just edges that of the SMC. Both of the Magellanic Clouds have larger *W4* fluxes due to their current star formation (see Section 5.4).

Besides the famed LG galaxies, the largest galaxies include many that are well studied, including the local starburst NGC 253 (5), Centaurus A (6), M101 (the Pinwheel; 9), NGC 1316 (Fornax A; 12), the Sombrero (17), Virgo A (21), the LG dwarf NGC 6822 (25), M83 (Southern Pinwheel; 27), M51 (Whirlpool; 42), the Fireworks (49), knife-edge NGC 5907 (63), the Seyfert galaxy Circinus (75) located behind the Milky Way, the starburst M82 (83), and, spectacularly, NGC 1068 (M77; 85), to name just a few. Some

of the largest-extent galaxies are not all that bright (e.g., the local dwarfs); correspondingly, some of the brightest galaxies are not in this list of large galaxies. If we only consider the SF bands of *W3* and *W4*, compact LIRGs would make the list of the top 100, such as Arp 220.

A large fraction of the LG galaxies appear in the list; however, a few notable ones are too small or faint in surface brightness to detect in angular extent. Hence, for completeness, we include the LG galaxies that *WISE* is able to detect and measure; note that many of the tiny and diffuse dwarf galaxies are not in play here. Table 1, at the bottom, includes IC 1613, M32, UGC 5373, and ESO 245-007 (Phoenix Dwarf).

In the following sections, we compare the properties of the largest galaxies, including their derived physical properties (size, mass, and star formation). For context, we also consider their mass and star formation properties relative to a large spectroscopic survey of local universe galaxies (Jarrett et al. 2017).

Table 1
Photometry of the 100 Largest Galaxies Imaged by *WISE*

iS	iB	Galaxy	R.A. (deg)	Decl. (deg)	Morph.	b/a PA	R_{W1} (arcmin)	$m1 \pm \Delta m1$ (mag)	R_{W2} (arcmin)	$m2 \pm \Delta m2$ (mag)	R_{W3} (arcmin)	$m3 \pm \Delta m3$ (mag)	R_{W4} (arcmin)	$m4 \pm \Delta m4$ (mag)
(1)	(2)	(3)	(4)	(5)	(6)	(7)	(8)	(9)	(10)	(11)	(12)	(13)	14	(15)
1	1	LMC	79.64101	−68.81836	SBm	1.00 0.0	300.00	−1.93 0.01	300.00	−1.99 0.01	300.00	−4.78 0.05	300.00	−7.15 0.05
2	3	SMC	13.18660	−72.82860	SBm-pec	1.00 0.0	166.67	0.56 0.01	166.67	0.62 0.01	166.67	−0.93 0.01	166.67	−3.48 0.01
3	2	M31	10.68479	41.26907	Sb	0.35 37.3	111.44	0.08 0.01	111.44	0.13 0.01	111.44	−1.95 0.01	111.44	−3.09 0.01
4	5	M33	23.46204	30.66022	Sc	0.59 18.9	31.64	3.09 0.01	31.64	3.02 0.01	31.64	−0.17 0.01	31.64	−1.94 0.01
5	6	NGC 0253	11.88844	−25.28827	SABc	0.28 53.0	21.13	3.46 0.01	21.13	3.27 0.01	21.13	−0.54 0.04	21.13	−2.94 0.04
6	4	NGC 5128	201.36481	−43.01954	S0	0.77 33.8	19.64	3.01 0.01	19.64	2.98 0.01	19.64	0.45 0.01	19.64	−1.25 0.01
7	36	NGC 0055	3.72192	−39.19775	SBm	0.19 108.9	19.49	5.45 0.01	19.49	5.36 0.01	19.49	2.80 0.01	19.49	0.29 0.01
8	7	M81	148.88837	69.06528	Sab	0.56 156.7	14.67	3.60 0.01	14.67	3.61 0.01	14.67	1.84 0.03	14.67	0.45 0.03
9	27	M101	210.80225	54.34893	SABc	0.92 33.3	14.50	5.22 0.01	14.50	5.10 0.01	14.50	1.62 0.01	14.50	−0.28 0.01
10	12	NGC 4945	196.36409	−49.46816	SBc	0.37 43.4	12.98	4.07 0.01	12.98	3.87 0.01	12.98	0.31 0.01	12.98	−1.56 0.01
11	10	IC 0342	56.70144	68.09635	SABcd	0.95 75.5	12.98	3.97 0.01	12.98	3.89 0.01	12.98	0.23 0.01	12.98	−1.81 0.01
12	23	NGC 1316	50.67380	−37.20796	S0	0.64 34.7	12.82	5.08 0.01	10.03	5.14 0.01	3.38	4.49 0.01	3.38	3.24 0.02
13	20	M49	187.44489	8.00050	E	0.77 152.0	12.75	4.95 0.01	9.73	5.08 0.01	2.58	4.82 0.01	2.58	3.92 0.03
14	37	M86	186.54897	12.94619	E	0.62 127.2	11.88	5.48 0.01	9.05	5.58 0.01	1.74	5.96 0.01	1.74	5.10 0.05
15	9	Maffei 1	39.14779	59.65487	E-S0	0.77 89.3	11.54	3.94 0.01	10.33	3.96 0.02	1.74	4.18 0.01	2.12	2.80 0.01
16	31	M110	10.09197	41.68548	E	0.50 168.2	11.36	5.32 0.01	10.10	5.41 0.01	10.10	4.65 0.02	10.10	3.34 0.06
17	16	M104	189.99765	−11.62305	Sa	0.46 90.7	11.04	4.62 0.01	9.28	4.66 0.01	3.67	3.74 0.01	3.67	2.57 0.02
18	43	NGC 2403	114.20885	65.60103	SABc	0.53 124.1	10.94	5.69 0.01	10.94	5.59 0.01	10.94	2.26 0.01	10.94	0.28 0.01
19	99	NGC 0247	11.78529	−20.76036	SABc	0.30 171.9	10.90	6.49 0.01	10.90	6.52 0.01	10.90	4.06 0.01	10.90	2.28 0.02
20	28	M106	184.73955	47.30408	Sbc	0.46 152.0	10.67	5.23 0.01	10.67	5.19 0.01	10.67	2.75 0.01	10.67	1.09 0.01
21	30	M87	187.70593	12.39113	E	0.79 152.9	10.37	5.32 0.01	6.88	5.46 0.01	1.86	5.14 0.01	1.86	3.84 0.02
22	48	NGC 3628	170.07085	13.58912	SBb	0.23 105.1	10.20	5.76 0.01	8.24	5.64 0.01	8.24	2.44 0.01	8.24	0.51 0.01
23	46	NGC 0300	13.72251	−37.68413	Scd	0.77 123.2	10.03	5.73 0.01	10.03	5.73 0.01	10.03	3.13 0.01	10.03	1.28 0.02
24	18	NGC 4736	192.72110	41.12020	SABa	0.89 105.6	9.64	4.77 0.01	7.19	4.78 0.01	7.19	2.03 0.01	7.19	0.32 0.01
25	51	NGC 6822	296.24115	−14.80224	IBm	0.82 20.5	9.53	5.80 0.01	9.53	5.80 0.01	9.53	3.50 0.01	9.53	1.20 0.02
26	90	NGC 1532	63.01807	−32.87421	SBb	0.24 32.2	9.44	6.43 0.01	7.40	6.41 0.01	7.40	3.61 0.01	7.40	2.00 0.01
27	13	NGC 5236	204.25296	−29.86598	Sc	0.95 161.4	9.33	4.24 0.01	9.33	4.12 0.01	9.33	0.32 0.01	9.33	−1.86 0.01
28	109	NGC 0147	8.30052	48.50901	E	0.57 28.7	9.28	6.57 0.01	7.52	6.69 0.01	7.52	4.84 0.01	Null	Null Null
29	38	NGC 6744	287.44211	−63.85751	Sbc	0.70 11.9	9.14	5.49 0.01	9.14	5.47 0.01	9.14	2.27 0.01	9.14	0.68 0.01
30	29	M63	198.95549	42.02931	Sbc	0.60 103.4	8.73	5.26 0.01	8.73	5.20 0.01	8.73	1.88 0.01	8.73	0.25 0.01
31	54	NGC 1553	64.04361	−55.78003	S0	0.79 153.1	8.70	5.89 0.01	6.21	6.00 0.01	2.25	5.38 0.01	2.25	4.27 0.02
32	52	NGC 1399	54.62093	−35.45040	E1pec	0.85 78.0	8.66	5.82 0.01	6.73	5.94 0.01	2.05	5.71 0.01	2.05	4.86 0.04
33	533	NGC 4236	184.17477	69.46757	SBdm	0.30 158.0	8.66	7.91 0.01	8.66	7.99 0.01	8.66	5.97 0.02	8.66	3.09 0.03
34	47	NGC 4565	189.08658	25.98755	Sb	0.19 136.3	8.54	5.76 0.01	8.54	5.71 0.01	8.54	3.21 0.01	8.54	1.66 0.01
35	17	Maffei 2	40.47926	59.60422	Sbc	0.44 27.7	8.50	4.76 0.01	8.50	4.58 0.01	8.50	1.07 0.01	8.50	−1.03 0.01
36	60	NGC 4631	190.53334	32.54174	SBcd	0.27 83.2	8.27	6.01 0.01	8.27	5.80 0.01	8.27	1.99 0.01	8.27	−0.06 0.01
37	33	M60	190.91643	11.55272	E	0.82 99.3	8.23	5.38 0.01	6.28	5.47 0.01	2.17	5.04 0.01	2.17	3.98 0.04
38	65	NGC 4636	190.70770	2.68779	E	0.68 147.7	8.06	6.07 0.01	6.45	6.17 0.01	1.65	6.17 0.01	1.65	4.95 0.05
39	142	NGC 2768	137.90607	60.03756	E	0.32 91.7	7.98	6.76 0.01	5.89	6.83 0.01	1.80	6.67 0.01	1.80	5.62 0.06
40	77	NGC 3585	168.32115	−26.75477	E	0.57 109.0	7.94	6.28 0.01	5.76	6.40 0.01	1.34	6.30 0.01	1.34	5.35 0.06
41	1151	ESO 270-G017	203.70584	−45.54919	SBm	0.18 107.5	7.94	8.55 0.01	6.05	8.72 0.01	6.05	6.27 0.02	6.05	3.98 0.03
42	24	M51a	202.46959	47.19518	SABb	0.67 17.6	7.72	5.09 0.01	7.72	4.97 0.01	7.72	1.19 0.01	7.72	−0.61 0.01
43	41	NGC 3115	151.30800	−7.71870	E-S0	0.56 41.7	7.69	5.59 0.01	5.65	5.64 0.01	1.57	5.47 0.01	1.57	4.61 0.03
44	56	NGC 3923	177.75705	−28.80606	E	0.88 40.6	7.66	5.98 0.01	5.89	6.12 0.01	1.32	6.15 0.01	1.32	5.33 0.06
45	76	NGC 4365	186.11780	7.31775	E	0.68 35.6	7.53	6.27 0.01	5.48	6.44 0.01	0.85	6.86 0.01	0.85	5.82 0.05
46	136	NGC 1313	49.56689	−66.49796	SBcd	0.63 173.3	7.47	6.71 0.01	7.47	6.64 0.01	7.47	3.51 0.01	7.47	1.03 0.01

Table 1
(Continued)

iS	iB	Galaxy	R.A. (deg)	Decl. (deg)	Morph.	b/a PA	R_{W1} (arcmin)	$m1 \pm \Delta m1$ (mag)	R_{W2} (arcmin)	$m2 \pm \Delta m2$ (mag)	R_{W3} (arcmin)	$m3 \pm \Delta m3$ (mag)	R_{W4} (arcmin)	$m4 \pm \Delta m4$ (mag)
(1)	(2)	(3)	(4)	(5)	(6)	(7)	(8)	(9)	(10)	(11)	(12)	(13)	14	(15)
47	45	M84	186.26555	12.88707	E	0.97 16.3	7.46	5.73 0.01	5.50	5.82 0.01	1.31	5.81 0.01	1.31	4.87 0.05
48	72	NGC 0185	9.74029	48.33795	E	0.74 49.0	7.45	6.23 0.01	5.81	6.34 0.01	2.06	5.52 0.01	2.06	4.65 0.04
49	21	NGC 6946	308.71796	60.15392	SABc	0.91 51.5	7.45	5.01 0.01	7.45	4.84 0.01	7.45	0.94 0.01	7.45	−1.04 0.01
50	93	NGC 1395	54.62383	−23.02732	E	0.81 146.5	7.42	6.45 0.01	5.63	6.57 0.01	1.32	6.41 0.01	1.32	5.47 0.07
51	25	IC 0010	5.07196	59.30388	IBm	0.87 125.8	7.33	5.11 0.01	7.00	5.04 0.01	3.87	2.35 0.01	3.87	−0.33 0.01
52	206	NGC 4517	188.18965	0.11525	Sc	0.18 81.9	7.22	7.08 0.01	7.22	6.99 0.01	7.22	3.91 0.01	7.22	2.11 0.01
53	32	NGC 1291	49.32742	−41.10804	S0-a	0.98 44.7	7.22	5.35 0.01	7.22	5.39 0.01	7.22	4.30 0.01	7.22	3.10 0.04
54	67	NGC 2683	133.17226	33.42194	Sb	0.19 42.0	7.16	6.14 0.01	6.26	6.10 0.01	6.26	3.79 0.01	6.26	2.65 0.02
55	59	NGC 4697	192.14961	−5.80060	E	0.81 49.9	7.13	6.00 0.01	5.27	6.10 0.01	1.32	6.02 0.01	1.32	4.81 0.04
56	35	NGC 3521	166.45242	−0.03587	SABb	0.62 165.4	7.13	5.44 0.01	4.93	5.38 0.01	4.93	1.98 0.01	4.93	0.33 0.01
57	598	NGC 3109	150.79233	−26.16096	SBm	0.31 91.7	7.09	8.00 0.01	7.09	8.01 0.01	7.09	6.66 0.04	Null	Null Null
58	39	NGC 0891	35.63731	42.34778	Sb	0.25 22.9	7.09	5.51 0.01	7.09	5.30 0.01	7.09	1.97 0.01	7.09	0.23 0.01
59	50	M85	186.35025	18.19108	S0-a	0.78 18.4	7.09	5.79 0.01	5.76	5.86 0.01	1.73	5.67 0.01	1.73	4.57 0.04
60	340	NGC 4244	184.37286	37.80739	Sc	0.19 46.5	7.08	7.51 0.01	7.08	7.46 0.01	7.08	5.34 0.01	7.08	3.27 0.01
61	221	NGC 4762	193.23326	11.23105	S0	0.29 27.8	7.08	7.11 0.01	5.16	7.19 0.01	1.61	6.96 0.02	1.61	6.18 0.10
62	155	NGC 5084	200.07019	−21.82725	S0	0.40 75.8	6.85	6.83 0.01	6.85	6.84 0.01	6.85	5.53 0.02	6.85	4.16 0.08
63	96	NGC 5907	228.97304	56.32876	SABc	0.19 154.3	6.76	6.47 0.01	6.76	6.35 0.01	6.76	3.24 0.01	6.76	1.57 0.01
64	461	NGC 4395	186.45364	33.54688	Sm	0.81 144.2	6.72	7.78 0.01	6.72	7.81 0.01	6.72	5.45 0.02	6.72	3.01 0.05
65	71	NGC 1407	55.04918	−18.58000	E	1.00 178.7	6.63	6.20 0.01	5.25	6.32 0.01	1.28	6.22 0.01	1.28	5.44 0.07
66	40	NGC 3627	170.06262	12.99155	Sb	0.53 177.3	6.59	5.56 0.01	5.16	5.47 0.01	5.16	2.03 0.01	5.16	0.02 0.01
67	148	NGC 4438	186.94028	13.00887	Sa	0.44 29.6	6.53	6.79 0.01	5.50	6.81 0.01	1.87	5.32 0.01	1.87	3.82 0.02
68	61	NGC 1365	53.40142	−36.14048	Sb	0.60 41.0	6.52	6.03 0.01	6.52	5.74 0.01	6.52	2.11 0.01	6.52	−0.46 0.01
69	42	NGC 2903	143.04214	21.50136	Sbc	0.49 21.5	6.48	5.67 0.01	6.48	5.58 0.01	6.48	2.07 0.01	6.48	0.09 0.01
70	87	NGC 5846	226.62210	1.60555	E	0.89 51.8	6.46	6.41 0.01	4.64	6.56 0.01	1.17	6.59 0.01	1.17	5.77 0.06
71	66	NGC 4725	192.61075	25.50079	SABa	0.63 40.0	6.44	6.09 0.01	5.12	6.15 0.01	5.12	3.99 0.01	5.12	2.62 0.02
72	83	NGC 1549	63.93811	−55.59235	E	0.80 5.3	6.43	6.35 0.01	5.68	6.46 0.01	1.90	6.09 0.01	1.90	5.21 0.03
73	1782	WLM	0.49227	−15.46099	IB	0.33 2.9	6.43	8.93 0.01	6.43	9.00 0.01	6.43	8.36 0.20	6.43	5.47 0.26
74	53	NGC 2841	140.51106	50.97655	SBb	0.47 151.4	6.41	5.89 0.01	4.93	5.91 0.01	4.93	3.78 0.01	4.93	2.21 0.01
75	14	Circinus Galaxy	213.29146	−65.33923	Sb	0.67 20.9	6.37	4.43 0.01	6.37	3.76 0.01	9.19	−0.29 0.04	8.70	−2.58 0.04
76	82	NGC 3621	169.56879	−32.81405	SBcd	0.48 162.0	6.33	6.33 0.02	5.23	6.21 0.02	5.23	2.57 0.01	5.23	0.85 0.01
77	134	NGC 5078	199.95856	−27.41013	Sa	0.39 145.7	6.32	6.71 0.01	4.60	6.68 0.01	2.73	4.07 0.01	2.73	2.46 0.01
78	62	NGC 1023	40.10017	39.06337	E-S0	0.47 84.0	6.30	6.04 0.01	4.52	6.12 0.01	1.60	5.94 0.01	1.60	5.01 0.05
79	44	NGC 7331	339.26675	34.41580	Sbc	0.43 172.0	6.22	5.70 0.01	6.22	5.61 0.01	6.22	2.36 0.01	6.22	0.67 0.01
80	26	M64	194.18185	21.68300	SABa	0.54 114.7	6.16	5.18 0.01	5.01	5.18 0.01	5.01	2.96 0.01	5.01	1.19 0.01
81	92	M59	190.50938	11.64700	E	0.76 164.9	6.11	6.45 0.01	4.50	6.57 0.01	1.44	6.20 0.01	1.44	5.23 0.06
82	123	NGC 4696	192.20518	−41.31093	E	0.62 97.9	6.07	6.66 0.01	5.06	6.74 0.01	1.62	6.63 0.01	1.62	5.54 0.06
83	11	M82	148.96646	69.67978	S?	0.79 54.1	6.06	4.07 0.01	6.06	3.61 0.01	8.01	−0.96 0.01	8.49	−4.14 0.01
84	538	ESO 274-001	228.55611	−46.80931	SAd	0.16 36.6	5.91	7.91 0.01	5.91	7.93 0.01	5.91	6.94 0.08	5.91	3.04 0.02
85	15	M77	40.66975	−0.01340	Sb	0.87 80.2	5.87	4.59 0.01	4.73	2.89 0.01	5.91	−0.68 0.04	6.32	−2.45 0.04
86	149	NGC 3077	150.82985	68.73387	S?	0.73 38.5	5.84	6.80 0.01	4.51	6.76 0.01	2.64	4.12 0.01	2.64	1.64 0.01
87	55	M65	169.73309	13.09245	Sa	0.34 171.3	5.84	5.90 0.01	4.91	5.92 0.01	4.91	4.16 0.01	4.91	2.78 0.02
88	98	NGC 7213	332.31741	−47.16676	Sa	0.97 174.6	5.83	6.48 0.01	3.99	6.47 0.01	2.21	4.36 0.01	2.21	2.48 0.01
89	49	IC 0356	61.94514	69.81254	Sb	0.72 103.0	5.80	5.76 0.01	4.98	5.78 0.01	4.98	3.78 0.01	4.98	1.95 0.02
90	1213	NGC 1560	68.20547	71.88394	Scd	0.22 24.4	5.79	8.59 0.01	4.51	8.75 0.01	1.56	7.71 0.04	1.56	5.55 0.04
91	74	NGC 2663	131.28387	−33.79462	E	0.65 112.2	5.78	6.26 0.01	5.03	6.36 0.01	1.22	6.45 0.01	1.22	4.95 0.03
92	85	NGC 4216	183.97667	13.14956	SABb	0.26 20.7	5.77	6.36 0.01	4.71	6.38 0.01	4.71	4.24 0.01	4.71	2.89 0.02

Table 1
(Continued)

iS (1)	iB (2)	Galaxy (3)	R.A. (deg) (4)	Decl. (deg) (5)	Morph. (6)	b/a PA (7)	R_{W1} (arcmin) (8)	$m1 \pm \Delta m1$ (mag) (9)	R_{W2} (arcmin) (10)	$m2 \pm \Delta m2$ (mag) (11)	R_{W3} (arcmin) (12)	$m3 \pm \Delta m3$ (mag) (13)	R_{W4} (arcmin) 14	$m4 \pm \Delta m4$ (mag) (15)
93	143	NGC 1055	40.43828	0.44376	SBb	0.30 103.8	5.69	6.76 0.01	5.69	6.64 0.01	5.69	3.08 0.01	5.69	1.32 0.01
94	303	NGC 5170	202.45326	−17.96646	Sc	0.17 127.3	5.67	7.43 0.01	4.74	7.41 0.01	4.74	5.24 0.01	4.74	3.79 0.02
95	135	M98	183.45123	14.90056	SABb	0.28 155.7	5.64	6.71 0.01	5.64	6.67 0.01	5.64	3.83 0.01	5.64	2.21 0.02
96	68	NGC 2997	146.41144	−31.19094	SABc	0.78 99.2	5.62	6.15 0.01	5.62	6.03 0.01	5.62	2.35 0.01	5.62	0.54 0.01
97	101	NGC 4125	182.02449	65.17439	E	0.71 83.9	5.61	6.50 0.01	4.03	6.59 0.01	1.44	6.27 0.01	1.44	5.20 0.04
98	102	NGC 7793	359.45728	−32.59102	Scd	0.62 97.9	5.60	6.52 0.01	5.60	6.43 0.01	5.60	3.21 0.01	5.60	1.55 0.01
99	108	NGC 5363	209.03012	5.25490	S0-a	0.68 124.6	5.60	6.57 0.01	4.06	6.63 0.01	1.49	5.69 0.01	1.49	4.36 0.02
100	245	NGC 4217	183.96248	47.09152	ZZZ	0.17 49.3	5.59	7.23 0.01	4.20	7.09 0.01	4.20	3.74 0.01	4.20	2.07 0.01
⋯	1081	IC 1613	16.20089	2.11914	IBm	0.90 135.4	4.69	8.49 0.01	4.69	8.69 0.01	Null	Null Null	Null	Null Null
⋯	22	M32	10.67439	40.86511	E	0.86 165.8	3.62	5.02 0.01	2.95	5.07 0.01	2.95	4.42 0.01	2.95	3.61 0.04
⋯	3902	UGC 05373	149.99974	5.33153	IB	0.75 97.0	2.89	9.76 0.01	1.76	10.04 0.02	Null	Null Null	1.76	6.69 0.35
⋯	8996	ESO 245-007	27.77698	−44.44341	Sm	0.81 11.2	2.18	11.06 0.01	2.18	11.28 0.04	Null	Null Null	Null	Null Null

Note. Columns: (1) order of *W1* 3.4 μm angular size; (2) order of *W1* brightness; (3) galaxy name; (4) and (5) J2000 coordinates; (6) RC3 Hubble type; (7) axis ratio and position angle (degrees east of north); (8) *W1* angular semimajor axis (arcmin), see Figure 5; (9) *W1* magnitude and associated error; (10) *W2* angular semimajor axis (arcmin); (11) *W2* magnitude and associated error; (12) *W3* angular semimajor axis (arcmin); (13) *W3* magnitude and associated error; (14) *W4* angular semimajor axis (arcmin); (15) *W4* magnitude and associated error. The following galaxies had saturated cores, necessitating recovery of lost flux: M82, NGC 253, Circinus, NGC 1068 (M77), and NGC 2070 (LMC).

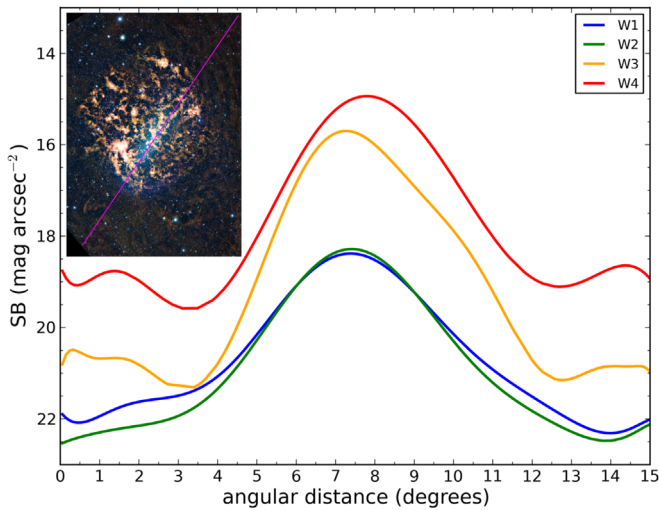(This table is available in machine-readable form.)

Figure 4. Mean surface brightness slice through the bar and central region of the LMC. The slice starts in the lower left of the LMC (see inset; magenta line) and extends 15° (~15.7 kpc) diagonally along the stellar bar. The mean surface brightness at a 100×100 pc scale is first computed, followed by fitting an 11th-order Legendre polynomial to produce the smooth (large-scale) result shown here. The stellar bar surface brightness (*W1*) peaks at (05:25:36, −69:49:34) J2000 coordinates.

4. Photometric Properties of the Largest Galaxies

In this section, we present the source characterization for the 100 largest galaxies, including isophotal and total flux measurements, colors, surface brightness, and bulge-to-disk comparisons.

4.1. Measurements of Integrated Flux and Radial Flux Distribution

Isophotal fluxes are derived from the *W1* (3.4 μm) $1 - \sigma_{sky}$ isophote (~23 mag arcsec^{-2}) fit with an elliptical aperture whose shape (axis ratio and position) was determined at a higher signal-to-noise ratio (S/N; $3 - \sigma_{sky}$) and, for simplicity, an assumed constant orientation throughout all radii. Total fluxes are estimated in two different ways: (1) asymptotic apertures and (2) by fitting the axisymmetric radial flux distribution; see below.

The angular size distribution ranges from $11'$ in diameter to the extreme ~10° size of the LMC. In fact, the size of the LMC is difficult to determine; it is not symmetric in shape, and it does not have an easily characterized radial distribution, as demonstrated in Figure 4. Here, slicing along the stellar bar, with a lower left end point (06:51:19, −71:32:57) to upper right end point (04:14:11, −65:19:19) perpendicular width of 100 pc ($5\rlap{.}'7$) and stretching 15° in total angular extent, the mean surface brightness is computed in 100×100 pc blocks along the profile. Fitting a high-order polynomial to the distribution produces a smoothed representation of the mean surface brightness (Figure 4). The stellar bar is evident in all four bands, peaking at a J2000 position (05:25:36, −69:49:34) and extending at least $\pm 5°$ to the nominal background level. As noted in the previous section, there is significant structure in the local background to the Magellanic Clouds, including the north–south "river" filament, which complicates the LMC characterization; consequently, the size and integrated flux measurements carry this additional uncertainty.

The mode of the size distribution, Figure 5, is about $13'$ in diameter. Other notably large galaxies include bright radio
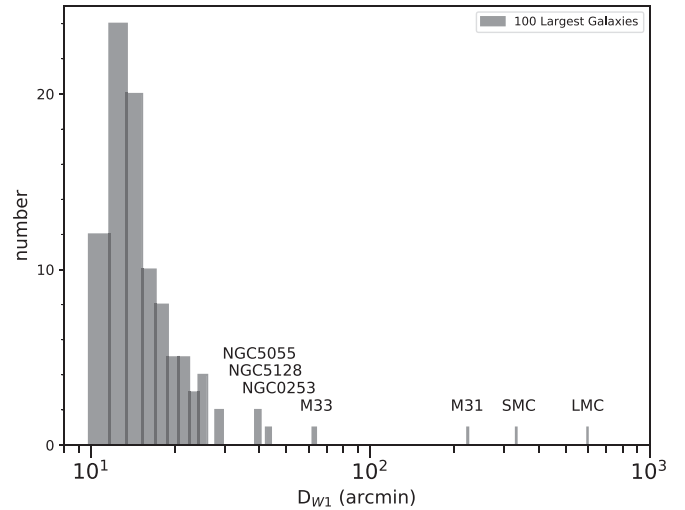

Figure 5. Angular diameter size distribution of the 100 largest galaxies based on the *WISE W1* imaging. The size metric is from the $1 - \sigma_{sky}$ (~23 mag arcsec^{-2}) isophotal semimajor axis (R_{W1}). The largest are the LG galaxies, followed by the nearest galaxy groups (NGC 253, Cen A), all within a few Mpc of the Milky Way.
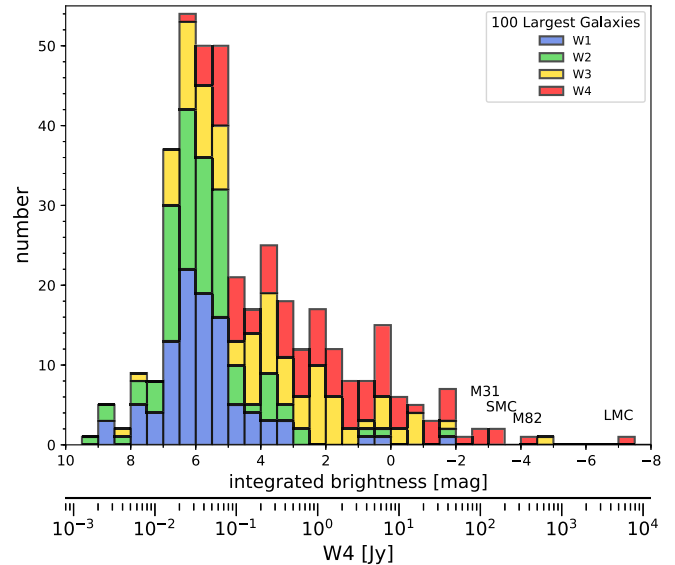

Figure 6. Stacked histogram showing the integrated brightness distribution for the four *WISE* bands based on the isophotal measurements. The brightest galaxies in *W4* (22 μm) are indicated, with the *W4* flux density scale (in Jy) given for comparison to the magnitudes. The LMC is the brightest owing to its proximity (50 kpc), but here the outstanding galaxy is M82, whose starburst is creating so much light in the infrared (~360 Jy) that it saturates in *WISE* (and *Spitzer*) imaging.

galaxy Cen A (NGC 5128), nearby nuclear starburst NGC 253, and the big four LG galaxies. The integrated flux ranges across ~7 mag for *W1* and *W2*, as well as an incredible 13–14 mag for *W3* and *W4* due to the extremes in SF activity traced in these mid-IR bands (notably, M82 makes a strong appearance); see Figure 6.

Total fluxes are estimated using both radial surface profile fitting and maximal curve-of-growth "asymptotic" apertures. The latter is simply a large aperture that represents the maximum flux achieved through a radial curve of growth within the error tolerance. This aperture is less than the background annulus radius, since it will converge before reaching the background level. It has some advantages,
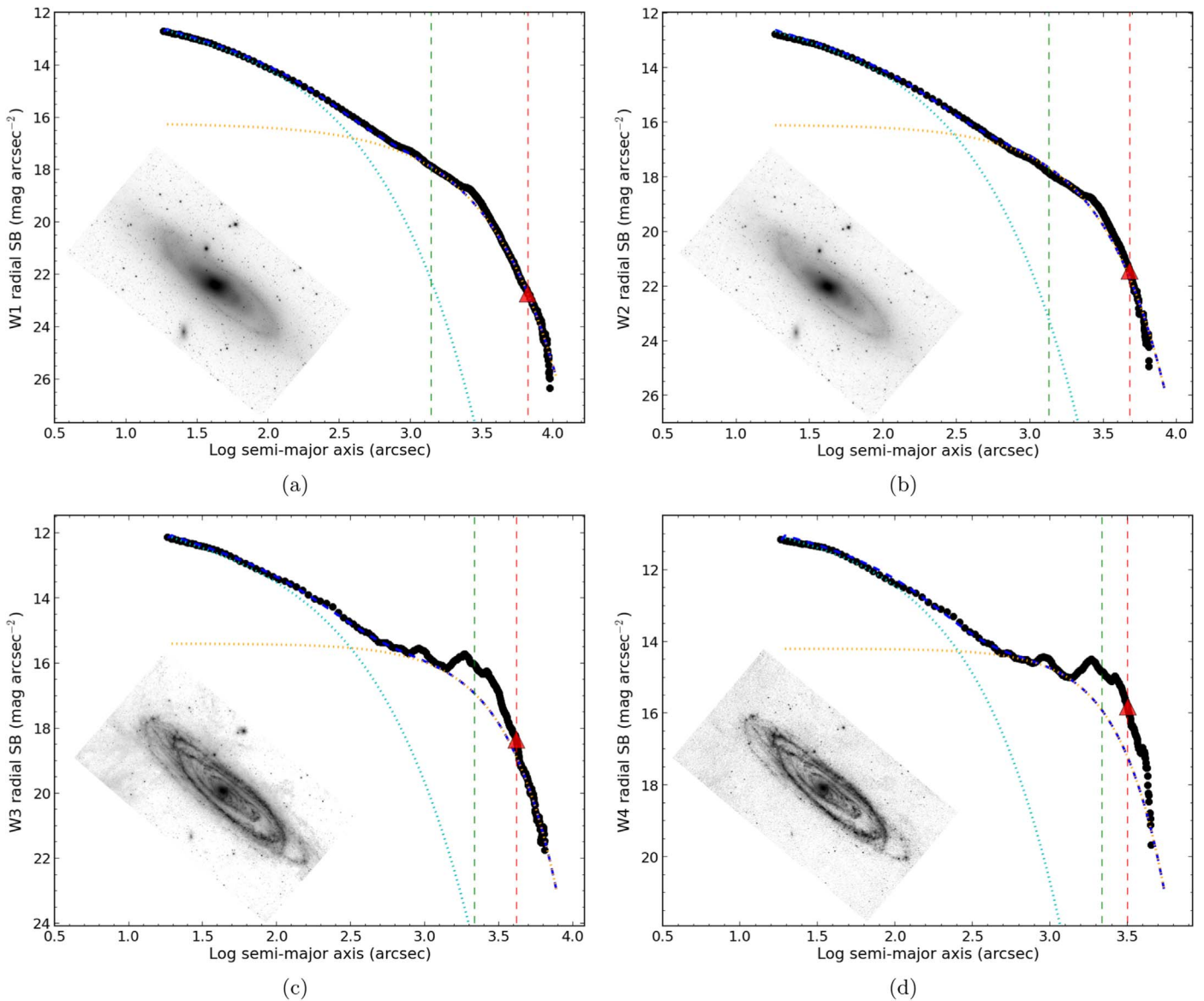
Figure 7. Axisymmetric radial profiles of M31 as measured for the four bands of *WISE*. The data measurements are indicated with black points, extending well beyond the $1 - \sigma_{\mathrm{sky}}$ isophotal radius (shown by the red triangle and dashed red line) into the single-pixel noise. The half-light radius is indicated by the green dashed line. The data are fit with a double Sérsic profile consisting of the inner bulge (blue dotted line) and disk (orange dotted line). The *W1* B/T is 0.67, indicating a prominent bulge. The inset figure shows the galaxy in the individual monochromatic band. Note that at longer wavelengths, the assumption of axisymmetry and smoothness is no longer valid due to the spiral arms and star formation regions.

including both simplicity and robustness for smaller angular-sized galaxies. On the other hand, it is susceptible to background gradients (e.g., nearby bright stars) and unsubtracted foreground stars; both of these effects can be systematic and are especially problematic for very large galaxies. Asymptotic magnitudes are a common method for estimating the total flux, having been used in many studies; e.g., Neill et al. (2014) used them for a large *WISE* sample Tully–Fisher relation study. The other method to estimate the total flux comes from a technique developed for 2MASS (Jarrett et al. 2000) by fitting a Sérsic profile to the axisymmetric radial profile. Since the mid-infrared includes both a bulge and disk (SF) component, we employ a double Sérsic to better fit the distribution. We demonstrate the performance of the fitting for M31 and M33 in Figures 7 and 8 showing log-log plots of the radial surface brightness. The measured surface brightness as a function of radius (in symmetric shells) is denoted by the filled

points, starting at a radius well beyond the PSF ($\sim15''$) and extending several degrees (in the case of M31) to well beyond the $1 - \sigma_{\mathrm{sky}}$ isophotal limit (denoted by the red triangle), to depths of around 26 mag arcsec^{-2} (or about 28.7 mag arcsec^{-2} in AB). The Sérsic fit is shown by the blue (bulge component) and orange (disk component) dotted curves.

Integrating out to three disk scale lengths beyond the $1 - \sigma_{\mathrm{sky}}$ isophotal limit, a radius of about 2°.8 for M31 and 0°.8 for M33, the total integrated flux (isophotal flux + extrapolation) for the four bands of *WISE* is 0.063, 0.104, −1.997, and −3.132 mag and 3.078, 3.020, −0.217, and −2.015 mag for M31 and M33, respectively. Comparing to the asymptotic aperture measurements, the M31 and M33 radii are 2°.49 and 1°.08, respectively, with fluxes of 0.078, 0.127, −1.950, and −3.111 mag and 3.032, 3.003, −0.174, and −1.945 mag, respectively. For these two LG galaxies, both total flux estimates appear to agree to better than 5%. Likewise,
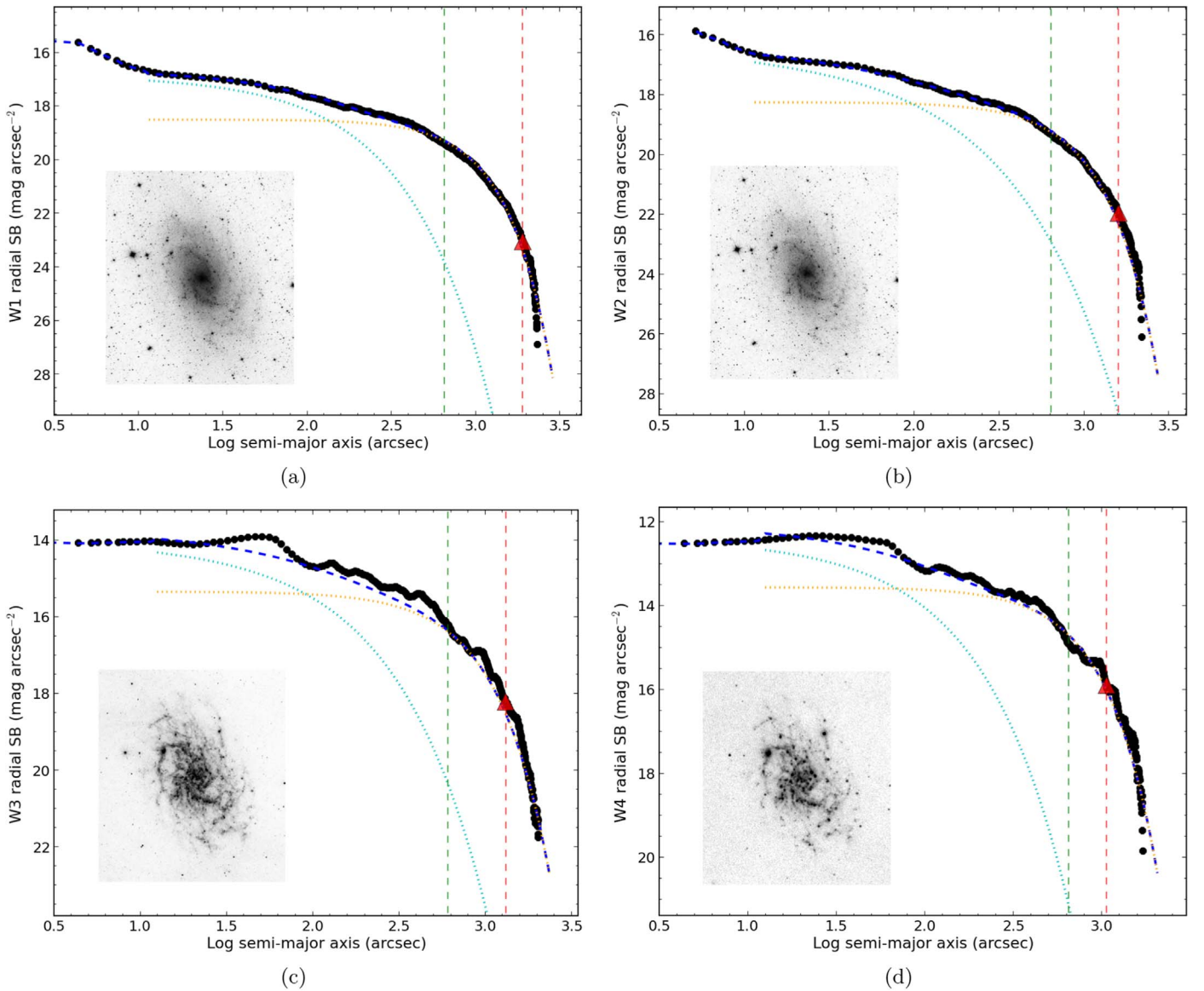
13

Figure 8. Axisymmetric radial profiles of M33 as measured for the four bands of *WISE*. See Figure 7 for details. The *W1* B/T is 0.3, indicating a prominent disk compared to the bulge population (compare with the bulgy galaxy, M31).

comparing the total fluxes from the two methods for the 100 largest galaxies, we find that there is very good correspondence, ∼1%, for the sensitive *WISE* bands (*W1* and *W2*) and 5%–6% for the *W3* and *W4* bands; see the tabulated statistical results in Table 2. Interestingly, there is a systematic in the median distribution, with profile fitting giving slightly (1%) brighter results in comparison to asymptotic apertures, likely because the fitting goes beyond the image noise to capture more flux. The exception is with *W3*, where the average (not the median) is skewed toward brighter fluxes. Visual inspection of galaxies with large discrepancies between the two methods reveals that early-type galaxies with very little *W3* emission (because only R-J stellar emission is seen for these types) have poor radial fits that do not extend much beyond the R_{W1} radius. It would appear that the asymptotic fluxes are more robust under these conditions, notably when the S/N is poor for radial fitting much beyond the $1 - \sigma_{sky}$ limit. We list the total photometry results for the largest 100 galaxies, including the radial profile fitting and the asymptotic, in Table 6 in

Table 2
Comparison between Total and Asymptotic Magnitudes

	(Total – Asymptotic) Magnitudes		
WISE Band ···	Ave. (mag)	Median (mag)	St. Dev. (mag)
W1	−0.01	−0.01	0.01
W2	−0.01	−0.01	0.01
W3	+0.05	−0.01	0.15
W4	−0.06	−0.06	0.05

Note. The sample consists of the 100 largest galaxies (with the exception of the Magellanic Clouds, which are not relevant here); the values correspond to the total minus the asymptotic magnitudes, where the total is estimated using a double Sérsic fitting to the radial surface brightness profile.

Appendix A. We will investigate the total flux differences in more detail and statistical clarity in Paper II when we include a much larger sample.
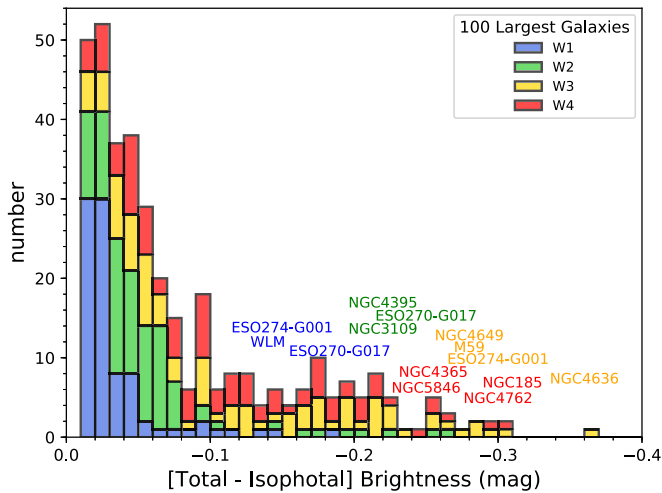
Figure 9. Comparison of the total vs. isophotal brightness for all four *WISE* bands. It is notable that *W1* isophotal and total fluxes are within 5% of each other, indicating the depth of the $1 - \sigma$ photometry. Outliers are indicated: low surface brightness galaxies tend to have large deviations for *W1* and *W2*, early types (spheroids) for *W3* and *W4*.

Figure 10. *WISE* colors of the 100 largest galaxies. The diagram attempts to delineate galaxies into four major groups: spheroid-dominated, intermediate disk, star formation–dominated, and AGN-dominated populations. The polygon dashed box is the AGN/QSO region defined in Jarrett et al. (2011). For comparison, the color distribution for ∼5000 WXSC (nearby, bright) galaxies is shown with the gray contours, and a set of WXSC galaxies are at higher redshift ($z > 0.3$), which accentuates the AGN and luminous (starbursting) types. We have defined a "star formation sequence" (cyan dashed line) in which normal galaxies—from quiescent to active SF—follow a track in this infrared color–color space. The yellow symbol to the left represents the mean colors and range of the brightest GCs, presented in Section 7.

Next, comparing the total fluxes from the radial fitting method to the $1 - \sigma_{\rm sky}$ isophotal fluxes, these total values are only 1.5%, 2.3%, 4.4%, and 4.1% brighter for bands *W1, W2, W3*, and *W4* for M31 and 1.5%, 0.5%, 5.2%, and 7.6% for M33. There is relatively little flux beyond the *W1* and *W2* isophotes, as demonstrated in Figure 9, which shows the difference (in magnitudes) between the total and isophotal magnitudes for the largest galaxies. For the most part, the total flux is within 4% of the isophotal flux for *W1* and 6% for *W2*. The exceptions (>20%) tend to be very low surface brightness galaxies (e.g., WLM and ESO 270-G017), in which there may be a significant component just below the $1 - \sigma_{\rm sky}$ noise per pixel.

For the long wavelengths, *W3* and *W4*, we observe a different behavior. The isophotal-to-total correction has a larger spread, easily ranging out to 25% or more, with the largest deviations occurring for early-type galaxies (e.g., Maffei 1, NGC 4406, NGC 4762) in which there is little emission in the *W3* and *W4* bands, only stellar (R-J) emission; hence, these bands miss a large fraction of the stellar and ISM light. Consequently, total flux measurements (either asymptotic or profile-fitting) are important for these bands when, e.g., measuring the global SFR; see next section.

4.2. Color Classification of the Largest Galaxies

Similar to optical color analysis of galaxies (e.g., the red and blue sequence, the green valley), mid-IR color diagnostics have proven to be useful in classifying the activity of galaxies, at least crudely separating quiescent, SF, and AGN populations (Lacy et al. 2004; Jarrett et al. 2011; Stern et al. 2012; Yan et al. 2013; Cluver et al. 2014, 2017), as well as radio galaxy types (Ching et al. 2017; Jarrett et al. 2017). Here we consider the galaxy colors after correcting for spectral redshift using a diverse set of templates compiled by Brown et al. (2014b) fit to the 2MASS XSC (Jarrett et al. 2003) plus *WISE* photometric spectral energy distribution (SED) measurements from this work; the templates and fitting method are detailed in Jarrett et al. (2017), and some example SED templates with photometric fits are given in Appendix B.
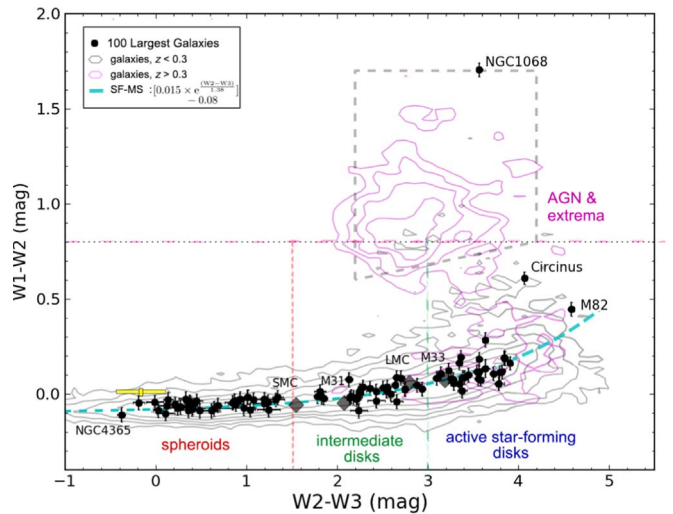
The color–color location for the largest 100 galaxies is presented in Figure 10. For comparison and context, we show the *WISE* rest-frame-corrected colors for the ∼5000 brightest galaxies in the WXSC, to be presented in detail in Paper II. The largest galaxies, with their corresponding high-S/N measurements, define a tight track within the color–color distribution of bright (low-redshift) WXSC galaxies (gray contours). The track ranges from mid-IR "blue" stellar-dominated galaxies to mid-IR "red," or dusty, SF galaxies, with approximately 4 mag of delineation in the *W2–W3* color. Along the *W1–W2* (*Y*-) axis, the trend is for the color to "warm" as the SF, or, alternatively, the AGN, activity increases. In the case of the largest galaxies, this spans approximately 0.4 mag.

We use the rest-frame-corrected measurements from the largest and highest-S/N galaxies to fit the functional form of this *WISE* color–color "sequence," given by

$$(W1 - W2) = [0.015 \times e^{\frac{(W2 - W3)}{1.38}}] - 0.08. \qquad (1)$$

The track is roughly flat with *W2–W3* color, curving upward (in *W1–W2* color) for the dusty SF galaxies. This curvature can be understood as warm dust from active star formation elevating the *W2* (4.6 μm) band relative to the bluer *W1* (3.4 μm) band. For example, the starburst galaxy M82 with a steeply rising mid-IR continuum exhibits a warmer *W1–W2* color—by 0.5 mag—compared to the early-type spiral galaxy M31. More extreme galaxies, including LIRGs and AGNs, lie well above this SF track, separating normal galaxies from active systems.

Considering just the 100 largest galaxies, there are several notable outliers: starburst M82 has the reddest *W2–W3* color of the sample, indicative of its active SF, while the two AGNs of the sample, Circinus and NGC 1068, have very warm *W1–W2* colors, a signature of AGN torus dust heating. In fact,

NGC 1068 is so warm, $W1–W2 \sim 1.7$ mag, it falls near the extreme limit of the AGN/QSO zone defined in Wright et al. (2010) and Jarrett et al. (2011). Classified as a Seyfert 2 LIRG, NGC 1068 (M77) is not only exceptional given its close proximity to the Milky Way ($\sim$10 Mpc), but it is also clearly an outlier compared to other galaxies in the local universe, as shown by the gray contours ($z < 0.3$), and the higher-redshift galaxies ($>$0.3) with luminous AGNs appearing in significant numbers (magenta contours).

Following the prescription of Jarrett et al. (2017), we have divided the color–color plane into four zones that are inspired by infrared morphology considerations of bulge, disk, and nuclear stellar populations (Johnson et al. 2007; Walker et al. 2010; Jarrett et al. 2011, 2013, 2017).

The early-type spheroids (E/S0) have "blue" colors, $W2–W3 < 1.5$ mag. They are characterized by prominent bulges with stellar-dominated mid-IR emission arising from evolved (luminous) stars (see also next section, bulge-to-disk measurements). They are some of the most massive and brightest galaxies in the mid-IR (see below) and tend to be located in dense environments: the brightest cluster galaxies, such as Fornax A (NGC 1316), Virgo A (M87), and many of the bright Virgo cluster galaxies, live in this zone. Since they tend to have little SF activity (unless undergoing a gas-rich "wet" merger or accretion event, consider the infrared excess in the core of Fornax A; Asabere et al. 2016), they are often difficult to detect in $W3$ and $W4$ because of the rapidly diminishing R-J tail; hence, only nearby examples can be detected in all three $WISE$ $W1, W2,$ and $W3$ bands, rendering a distance selection bias when studying these objects with $WISE$ colors, also noted in Jarrett et al. (2017).

In contrast, active SF galaxies, $W2–W3 > 3$ mag, have bright $W3$ emission and are easily detected in all four bands. Here we find the late-type disks that have ongoing SF (e.g., M83) and starbursting galaxies (M82, NGC 253, NGC 1365). Intermediate between the gas-depleted and SF galaxies, 1.5 mag $< W2–W3 < 3.0$ mag, are the early-type spirals (e.g., M81, M31, Milky Way) characterized by prominent bulges, semi-quiescent SF disks, and pseudo-bulges. Some of these galaxies may be undergoing quenching due to environmental effects and likened to green valley populations seen in the optical and infrared (e.g., Johnson et al. 2007; Walker et al. 2010; Cluver et al. 2013).

The final demarcation is for the extrema populations, QSOs, and various flavors of mid-infrared AGN activity, including high-excitation, broad-line radio galaxies (HERGs and AeBs). Those whose hosts are completely dominated by AGN emission tend to have $W1–W2$ colors greater than 0.8 (Stern et al. 2012), while some Seyferts may lie below this line (e.g., Circinus) chiefly due to strong host SF emission, comparable to the AGN itself (For et al. 2016). In order to track Circinus as an AGN (Seyfert 2), we relax the $W1–W2$ threshold to a value of 0.5 mag so we can include Circinus in the AGN group (along with NGC 1068). Current studies of AGNs and X-ray/infrared colors (Mingo et al. 2016; Huang et al. 2017) seem to indicate that Seyferts and low-power AGNs can have $W1–W2$ colors much below the 0.8 demarcation (e.g., 0.3–0.8) but still well above the SF track (Equation (1)).

Colors broadly reveal spectral features and continuum trends. The actual mid-IR spectra for galaxies are far richer, encoding the early-to-late star formation histories. Examples of the broad $WISE$ color classification are shown in Appendix B, where the SEDs reveal the rich emission features for each color class.

4.3. Surface Brightness

Employing the color classification, we investigate the half-light surface brightness, SB_{eff}, of the sample. The half-light, or effective, radius is derived from the total flux measurement and corresponds to the radius at which half of the total light is enclosed within the ellipsoidal shape of the galaxy. This radius can be compromised by the relatively large $WISE$ PSF for small galaxies, but in the case of the largest galaxies in the sky, the radius is well determined. The effective surface brightness is the half-light flux normalized by the encompassed area. This distant-independent value is sensitive to the Hubble type, with bright surface brightnesses attributed to early-type bulge-dominated systems, and, conversely, late-type spirals have relatively faint surface brightnesses.

The resulting half-light surface brightness for the 100 largest galaxies is presented in Figure 11, which includes panels for each photometric band. In the stellar bands, $W1$ and $W2$, there are a number of sources with brightnesses between 16 and 17 mag arcsec^{-2} for all classification types, with more subtle delineations following the expected trends: spheroids are typically brighter than SF disks, and although there is a distinct population of spheroids that have low values, these are the dwarf spheroidals (see below). Intermediate disk galaxies have the largest spread in surface brightness, 15–20 mag arcsec^{-2}, and finally, the brightest galaxies by several orders of magnitude are the AGNs and nuclear starburst galaxies. The faintest galaxies are the low surface brightness dwarfs (hence their moniker), including the ghostly ESO 245-007.

More diversity is evident in the dust emission–sensitive bands of $W3$ and $W4$ (Figures 11(c) and (d)). Spheroidals are now the faintest galaxies and, as noted previously, can be difficult to detect in the long-wavelength channels of $WISE$. Not surprisingly, the brightest galaxies are the active SF galaxies (e.g., M82, NGC 0253, NGC 1365) and the AGN "extrema" (NGC 1068 and Circinus). Intermediate disks again have a broad range in values, indicating both semi-quiescent (low SB_{eff}) and high-SF (high SB_{eff}) populations, but they truly fill the gap between "dead" and SF galaxies, notably in the warm dust continuum band of $W4$ (Figure 11(d)).

It is instructive to compare the $WISE$ half-light measurements with those from the 2MASS Large Galaxy Atlas (LGA) from Jarrett et al. (2003). It has already been noted that $WISE$ isophotal radii are two to five times larger than those from the LGA and hence capturing more of the total light, notably for low surface brightness (dwarf) galaxies and early types with $R^{1/4}$ profiles. For these cases, we would expect the half-light radii to be correspondingly larger and surface brightnesses to be fainter. Figure 12 presents the comparison of (effective) half-light radii and surface brightness between the $WISE$ and 2MASS measurements. The top panel shows the results for the half-light radii; the dashed line shows the expected 1:1 correspondence if all things were equal. The bottom two panels show the effective surface brightness comparison, with the dashed line representing equal half-light surface brightness. What we see is that $WISE$ 3.4 μm half-light radii are nearly all much larger than those from the 2.2 μm imaging, and in some extreme cases, they reach nearly four times larger, corresponding to the lowest surface brightness galaxies (note bottom panels), thus demonstrating the relatively poor sensitivity of the 2MASS LGA to dwarf galaxies (e.g., WLM and ESO 270-G017). Similarly, for the large and extended early-type galaxies, such as NGC 4406, $WISE$ detects far more total
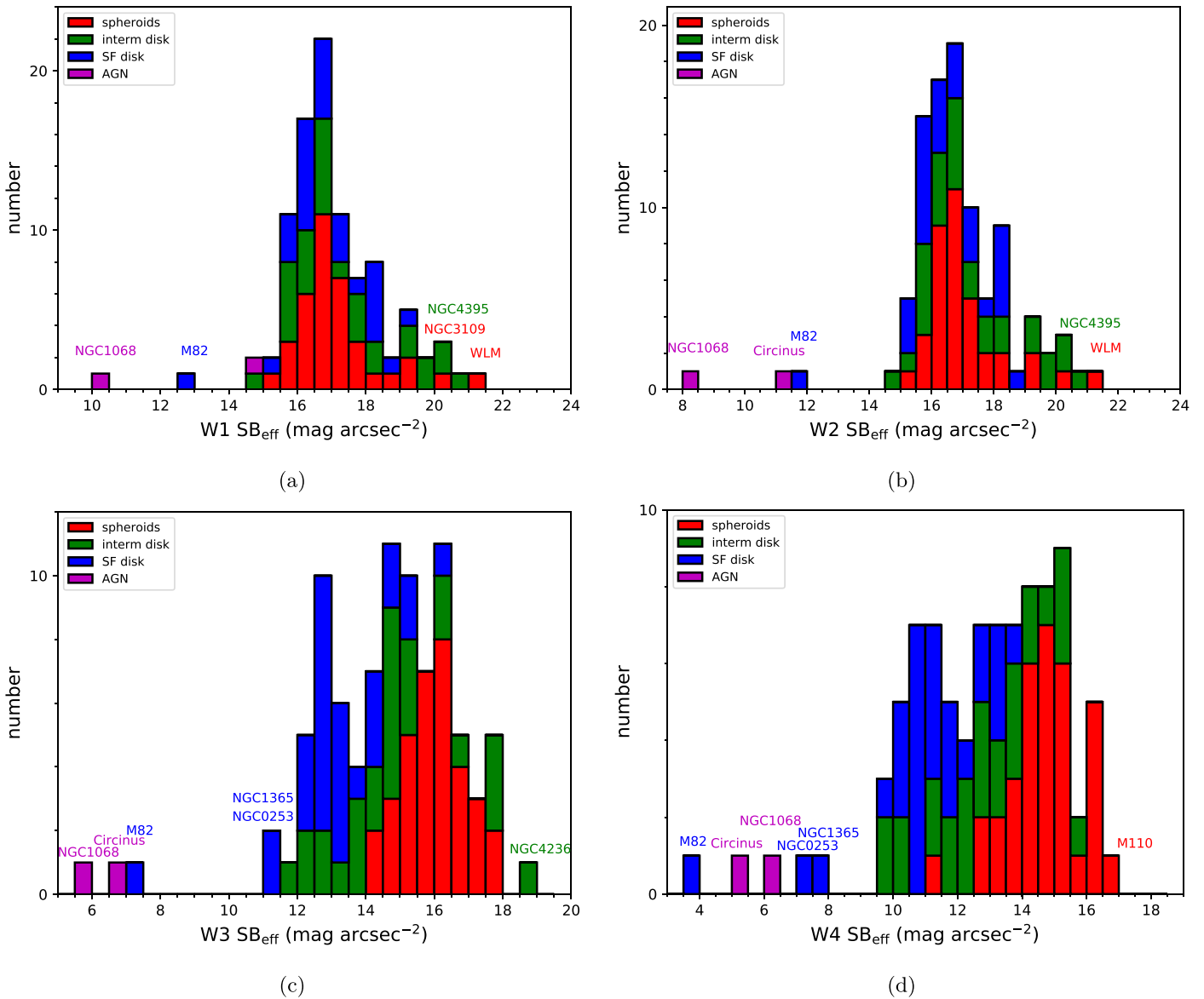
Figure 11. Half-light surface brightness (SB$_{eff}$) for the 100 largest galaxies based on the four bands of *WISE*. The galaxies are group-delineated by their *WISE* colors (see Figure 10), with notably bright and faint galaxies labeled and four-band standouts NGC 1068, Circinus, and M82.

emission, giving rise to larger half-light radii and fainter surface brightnesses. Interestingly, for the nuclear active galaxies—starburst M82, AGN Circinus, and NGC 1068— the *WISE* half-light radii are smaller (more compact) and significantly higher surface brightness (1–3 mag; see bottom panels of Figure 12) compared to 2MASS, likely due to less extinction in the longer *WISE* bands and the SED differences between the 2.2 and 3.4 μm bands.

4.4. Bulge and Disk Populations

On scales of kiloparsecs, well-resolved galaxies exhibit aggregate stellar populations that are typically decomposed into disk and bulge populations that are distinct not only in their spatial distribution but also mean age, mass, and luminosity characteristics. The near- and mid-infrared are sensitive to cooler populations of dwarf and giant stars, which dominate the total stellar mass of the host galaxy. For the *WISE* colors, we have subdivided the *W2–W3* color to represent bulk

populations from spheroidal (early-type, typically the oldest populations), intermediate disks and young spiral galaxies, which should, in principle, be reflected in the light coming from the separate bulge and disk populations (see previous section on the infrared color–color diagram).

Here we employ a very simple decomposition based on axisymmetry and a double Sérsic fit to the *W1* (3.4 μm) radial profile. The inner profile represents the bulge population, constrained by a (relatively high) Sérsic index that may range between 2 and 4, and a smaller scale length relative to the disk. The disk component has an index between 0.8 and 2 (the ideal being a perfect exponential index of 1). An example of a radial decomposition can be seen in Figure 7, showing the bulge and disk populations of M31, which has a bulge-to-total ratio (B/T) of 0.67.

Figure 13(a) presents the B/Ts for the 100 largest galaxies, coded by their *W2–W3* global colors and normalized to show relative differences. The strongest trend is for the early types, which have a strong peak at high (∼0.9) B/T, consistent with
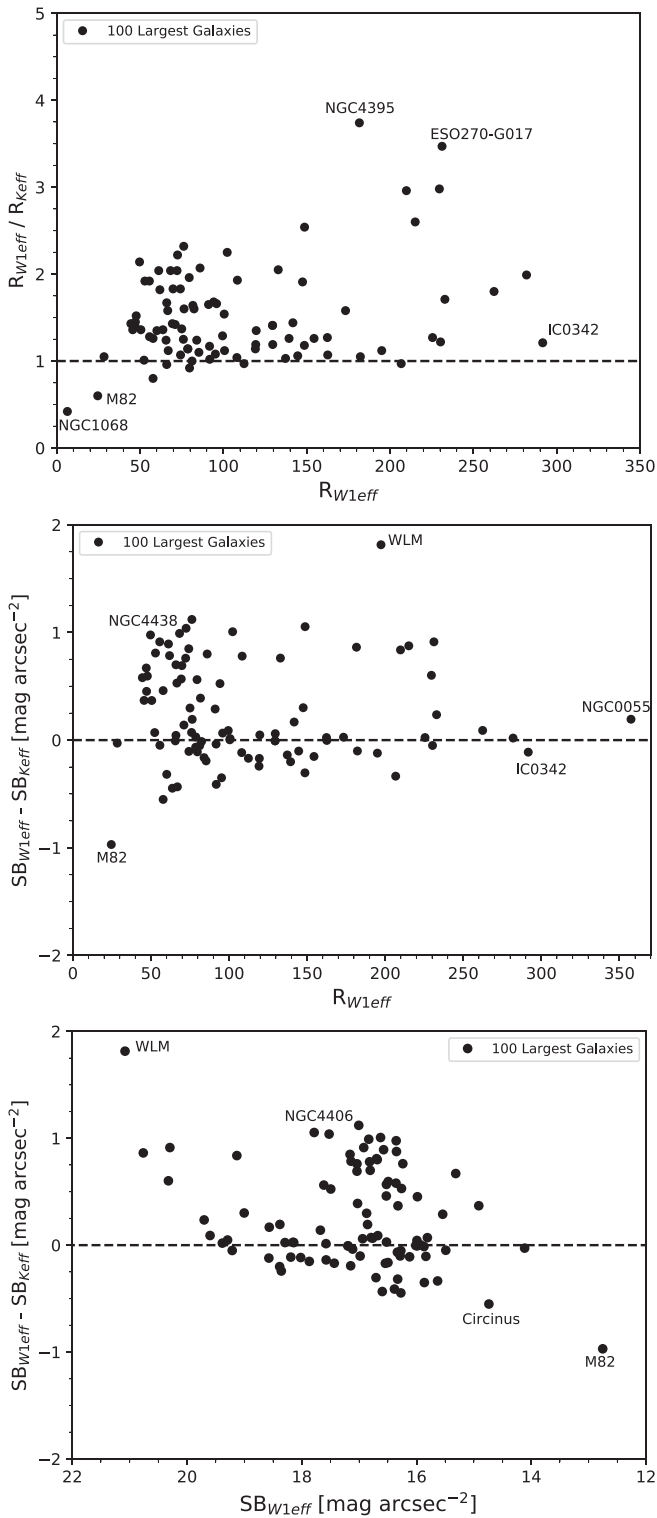
Figure 12. Half-light radius (top panel) and surface brightness (bottom two panels) comparison between *WISE W1* and the 2MASS K_s band. Here *W1* [3.4 μm] is much more sensitive than the 2MASS K_s [2.17 μm] band; hence, it has much larger radii (and fainter surface brightnesses) for dwarf (low surface brightness) and early-type galaxies.

the late-type spirals (*W2–W3* > 3 mag) range across the B/T scale, similar to the intermediate disks; only a slight trend toward lower B/T is seen for the more SF-active galaxies. At face value, the B/T clearly delineates the early-type spheroids but seems to have less power in decomposing the stellar populations in the more active (and presumably disky) galaxies, perhaps confusing the (low scale height) pure disk, (larger scale height) thick disk, and pseudo-bulge populations that would comprise the SF color galaxy set.

We compare the B/T of the 100 largest galaxies with that of the nearby galaxy WXSC, notably the 5000 brightest galaxies (all at low redshifts, $z < 0.1$), in Figure 13(b), again normalized to show relative differences across the range. The only difference between these two samples is that the 100 largest are the most well resolved, while the 5000 brightest may not always clearly resolve the different stellar populations. We would expect little difference between the two sets; however, we see that the nearby galaxy sample does not have a prominent peak at B/T = 0.9, while it does have a relative excess at low-B/T, disky galaxies with 0.05–0.2 in ratio. Either the larger nearby sample has a statistically significant set of disky galaxies (relative to the 100 largest), the 100 largest sample is dominated by bulgy galaxies, or there is some biased difference, perhaps related to angular resolution. The 100 largest are biased in the sense that we have chosen those with the largest angular extents, which could very well be the spheroidal galaxies whose $R^{\frac{1}{4}}$ light distribution is detectable at larger angular scales compared to disks with exponential light falloff. We will investigate the B/T properties of the nearby galaxies in Paper II, creating subsamples that do not have such angular biases.

5. Derived Physical Properties: Size, Mass, and SFR

The physical parameters presented in this section are derived from the isophotal measurements presented above, combined with the adopted distance to the object. If available, we use redshift-independent distances (Cepheid, tip of the red giant branch, Tully–Fisher, etc.) as tabulated in NED,[10] adopting the median value as a robust estimate that minimizes the impact of completely unphysical values, compared to the distribution, occasionally found in lists curated by NED. For those without redshift-independent distances, we instead compute the redshift luminosity distance in the CMB frame after correcting for LG motion. In the case of physical diameters and beam sizes, we instead use the angular diameter distance. For luminosities, we compute two different kinds: spectral νL_ν and in-band L_λ, where the former is used for SFRs and the latter for stellar mass, as is the tradition. It should be emphasized that these two luminosities are distinctly different: the spectral luminosity is monochromatic and normalized by the bolometric luminosity of the Sun, while the in-band is normalized by the integrated solar spectrum convolved with the *WISE W1* band (as computed in Jarrett et al. 2013). Key derived parameters are listed in Table 3.

5.1. Physical Size Distribution

We compute the diameters using the *W1* (3.4 μm) $1 - \sigma_{sky}$ isophotal radii and the redshift-independent or angular diameter distance (as discussed above). The distribution of the 100

their dominant (global) spheroidal population. The two AGNs in the sample also have a high ratio due to the unresolved nucleus emitting at mid-infrared wavelengths from hot dust accretion, thoroughly dominating the total light (see Figure 11 showing the effective surface brightness). Much less defined,

---

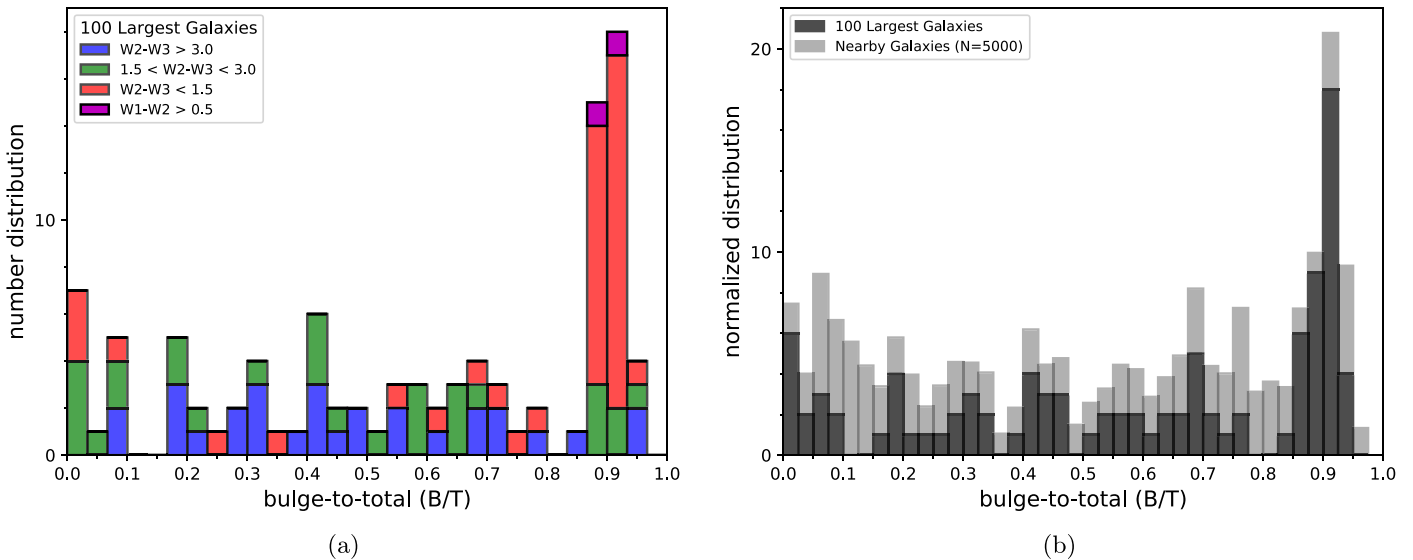[10] http://ned.ipac.caltech.edu/Library/Distances/

Figure 13. (a) The B/T light decomposition for the 100 largest galaxies in comparison to a large sample of nearby galaxies in the WXSC. The bulge and disk properties are derived from the axisymmetric radial profile fit with a double Sérsic function. Disk and spheroidal properties are correlated with *W2–W3* color: blue galaxies tend to have high B/Ts, while red (SF) galaxies have considerably lower ratios. It should be noted that the largest galaxies have a strong peak at B/T $\sim$ 0.9, which is not as apparent in a large sample of nearby galaxies (see panel (b)).

largest (angular) galaxies is presented in Figure 14, ranging from a few to well over 100 kpc. Here we have once again divided the sample by the color classification (Figure 10) to discern any trends with the morphology proxy.

To begin with, there is a stark separation between the two flavors of early-type systems (bulge-dominated spheroids): giant cluster (brightest or BCG) galaxies and dwarf spheroidals. Fornax A has the largest diameter, nearly 140 kpc in size, closely followed by the largest Virgo cluster galaxies, which are all double or triple the size of the large disk galaxies (e.g., the Milky Way is $\sim$50 kpc in extent), and some local BCG galaxies (e.g., NGC 4696 and NGC 5078). Intermediate disk galaxies (e.g., NGC 5078) have the second-largest distribution. At the other end of the scale, the diminutive satellite dwarf spheroidals (e.g., NGC 0147) are the representative population, followed by dwarf intermediate-type galaxies (e.g., NGC 6822). Occupying the center stage, late-type disks uniformly range from small $\sim$10 kpc to broad 60 kpc diameters. Setting aside the extreme size ($\sim$100 kpc) of radio galaxy M87 (Virgo A), the two outstanding AGNs in the sample, NGC 1068 (M77) and Circinus, have host galaxy sizes that are not particularly large, $<$25 kpc, indicating relatively modest or compact bulges and SF regions. We will investigate this trend with the larger WXSC sample to see if Seyferts and AGNs in general are more compact relative to SF disk galaxies.

5.2. Spatial Resolution

WISE does not have outstanding angular resolution, roughly 6″ in the shortest bands. Nevertheless, the largest galaxies in the sky are also (typically) the nearest galaxies; hence, the physical spatial resolution is well suited for the study of the internal components of galaxies. Examining column 4 in Table 3, the physical beam size (at 3.4 μm) ranges from 1 to 2 pc in the Magellanic Clouds, to $<$300 pc for local volume galaxies (e.g., M51) and 500 pc for Virgo and Fornax cluster galaxies, to 1 kpc for the most distant galaxies in the 100 largest sample. The four independent bands of *WISE* at this

physical resolution make it a superlative imaging set to combine with complementary data sets (e.g., *GALEX*-UV, *Herschel*-PACS, radio continuum, neutral hydrogen) in order to study the internal star formation processes in giant molecular clouds and the general ISM; see, for example, the detailed study of M31 (Tomicic et al. 2019), M33 (Kam et al. 2017; Elson et al. 2019), NGC 253 (Lucero et al. 2015), and M83 (Jarrett et al. 2013; Heald et al. 2016). Both the standard and mask/cleaned *WISE* mosaics (see Appendices C and D) of the largest galaxies will be publicly available to the astronomical community through NED and other astronomical archives.

5.3. Global Stellar Mass

As one of the most important physical parameters for decoding the star formation history of a galaxy, estimating the aggregate stellar mass is one of the key priorities for near- and mid-infrared imaging extragalactic surveys because of their sensitivity to the evolved population R-J stellar bump between 1 and 4 μm; see Jarrett et al. (2013) for discussion of the *Spitzer*-IRAC and *WISE* bands used to trace the stellar mass. Accordingly, the galaxy host stellar mass is estimated using the *W1* integrated (isophotal) flux density converted to in-band luminosity, L_{W1}, and the *M/L* ratio based on the *W1–W2* color relation (Cluver et al. 2014). Here we assume that the *W1* (3.4 μm) light arises from the evolved population and that the short-lifetime dusty-phase populations (post-AGBs) are not significantly skewing the near-infrared brightness compared to the calibrated relation.[11]

We adopt the "nearby galaxy" *M/L* prescription from Cluver et al. (2014), where the *WISE W1* in-band luminosity was calibrated against Galaxies and Mass Assembly (GAMA) stellar masses derived using stellar population synthesis models

---

[11] The 3–5 μm bands appear to remarkably trace the stellar mass compared to other independent metrics (Cluver et al. 2014; Ponomareva et al. 2017; Kettlety et al. 2018), but see also Meidt et al. (2012) and Querejeta et al. (2015) for alternative views.

Table 3
Derived Global Stellar Mass and SFRs

iS	Galaxy	d (Mpc)	Beam (pc)	$1-2$ (mag)	$2-3$ (mag)	$\log L_{W1}$ ($L_{\odot,W1}$)	$\log M_\star$ ($M_\odot$)	$\log \nu L_3$ ($L_\odot$)	$\log \nu L_4$ ($L_\odot$)	SFR_{W3} ($M_\odot\,\mathrm{yr}^{-1}$)	SFR_{W4} ($M_\odot\,\mathrm{yr}^{-1}$)	$\log$ sSFR (yr^{-1})
(1)	(2)	(3)	(4)	(5)	(6)	(7)	(8)	(9)	(10)	(11)	(12)	(13)
(a)												
1	LMC	0.05	1	0.06	2.79	9.47 0.01	9.15 0.11	7.62 0.01	7.76 0.01	0.12 0.03	0.03 0.14	−10.07
2	SMC	0.06	2	−0.05	1.55	8.63 0.01	8.59 0.09	6.06 0.01	6.43 0.01	0.01 0.01	0.01 0.01	−10.59
3	M31	0.77	22	−0.03	2.09	11.04 0.02	10.95 0.14	8.82 0.02	8.48 0.03	1.20 0.11	0.58 0.07	−10.88
4	M33	0.86	25	0.07	3.18	9.97 0.02	9.61 0.14	8.33 0.02	8.22 0.03	0.45 0.04	0.33 0.04	−9.96
5	NGC 0253	3.01	88	0.19	3.83	10.88 0.01	10.24 0.09	9.54 0.01	9.64 0.01	5.36 1.86	6.52 2.56	−9.51
6	NGC 5128	3.65	106	0.01	2.55	11.23 0.01	11.02 0.09	9.25 0.02	9.12 0.01	2.98 1.03	2.16 0.85	−10.55
7	NGC 0055	2.10	61	0.09	2.66	9.77 0.01	9.39 0.09	7.88 0.02	8.06 0.01	0.19 0.06	0.23 0.09	−10.11
8	M81	3.65	106	−0.01	1.81	10.99 0.01	10.85 0.09	8.62 0.04	8.44 0.02	0.82 0.29	0.52 0.20	−10.94
9	M101	7.22	210	0.12	3.54	10.91 0.01	10.45 0.10	9.43 0.01	9.36 0.01	4.22 1.46	3.61 1.42	−9.82
10	NGC 4945	3.22	94	0.18	3.57	10.71 0.01	10.07 0.09	9.26 0.01	9.15 0.01	3.03 1.05	2.31 0.91	−9.59
11	IC 0342	3.14	91	0.05	3.80	10.74 0.01	10.43 0.09	9.33 0.02	9.23 0.01	3.49 1.21	2.75 1.08	−9.88
12	NGC 1316	18.92	550	−0.03	0.74	11.82 0.01	11.72 0.10	8.28 0.61	8.60 0.06	0.42 0.14	0.73 0.29	−12.09
13	M49	15.28	444	−0.09	0.47	11.66 0.01	11.62 0.10	<4.28	7.73 0.28	<0.01	0.12 0.05	<−12.17
14	M86	16.32	475	−0.05	−0.18	11.53 0.01	11.48 0.10	<4.33	<4.04	<0.01	<0.01	<−10.84
15	Maffei 1	3.39	99	−0.04	−0.03	10.85 0.01	10.79 0.10	<2.97	7.02 0.23	<0.01	0.03 0.01	<−11.43
16	M110	0.82	24	−0.05	0.89	9.00 0.01	8.96 0.09	5.75 0.31	5.85 0.06	0.01 0.00	0.00 0.00	−10.96
17	M104	9.38	273	−0.03	1.01	11.38 0.01	11.28 0.09	8.34 0.19	8.30 0.04	0.47 0.16	0.39 0.15	−11.61
18	NGC 2403	3.18	93	0.09	3.38	10.04 0.01	9.65 0.09	8.47 0.01	8.43 0.01	0.61 0.21	0.51 0.20	−9.86
19	NGC 0247	3.44	100	−0.04	2.67	9.79 0.01	9.72 0.09	7.84 0.03	7.73 0.04	0.17 0.06	0.12 0.05	−10.49
20	M106	7.31	213	0.03	2.51	10.93 0.01	10.68 0.09	8.94 0.02	8.80 0.02	1.60 0.55	1.12 0.44	−10.47
21	M87	15.80	460	−0.07	0.42	11.57 0.01	11.53 0.10	<4.30	8.08 0.11	<0.01	0.24 0.10	<−12.49
22	NGC 3628	10.45	304	0.12	3.24	11.02 0.01	10.53 0.09	9.40 0.01	9.33 0.01	4.05 1.40	3.40 1.33	−9.93
23	NGC 0300	1.93	56	−0.00	2.59	9.58 0.01	9.41 0.10	7.62 0.02	7.55 0.01	0.11 0.04	0.08 0.03	−10.37
24	NGC 4736	5.20	151	0.02	2.75	10.81 0.01	10.58 0.10	8.93 0.02	8.80 0.01	1.56 0.54	1.11 0.44	−10.39
25	NGC 6822	0.47	14	−0.02	2.45	8.34 0.01	8.22 0.09	6.30 0.04	6.39 0.05	0.01 0.00	0.01 0.00	−10.22
26	NGC 1532	14.25	415	0.05	2.86	11.02 0.01	10.73 0.09	9.20 0.02	9.02 0.02	2.69 0.93	1.76 0.69	−10.30
27	NGC 5236	4.51	131	0.12	3.82	10.90 0.01	10.43 0.10	9.53 0.01	9.56 0.01	5.17 1.79	5.42 2.12	−9.72
28	NGC 0147	0.73	21	−0.02	1.85	8.41 0.01	8.30 0.09	6.06 0.04	<1.34	<0.01	<0.01	<−9.69
29	NGC 6744	9.51	277	0.01	3.35	11.04 0.01	10.83 0.09	9.43 0.02	9.20 0.01	4.24 1.47	2.57 1.01	−10.20
30	M63	9.81	285	0.05	3.35	11.16 0.01	10.86 0.09	9.56 0.01	9.38 0.01	5.60 1.94	3.75 1.47	−10.11
31	NGC 1553	17.18	500	−0.06	0.69	11.39 0.01	11.34 0.10	7.47 1.42	8.04 0.08	0.08 0.03	0.22 0.09	−12.44
32	NGC 1399	19.61	570	−0.08	0.39	11.56 0.01	11.51 0.10	<4.49	7.47 0.41	<0.01	0.07 0.03	<−11.90
33	NGC 4236	4.47	130	−0.09	2.32	9.44 0.01	9.40 0.10	7.31 0.04	7.56 0.02	0.06 0.02	0.08 0.03	−10.62
34	NGC 4565	12.05	351	0.04	2.56	11.14 0.01	10.88 0.09	9.18 0.02	8.99 0.01	2.58 0.89	1.67 0.66	−10.47
35	Maffei 2	2.79	81	0.07	3.57	10.42 0.01	10.07 0.08	8.93 0.01	8.82 0.01	1.53 0.53	1.17 0.46	−9.89
36	NGC 4631	7.35	214	0.19	3.84	10.63 0.01	9.98 0.09	9.30 0.01	9.27 0.01	3.26 1.13	2.95 1.16	−9.46
37	M60	17.36	505	−0.05	0.68	11.60 0.01	11.56 0.10	7.64 1.61	8.14 0.11	0.11 0.04	0.27 0.11	−12.52
38	NGC 4636	14.85	432	−0.07	0.33	11.19 0.01	11.15 0.10	<4.25	7.38 0.22	<0.01	0.06 0.02	<−11.80
39	NGC 2768	20.60	599	−0.03	0.34	11.20 0.01	11.09 0.10	<4.54	7.46 0.18	<0.01	0.07 0.03	<−11.83
40	NGC 3585	18.14	528	−0.07	0.25	11.31 0.01	11.26 0.10	<4.43	7.30 0.34	<0.01	0.05 0.02	<−11.74
41	ESO 270-G017	15.37	447	0.01	2.43	10.24 0.01	10.04 0.10	8.21 0.04	8.31 0.03	0.36 0.13	0.40 0.16	−10.48
42	M51a	9.12	265	0.11	3.81	11.16 0.01	10.71 0.09	9.79 0.01	9.66 0.01	8.77 3.04	6.77 2.65	−9.77
43	NGC 3115	9.64	280	−0.02	0.33	11.03 0.01	10.91 0.10	<3.88	6.87 0.48	<0.01	0.02 0.01	<−11.22
44	NGC 3923	20.08	584	−0.10	0.15	11.52 0.01	11.47 0.10	<4.51	<4.22	<0.01	<0.01	<−10.82
45	NGC 4365	21.68	631	−0.11	−0.37	11.46 0.01	11.42 0.10	<4.58	<4.28	<0.01	<0.01	<−10.76
46	NGC 1313	4.12	120	0.05	3.30	9.86 0.01	9.55 0.09	8.24 0.02	8.37 0.02	0.38 0.13	0.45 0.18	−9.97
47	M84	17.70	515	−0.03	0.12	11.50 0.01	11.41 0.10	<4.40	7.04 0.97	<0.01	0.03 0.01	<−11.42
48	NGC 0185	0.64	19	−0.04	0.89	8.43 0.01	8.35 0.09	5.22 0.29	5.13 0.07	<0.01	<0.01	<−9.48
49	NGC 6946	5.89	171	0.16	3.91	10.84 0.01	10.26 0.09	9.52 0.01	9.46 0.01	5.14 1.78	4.43 1.74	−9.55
50	NGC 1395	22.03	641	−0.07	0.28	11.40 0.01	11.36 0.10	<4.59	7.40 0.34	<0.01	0.06 0.02	<−11.83
(b)												
51	IC 0010	0.77	22	0.03	2.73	9.10 0.01	8.87 0.08	7.22 0.02	7.42 0.01	0.05 0.02	0.06 0.02	−10.17
52	NGC 4517	10.63	309	0.08	3.15	10.51 0.01	10.13 0.09	8.83 0.01	8.72 0.01	1.27 0.44	0.94 0.37	−10.02
53	NGC 1291	10.54	307	−0.05	1.20	11.18 0.01	11.12 0.01	8.33 0.12	8.19 0.05	0.46 0.16	0.31 0.12	−11.46
54	NGC 2683	8.47	246	0.03	2.37	10.70 0.01	10.45 0.09	8.64 0.02	8.29 0.02	0.87 0.30	0.38 0.15	−10.51
55	NGC 4697	10.50	305	−0.05	0.22	10.94 0.01	10.90 0.10	<3.95	7.26 0.17	<0.01	0.04 0.02	<−11.67
56	NGC 3521	8.60	250	0.09	3.40	11.00 0.01	10.61 0.09	9.44 0.01	9.26 0.01	4.37 1.51	2.92 1.14	−9.97
57	NGC 3109	1.25	36	−0.02	1.35	8.30 0.01	8.18 0.10	5.60 0.09	<1.80	<0.01	<0.00	<−9.23
58	NGC 0891	7.09	206	0.19	3.37	10.81 0.01	10.16 0.09	9.28 0.01	9.13 0.01	3.16 1.09	2.20 0.86	−9.66
59	M85	14.38	418	−0.04	0.38	11.27 0.01	11.21 0.10	<4.22	7.63 0.15	<0.01	0.10 0.04	<−12.03

Table 3
(Continued)

iS	Galaxy	d (Mpc)	Beam (pc)	$1-2$ (mag)	$2-3$ (mag)	$\log L_{W1}$ ($L_{\odot,W1}$)	$\log M_\star$ ($M_\odot$)	$\log \nu L_3$ ($L_\odot$)	$\log \nu L_4$ ($L_\odot$)	SFR$_{W3}$ ($M_\odot$ yr^{-1})	SFR$_{W4}$ ($M_\odot$ yr^{-1})	$\log$ sSFR (yr^{-1})
(1)	(2)	(3)	(4)	(5)	(6)	(7)	(8)	(9)	(10)	(11)	(12)	(13)
60	NGC 4244	4.21	122	0.04	2.29	9.55 0.01	9.29 0.09	7.46 0.03	7.49 0.03	0.08 0.03	0.07 0.03	−10.38
61	NGC 4762	13.86	403	−0.05	0.42	10.71 0.01	10.66 0.10	<4.19	6.80 0.27	<0.01	0.02 0.01	<−11.22
62	NGC 5084	17.88	520	−0.03	1.41	11.06 0.01	10.95 0.09	8.41 0.09	8.27 0.04	0.54 0.19	0.36 0.14	−11.22
63	NGC 5907	17.06	496	0.11	3.15	11.16 0.01	10.72 0.09	9.50 0.01	9.33 0.01	4.92 1.70	3.39 1.33	−10.03
64	NGC 4395	4.51	131	−0.04	2.47	9.50 0.01	9.42 0.01	7.46 0.04	7.62 0.04	0.08 0.03	0.09 0.04	−10.52
65	NGC 1407	25.41	739	−0.09	0.34	11.63 0.01	11.59 0.10	<4.72	6.62 3.39	<0.01	<0.01	<−11.06
66	NGC 3627	10.02	291	0.10	3.45	11.09 0.01	10.67 0.09	9.56 0.01	9.51 0.01	5.49 1.90	4.97 1.95	−9.93
67	NGC 4438	11.32	329	0.01	1.57	10.69 0.01	10.49 0.09	8.19 0.06	8.06 0.03	0.34 0.12	0.23 0.09	−10.96
68	NGC 1365	17.92	521	0.28	3.65	11.38 0.01	10.70 0.09	10.01 0.01	10.19 0.01	13.62 4.72	20.39 8.00	−9.56
69	NGC 2903	9.98	290	0.08	3.55	11.02 0.01	10.64 0.09	9.52 0.01	9.46 0.01	5.07 1.76	4.42 1.74	−9.94
70	NGC 5846	25.23	734	−0.06	0.10	11.54 0.01	11.50 0.10	<4.71	<4.42	<0.01	<0.00	<−10.82
71	NGC 4725	12.74	371	−0.03	2.20	11.08 0.01	10.98 0.09	8.91 0.03	8.68 0.02	1.50 0.52	0.86 0.34	−10.80
72	NGC 1549	17.66	514	−0.09	0.54	11.22 0.01	11.18 0.10	<4.40	7.45 0.20	<0.01	0.07 0.03	<−11.88
73	WLM	0.94	27	−0.08	0.64	7.68 0.01	7.64 0.10	<1.90	5.23 0.16	<0.01	0.00 0.00	<−8.44
74	NGC 2841	14.08	410	−0.01	2.16	11.22 0.01	11.09 0.09	9.04 0.03	8.91 0.01	1.93 0.67	1.40 0.55	−10.80
75	Circinus	4.21	122	0.61	4.07	10.85 0.01	10.17 0.08	9.79 0.01	9.80 0.01	8.79 3.04	8.98 3.52	−9.23
76	NGC 3621	7.01	204	0.13	3.66	10.46 0.01	9.95 0.12	9.03 0.01	8.87 0.01	1.89 0.65	1.29 0.51	−9.68
77	NGC 5078	31.13	906	0.05	2.64	11.59 0.01	11.30 0.09	9.67 0.02	9.50 0.01	6.94 2.40	4.80 1.88	−10.46
78	NGC 1023	10.41	303	−0.05	0.37	10.89 0.01	10.85 0.10	<3.94	7.03 0.24	<0.01	0.03 0.01	<−11.46
79	NGC 7331	14.72	428	0.08	3.28	11.37 0.01	11.01 0.09	9.75 0.01	9.59 0.01	8.19 2.84	5.79 2.27	−10.09
80	M64	10.02	291	0.00	2.26	11.24 0.01	11.06 0.09	9.11 0.03	9.02 0.01	2.25 0.78	1.78 0.70	−10.70
81	M59	16.32	475	−0.08	0.61	11.12 0.01	11.08 0.10	<4.33	7.43 0.16	<0.01	0.06 0.03	<−11.86
82	NGC 4696	36.83	1071	−0.06	0.36	11.74 0.01	11.70 0.09	<5.04	7.98 0.20	<0.01	0.20 0.08	<−12.40
83	M82	3.70	108	0.45	4.58	10.81 0.01	10.13 0.10	9.89 0.01	10.29 0.01	10.68 3.70	25.27 9.91	−9.10
84	ESO 274-001	3.18	93	−0.03	1.28	9.15 0.01	9.06 0.09	6.40 0.11	7.31 0.01	<0.01	0.05 0.02	−11.06
85	M77	10.28	299	1.71	3.57	11.49 0.01	10.81 0.10	10.67 0.01	10.51 0.01	52.00 18.00	40.60 15.90	−9.09
86	NGC 3077	3.82	111	0.08	2.71	9.75 0.01	9.37 0.09	7.88 0.02	8.03 0.01	0.19 0.06	0.22 0.09	−10.09
87	M65	12.65	368	−0.02	1.82	11.15 0.01	11.02 0.09	8.78 0.04	8.60 0.02	1.14 0.40	0.73 0.29	−10.97
88	NGC 7213	26.66	776	0.08	2.14	11.53 0.01	11.17 0.10	9.38 0.03	9.37 0.03	3.87 1.34	3.64 1.44	−10.58
89	IC 0356	11.75	342	−0.02	2.20	11.14 0.01	11.02 0.09	8.97 0.03	8.87 0.02	1.69 0.59	1.30 0.51	−10.79
90	NGC 1560	3.01	88	−0.08	1.04	8.83 0.01	8.79 0.09	5.77 0.20	6.22 0.03	<0.01	<0.01	<−10.79
91	NGC 2663	28.49	829	−0.09	0.03	11.69 0.01	11.65 0.09	<4.82	8.00 0.17	<0.01	0.21 0.08	<−12.43
92	NGC 4216	15.50	451	−0.02	2.22	11.12 0.01	11.00 0.09	8.96 0.03	8.71 0.02	1.65 0.57	0.93 0.36	−10.78
93	NGC 1055	14.16	412	0.12	3.60	10.88 0.01	10.42 0.09	9.42 0.01	9.27 0.01	4.18 1.45	3.01 1.18	−9.80
94	NGC 5170	22.07	642	0.02	2.26	11.00 0.01	10.79 0.09	8.89 0.03	8.70 0.02	1.42 0.49	0.90 0.35	−10.64
95	M98	15.98	465	0.03	2.91	11.01 0.01	10.77 0.09	9.20 0.02	9.03 0.01	2.70 0.94	1.82 0.71	−10.34
96	NGC 2997	11.32	329	0.11	3.73	10.93 0.01	10.49 0.09	9.52 0.01	9.40 0.01	5.08 1.76	3.88 1.52	−9.79
97	NGC 4125	21.99	640	−0.04	0.44	11.35 0.01	11.28 0.10	<4.59	7.79 0.12	<0.01	0.13 0.05	<−12.18
98	NGC 7793	3.95	115	0.08	3.27	9.88 0.01	9.51 0.09	8.26 0.01	8.09 0.01	0.40 0.14	0.25 0.10	−9.91
99	NGC 5363	20.30	591	−0.02	1.02	11.29 0.01	11.16 0.10	8.28 0.18	8.29 0.04	0.42 0.14	0.38 0.15	−11.54
100	NGC 4217	18.57	540	0.16	3.34	10.93 0.01	10.35 0.09	9.38 0.01	9.20 0.01	3.85 1.33	2.59 1.02	−9.76
⋯	IC 1613	0.73	21	−0.19	<3.30	7.63 0.01	7.58 0.10	<1.63	<1.34	<0.01	<0.01	<−8.58
⋯	M32	0.82	24	−0.05	0.69	9.12 0.01	9.07 0.09	5.27 1.24	5.55 0.12	<0.01	<0.01	−11.07
⋯	UGC 05373	1.42	41	0.11	<2.79	7.70 0.01	7.25 0.10	<2.21	5.07 0.14	<0.01	<0.01	<−6.91
⋯	ESO 245-007	0.43	13	−0.22	<1.39	6.14 0.01	6.10 0.14	<1.17	<2.58	<0.01	<0.01	<−6.95

Note. (a) Columns: (1) order of *W1* (3.4 μm) angular size; (2) galaxy name; (3) distance; (4) physical resolution based on 6″ beam; (5) *W1–W2* color; (6) *W2–W3* color; (7) *W1* in-band luminosity; (8) stellar mass derived from $\log L_{W1}$ and the color-dependent mass-to-light; (9) and (10) *W3* and *W4* spectral luminosities, $\log \nu L_\nu$, after subtraction of the stellar continuum; (11) and (12) TIR SFRs based on *W3* and *W4*. (b) Columns: (1) order of angular size; (2) galaxy name; (3) distance; (4) physical resolution based on 6″ beam; (5) *W1–W2* color; (6) *W2–W3* color; (7) *W1* in-band luminosity; (8) stellar mass derived from $\log L_{W1}$ and the *W1–W2* color-dependent mass-to-light; (9) and (10) *W3* and *W4* spectral luminosities, $\log \nu L_\nu$, after subtraction of the stellar continuum; (11) and (12) *W3* and *W4* SFRs; (13) specific SFR(W3).

(This table is available in machine-readable form.)

(Taylor et al. 2011). The relation is reproduced here,

$$\log_{10} M_\star/L_{W1} = -2.54(W1 - W2) - 0.17, \quad (2)$$

where L_{W1} $(L_{\odot,W1}) = 10^{-0.4(M-M_{\odot,W1})}$, M is the absolute magnitude of the source in *W1*, and $M_{\odot,W1} = 3.24$ mag is the *W1* in-band solar value; see Jarrett et al. (2013). We place

floor-to-ceiling limits on the *W1–W2* color, −0.05 to 0.2 mag —corresponding *M/L* ranging from 0.21 to 0.91—to minimize the contaminating effects of AGN light, as well as unphysical blue colors due to low S/N in the *W2* band (relative to the more sensitive *W1* band). For those dwarf galaxies with only *W1* detections or colors with S/N ⩽ 3, we adopt an *M/L* value of
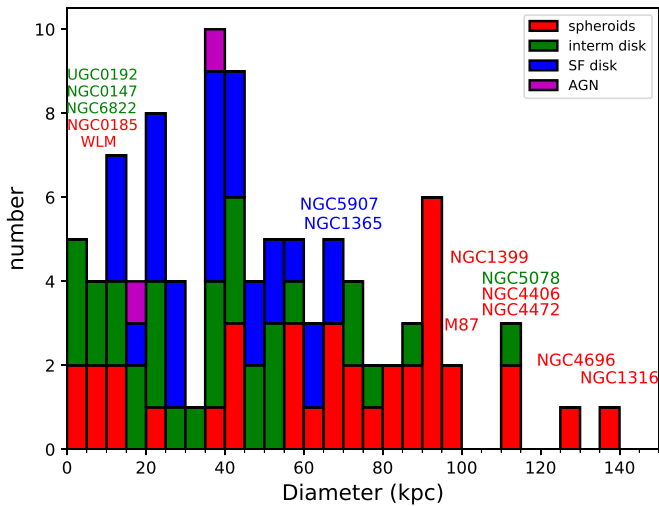
Figure 14. Physical size (kpc) distribution for the 100 largest (angular) galaxies, based on the infrared *W1* (3.4 μm) size. The galaxies are group-delineated by their *WISE* colors (see Figure 10), with notable galaxies labeled.

Figure 15. Stellar mass distribution for the 100 largest galaxies. The galaxies are group-delineated by their *WISE* colors (see Figure 10), with a few of the exceptional ones labeled.

0.6 (Kettlety et al. 2018). In general, adopting a single *M/L* between 0.5 (for disky galaxies; see Ponomereva et al. 2017) and 0.7 (bulge-dominated types; see Cluver et al. 2014) is a good strategy for estimating the stellar mass using *WISE W1* (3.4 μm) light.

The distribution of stellar mass is presented in Figure 15, with the sample delineated by color as before. Unsurprisingly, the largest-diameter galaxies are also the most massive. These bulge-dominated early-type systems typically have values $>10^{11}\ M_\odot$. In terms of stellar mass, the most massive galaxy is NGC 1316 (Fornax A), weighing in at $5.2 \times 10^{11}\ M_\odot$, which is nearly an order of magnitude larger than the Milky Way at $6 \times 10^{10}\ M_\odot$ (Licquia & Newman 2015). At the other extreme, the dwarf spheroids have $\log M_\star$ values that range between 7.5 and 8.5. The least-massive galaxies, 6–7, are the very low surface brightness dwarfs (e.g., ESO 245-007), which are only visible to *WISE* in the local volume, $d < 10$ kpc. The Magellanic Clouds are in the upper dwarf range (8.5–9.0). Intermediate disks, such as M81 ($\log M_\star = 10.85$) and M31 (10.96), are the second most massive population (but also have a "dwarf" population near 9.4), followed by the late-type SF disks, which tend to have $\log M_\star < 10.5$ and are clearly still building their disks (see SFR and specific SFR below and in Table 2). The Milky Way falls within the intermediate range, with an estimated $\log M_\star = 10.78$ (Licquia & Newman 2015), somewhat smaller than its sister galaxy, M31.

5.4. Star Formation Activity

The ISM-sensitive bands of *WISE*, *W3* (12 μm) and *W4* (23 μm), are effective tracers of the dust-obscured SF activity (Jarrett et al. 2013; Cluver et al. 2014, 2017). It turns out that *W3* is particularly effective, because not only is it far more sensitive than the 23 μm band but it better traces the total infrared luminosity and appears to be robust to metallicity variation. This is largely attributable to the breadth of the *W3* band, resulting in it being dominated by the dust continuum and less susceptible to emission line and PAH variations
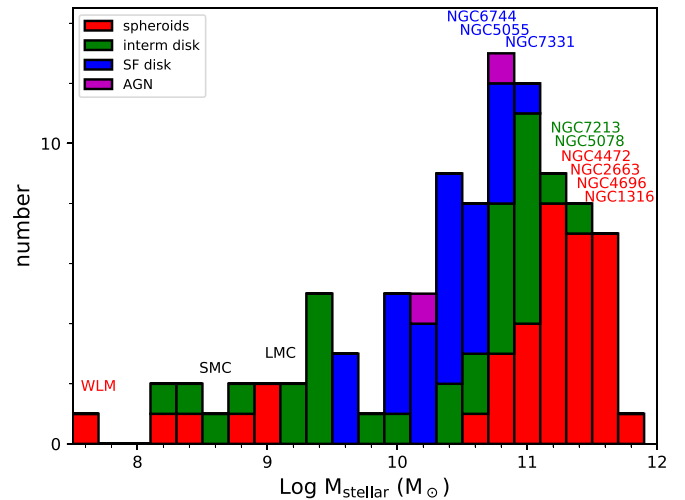
(Cluver et al. 2017), compared to, for example, the *Spitzer*-IRAC 8 μm band. We should stress that galaxies with little to no dust emission or, alternatively, very low metallicities will have correspondingly low SFRs based on the infrared emission. It is more appropriate to use Hα and UV tracers of SF for such galaxies, which may be particularly important for dwarf galaxies.

In the low-z universe, the *W3* 12 μm band includes contributions from the warm $T \sim 150$ K dust continuum; the 7.7, 8.5, and 11.3 μm PAHs; and the 12.8 μm [Ne II] and 15.7 μm [Ne III] emission features. It is thus sensitive to SF activity (but also metallicity), as well as a small fraction of stellar light (R-J tail). Although our sample does not contain any extreme IR-bright galaxies, the closest being NGC 1068, we should note that the band also contains a 10 μm silicate absorption, which is clearly present in the spectra of heavily dust-obscured galaxies, such as Arp 220. Cluver et al. (2017) did observe that LIRGs and ULIRGs have a slightly different SFR relation compared to normal galaxies, likely indicative of the extreme dust and ice(s) absorption. For these extreme IR-bright galaxies, we recommend using the 23 μm *W4* band.

Relative to the near-IR bands of *WISE*, *W1* and *W2*, the mid-IR *W3* and *W4* bands are not nearly as sensitive; this particularly affects stellar continuum– (bulge-) dominated systems with predominately R-J emission at these wavelengths. Hence, SF activity can only be measured for (1) relatively nearby galaxies or (2) relatively dusty galaxies. The LIRGs can be detected to high redshift (e.g., the Hyper-LIRGs discovered by *WISE*; see Tsai et al. 2015). There are cases where the *W3* flux is easily detected, but after subtraction of the stellar continuum (estimated from the *W1* flux), there is nothing left representing the ISM emission (e.g., NGC 2768). Nevertheless, for most of the largest galaxies in the sky and WXSC galaxies within $z < 0.1$, SF activity can be estimated using *WISE*.

We employ the latest SFR calibration based on the total infrared luminosity—and adopting a Kroupa (2002) initial mass function (IMF)—of a varied sample of nearby systems from the SINGS (Kennicutt et al. 2003) and KINGFISH (Kennicutt et al. 2011) surveys, correlated to the corresponding mid-infrared luminosities (Cluver et al. 2017). The general

prescription is that the 12 and 23 μm SFRs are derived from the spectral luminosities, νL_ν, where ν is the bandpass central frequency and normalized by the bolometric luminosity of the Sun.[12]

The total infrared SFR scaling relations of Cluver et al. ([2017](#)) are given by

$$\begin{aligned}\text{Log}_{10}\ \text{SFR}_{\text{TIR}}(M_\odot\ \text{yr}^{-1}) &= 0.873(\pm 0.021)\\ &\times \text{Log}_{10}\ \nu L_{12\,\mu\text{m}}(L_\odot) - 7.62(\pm 0.18),\end{aligned} \quad (3)$$

$$\begin{aligned}\text{Log}_{10}\ \text{SFR}_{\text{TIR}}(M_\odot\ \text{yr}^{-1}) &= 0.900(\pm 0.027)\\ &\times \text{Log}_{10}\ \nu L_{22\,\mu\text{m}}(L_\odot) - 7.87(\pm 0.24),\end{aligned} \quad (4)$$

where $\nu L_{12\,\mu\text{m}}$ and $\nu L_{22\,\mu\text{m}}$ are the spectral luminosities normalized by the solar luminosity ($L_\odot$) and the stellar continuum removed using the *W1* luminosity as a proxy for the stellar continuum as follows: 15.8% in the *W3* band and 5.9% in the *W4* band (see Cluver et al. [2017](#) for details). Note that the relation uncertainties, in particular the offsets, render an SFR accuracy of, at minimum, 20%–25%, but can be several percent higher when propagating the formal photometric errors. Moreover, and as noted earlier, the mid-IR SFRs are based on the warmed ISM that arises from dust-obscured star formation, which does not account for unobscured UV emission from young stars that manages to escape the host galaxy.

The SFRs and stellar masses for each galaxy are presented in Table [3](#), which includes the redshift-independent or luminosity distance (column 3), physical resolution (column 4), colors (columns 5 and 6), continuum-subtracted spectral luminosities (columns 7 and 8), *W1* in-band luminosity (column 9), estimated stellar mass (column 10), and total infrared (TIR) SFRs from the *W3* and *W4* (columns 11 and 12) spectral luminosities. Here the spectral luminosities, with the stellar subtraction, represent the 12 μm aggregate and 23 μm dust emission after stellar continuum subtraction. Finally, the specific SFR (column 13) is the SFR normalized by the stellar mass.

To graphically show the SFR results, we relate the SFRs (based on the *W3* relation) with the corresponding host stellar masses, creating the so-called galaxy star formation "main sequence" (galactic main sequence, hereafter referred to as the Galactic main sequence (GMS); Figure [16](#)). This GMS gives a crude representation of the past-to-present star formation history in which ever-larger SFRs track with ever-larger stellar masses, which appears to hold even at higher redshifts (see, for example, Elbaz et al. [2007](#); Noeske et al. [2007](#); Bouch'e et al. [2010](#)). The slope of the sequence therefore represents a secular evolution path, with deviations due to events from interactions, bar formation, AGN and superwind feedback, and starburst and quenching events. For reference, we show lines of constant specific star formation ratio (sSFR = SFR/mass; column 13 of Table [3](#)) ranging from 10^{-13} to 10^{-9} yr^{-1}, covering the range that is seen for nearby galaxies, from active building (10^{-9}–10^{-10}) to semi-quiescent (10^{-10}–10^{-11}) and quenched or depleted ($<10^{-11}$).

To put the largest 100 galaxies into context, we show the results for the larger WXSC sample, some 5000 galaxies, contours coded by color classification as before, and the overall trend in the GMS derived from a higher-redshift (z complete up to 0.3) sample from the GAMA G12 region (Jarrett et al. [2017](#)).
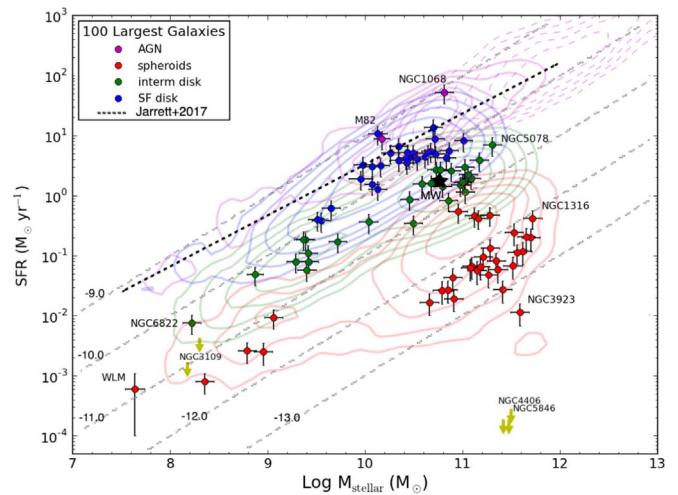
---

[12] We note that the spectral luminosity is different from the in-band luminosity due to the bolometric versus *W1* in-band normalization. See Jarrett et al. ([2013](#)).

Figure 16. GMS: SFR (based on *W3*, Equation ([3](#))) vs. stellar mass sequence for the 100 largest galaxies (points and error bars) and the bright galaxy sample from the WXSC (contours, where the higher redshifts are magenta dashed contours, tracking the AGN). The data are delineated by their *WISE* colors (Figure [10](#)) and generally fall below the sequence derived from a more distant (and luminous) sample as defined by the GAMA G12 region (Jarrett et al. [2017](#); dashed line). The Milky Way (black star symbol) is located in the central spread of the "intermediate" disk galaxies (green points and contours). The faint dashed lines represent lines of constant log sSFR = -13, -12, -11, -10, and -9.0 yr^{-1}.

A number of interesting features are seen in Figure [16](#). The dusty galaxies with their strong *W3* emission (blue points) are generally massive in stars, $\log M_\star > 10$, and relatively high (>2) SFRs, defining the upper end of the sequence. A maximum SFR is reached where the disk galaxies appear to turn over at a stellar mass of $\log M_\star$ between 10.4 and 10.7, perhaps signifying a gas-depletion phase. Sitting well above the sequence is the starburst galaxy M82, clearly demonstrating how young (megayear) starburst events move galaxies upward, outpacing the stellar mass gigayear buildup timescale. The highest-SFR galaxy is NGC 1068 (see also the Circinus Galaxy), which represents an upper limit, since the AGN accretion emission from hot dust is heavily boosting the *WISE* fluxes; even more luminous galaxies with AGNs (e.g., Mrk 231; see Cluver et al. [2017](#)) move along this upper AGN sequence, as represented by the dashed magenta contours (in the top right of the diagram). In this way, neither the SFR nor the stellar mass of mid-infrared AGNs is properly measured or modeled with simple *WISE* fluxes and colors.

As galaxies build their mass and consume their gas, they move to the right and down from the SF sequence, as demonstrated by the intermediate disk galaxies (green points and contours). The Andromeda (M31), M81, and Milky Way values from Licquia & Newman ([2015](#)) are example galaxies that have built the bulk of their stellar backbone while continuing to form stars at a relatively semi-quiescent rate, $\sim$1–2 $M_\odot$ yr^{-1}. The final evolutionary sequence is dominated by the spheroidals (red points), with examples of dwarf ($<10^9\ M_\odot$) and massive ($>10^{11}\ M_\odot$) varieties in the 100 largest galaxies, whose SF rates are several orders of magnitude smaller than those of disk galaxies, and correspondingly low specific SFRs ($<10^{-12}$ yr^{-1}). Presumably, the gas has been depleted—or accretion shutdown, so-called strangulation (Peng et al. [2015](#))—halting the SF and creating a downward descent from the GMS, reaching a peak in stellar mass around

$\log M_{\star}(M_{\odot}) \sim 11.5$. The SF activity is so low for many of these early types that no *WISE W3* emission is detected; hence, only upper limits are indicated in the GMS plot, for example, the heart of Virgo, NGC 4406 (M86). As previously noted, galaxies with low dust content may poorly trace the ongoing SF that is better detected and traced using UV *GALEX* imaging or Hα spectro-imaging, optimally in combination with infrared to produce a complete view of the SF activity in galaxies (see, e.g., Leroy et al. 2019).

In Figure 16, we can also compare the GMS of the bright and nearby galaxy with that of a deep and complete redshift survey (dashed line), GAMA G12 $z < 0.3$ (Jarrett et al. 2017). Dwarf spheroidals, such as NGC 0185, have the lowest SFRs, 1 or 2 orders lower than the low-mass dwarfs in G12. It should be noted that G12 is optically selected (r band) and preferentially finds redshifts of emission line systems at ever-larger distances (hence, relatively unobscured SF disk galaxies, which would have higher SFRs than dwarf spheroidals). The corresponding specific SFRs of the dwarf spheroids are quite long, $>10^{-11}$ yr^{-1}, confirming their quiescent state. The late-type SF galaxies, such as M83, unsurprisingly have the highest SFRs and lie within the G12 sequence (i.e., consistent with the GAMA selection), with $>10^{-9}$ yr^{-1} rapid-building rates. In the 100 largest sample, the most rapidly building galaxy is M82; its current starburst phase is perhaps just one of many that will occur in its lifetime. Meanwhile, the massive, high surface brightness spheroids, such as NGC 4696, have rapidly declining specific SFRs, 10^{-12} yr^{-1}, indicating that they are "dead," having consumed their gas and fallen off the sequence long ago.

6. WXSC

6.1. The Largest Angular Size Galaxies

We have presented the largest galaxies in the sky based on the angular apparent size as measured in the mid-infrared. Compared to large (>5000) samples of bright nearby galaxies, the 100 largest have physical properties that are generally unremarkable. Nevertheless, because these galaxies are either LG members or tend to be very close to the Milky Way, <50 Mpc, we have access to the lowest-mass satellites and dwarf galaxies (e.g., NGC 6822, NGC 3109), while also being graced by two galaxy clusters that have some singularly large galaxies (e.g., Fornax A and Virgo A and many other BCGs, such as M86).

We have shown that the apparent mid-IR colors have distinct trends that can be exploited to discern galaxies in different states of their star formation history, including semi-quiescent/passive types (intermediate or green valley disks), actively building SF types (late-type disks), "dead" and gas-poor types (spheroidals), and even incredibly slow yet building types (dwarf spheroidals). There are two standout galaxies with AGNs, NGC 1068 and Circinus, both of which have extraordinarily high surface brightnesses, several magnitudes brighter than typical galaxies, indicative of their intense nuclear activity. In the following, we discuss how the 100 largest and the greater WXSC can be used to further our understanding of galaxy evolution.

6.2. Legacy of Large Galaxy Archives

The 100 largest are interesting in the sense that they are nearby and may be studied in precise—resolution and multi-wavelength—detail; they can have very small physical sizes or be giants that live within dense environments. This special sample is but a small set of a much larger one that is being constructed, the whole-sky WXSC, which will have tens of thousands of galaxies drawn from the local universe, many of which are legacy galaxies from early surveys such as the Messier and NGC (RC3) catalogs, but also fainter galaxies that enter the realm (targets) of large-area spectroscopic surveys such as SDSS-V (in the north; Kollmeier et al. 2017) and Taipan (in the south; da Cunha et al. 2016).

The legacy extragalactic data from the WXSC are timely, particularly in the southern hemisphere, given the historic paucity of studies below the equator and the rapid rise of large telescopes in the south. The Square Kilometre Array (SKA), for example, is driving radio surveys of the southern hemisphere, first through the pathfinders (e.g., ASKAP and MeerKAT, both now underway) and later next decade by the SKA itself. These future surveys notably target the early universe but will sweep across the sky, image the local universe with clarity (resolution) and quality (S/N), and range across the vast mass spectrum of galaxies that is so pivotal in connecting how baryons are cycled through the cosmic web to halos and into galaxies.

The goal of the WXSC archive is to make available data products that are directly useful to these surveys, including source catalogs of global properties, large-area imaging showing the environments of galaxies, internal measurements (bulge–disk decompositions), and diagrams that summarize physical characteristics. Ultimately, our aim is to measure all resolved galaxies as discerned in the *W1* (3.4 μm) band, estimated to be 1–2 million galaxies, which may be combined with the ALLWISE point-source catalog (Cutri et al. 2012) and the deeper CATWISE catalog (Eisenhardt et al. 2019) to form a complete whole-sky census of galaxies down to 15 μJy and sensitive to early galaxy formation at redshifts beyond 1.

The 100 largest and WXSC are comprised of several data products—images, profiles, SEDs, and tables—that fully characterize the measurements from *WISE*. As part of a value-added effort to compare and contrast across galaxy properties, we create graphic diagrams that depict the key global measurements and derived values—colors, surface brightness, size, SFR—with the goal to be able to categorize and discern groups of galaxies that have similar properties and SF histories. We refer to these as "pinwheel" diagrams, described below.

6.3. Galaxy Physical Properties: The Pinwheel Diagram

Inspired by the "starfish" diagrams created for the SAMI survey of galaxies (see, e.g., Konstantopoulos 2015), we have constructed a polar-wedge schematic for each galaxy, which we will refer to as pinwheel diagrams. For a given attribute, e.g., SFR, the goal is to convey the value relative to some average or typical value observed for a large sample. In this way, the circular pinwheel can graphically show many attributes at once, conveying a signature pattern for that galaxy. We can then use that pattern, for example, to match against other galaxies in order to associate similar kinds of galaxies or those in comparable phases of their stellar population evolution.

An example of the pinwheel diagram for the barred Fornax spiral galaxy NGC 1365 is shown in Figure 17 (top panel). The six attributes that make the pinwheel are the following: mid-IR colors [*W1*–*W2*] and [*W2*–*W3*], effective surface brightness (SBe), stellar mass ($\log M_{\star}$), diameter (D[kpc]), and SFR (log SFR). Starting from the center, 0% departure from average, circular rings indicate the 50% and 100% departure
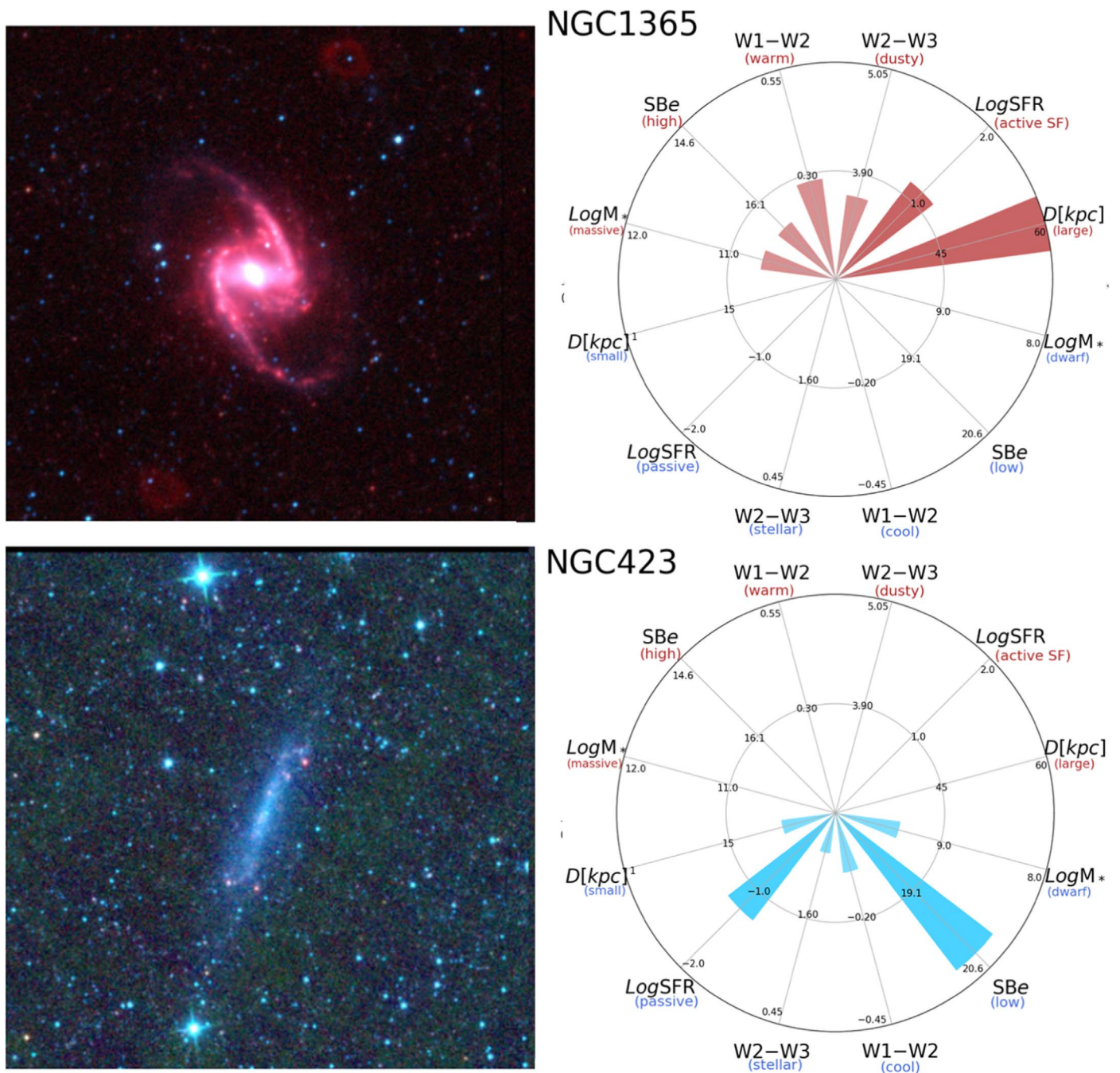
Figure 17. Physical properties of barred spiral NGC 1365 (top panels) and low surface brightness, highly inclined galaxy NGC 4236 (bottom panels). The composite diagram shows the (left) *WISE* three-color view of the galaxy, and the (right) pinwheel diagram graphically displays the physical properties, with the center of the diagram representing the average values for the galaxies (see Table 4). The inner and outer rings indicate the 50% and 100% departures from the canonical average values. In this example, NGC 1365 exhibits "positive" attributes: active SF and colors and massive and extended host. In contrast, the galaxy NGC 4236 has "negative" properties: minimal SF, low surface brightness, and dwarf-like mass and extent.

values of the parameter from the typical value. The center of the diagram represents the median values for galaxies in the WXSC (defined in Table 4), and so departures from the average value indicate either positive departure (upper half of diagram) or negative departure (lower half). For example, galaxies with a large SFR will have a red wedge pointing upward toward "active SF," whereas galaxies with low log SFRs will have a blue wedge pointing downward toward "passive." In the case of NGC 1365, it has large-valued colors indicating active star formation and somewhat high surface brightness, and it is more massive and larger in diameter than typical galaxies. In the

Fornax cluster, NGC 1365 stands out among its many cluster members.

In contrast, the faint galaxy, NGC 4236 in Figure 17 (bottom panels), has "negative" properties, including low (dwarf) mass, low surface brightness, low SFR, and cool colors; indeed, there is not much going on in this physically small galaxy, but it may be quite typical for its stellar mass and evolutionary star formation history phase. It is immediately apparent that NGC 1365 and NGC 4236 could not be more different galaxies in their measured and derived properties, visually (and easily) discerned with the pinwheel diagram.

Table 4
Pinwheel Diagram Reference Center

Attribute	Units	Median Value	Floor (min)	Ceiling (max)
…	…	…		
D	kpc	30	1	90
log SFR	$\log [M_\odot \ \mathrm{yr}^{-1}]$	0	−2.0	+2.0
$W2$–$W3$	(mag)	2.75	0.45	5.05
$W1$–$W2$	(mag)	0.05	−0.45	0.55
SB_e	mag arcsec^{-2}	17.6	20.6	14.6
$\log M_\star$	$\log [M_\odot]$	10.0	8.0	12.0

Note. The center of the pinwheel diagram has the values presented here; the median values are derived from the larger WXSC, several thousand galaxies. The exception is the central value for the log SFR, adopted to be the approximate value of the Milky Way and its LG companion, M31.

In Paper II, we will present the measurements and derived properties of the WXSC and include pinwheel diagrams for each. We will attempt to identify similar types of galaxies based on the pinwheel patterns, thereby linking their properties to their SF history and environment.

7. The Brightest GCs

For completeness, we include here the brightest Milky Way GCs, since many are also some of the largest and brightest objects in the sky; e.g., 47 Tucanae is a spectacular GC in the SMC field (see also Figure 1), and Omega Centauri (NGC 5139; top panel of Figure 18) is so large that it is effectively a dwarf satellite galaxy. Because we are unable to distinguish foreground (Milky Way) stars from those in the GCs, we measure their fluxes in a similar way as for the Magellanic Clouds. Specifically, we compute the mean flux per pixel of the "sky" (annulus well outside of the GC) and remove that from each pixel value within the GC aperture.

The resulting fluxes are shown in Table 5, which presents the 25 brightest GCs in the sky; all are part of the Milky Way system, and most are famed Messier objects. For simplicity, we use the same circular aperture (column 4) for all four *WISE* bands and report the integrated flux (sky-subtracted) in Vega magnitudes and the enclosed surface brightness. Omega Centauri (top panel of Figure 18) is by far the brightest GC, with an integrated magnitude of +0.84 in *W1* (143 Jy), while the last GC on the list, M72, is 6.2 mag fainter (0.5 Jy). A common property of GCs is their relatively uniform color, due to the dominant population—evolved, low-mass stars—that are the last survivors of these ancient star clusters; note how Omega Centauri and 47 Tucanae (Figure 1) appear homogenous in apparent properties but with the occasional dusty (shell-enshrouded) red giant standing out. Nevertheless, there is a slight spread in color across the 25 brightest GCs, which would reflect the range in GC ages and metallicities accordingly.

For this sample, the mean colors are +0.002 ± 0.011 and −0.101 ± 0.161 for *W1*–*W2* and *W2*–*W3*, respectively, which would land at the extreme "blue" end of the galaxy color plot, indicated in Figure 10. As some of the oldest known objects in the universe, GCs have low-mass, evolved member populations and correspondingly similar colors to spheroidal galaxies. None of the 25 brightest GCs have particularly deviant colors; however, in terms of the morphology or SF activity indicator, *W2*–*W3* color, the GC with the warmest (red) color is NGC 6397 (bottom panel of Figure 18), whose value is +0.56 ± 0.02 mag, about 3σ warmer than the mean color for GCs.
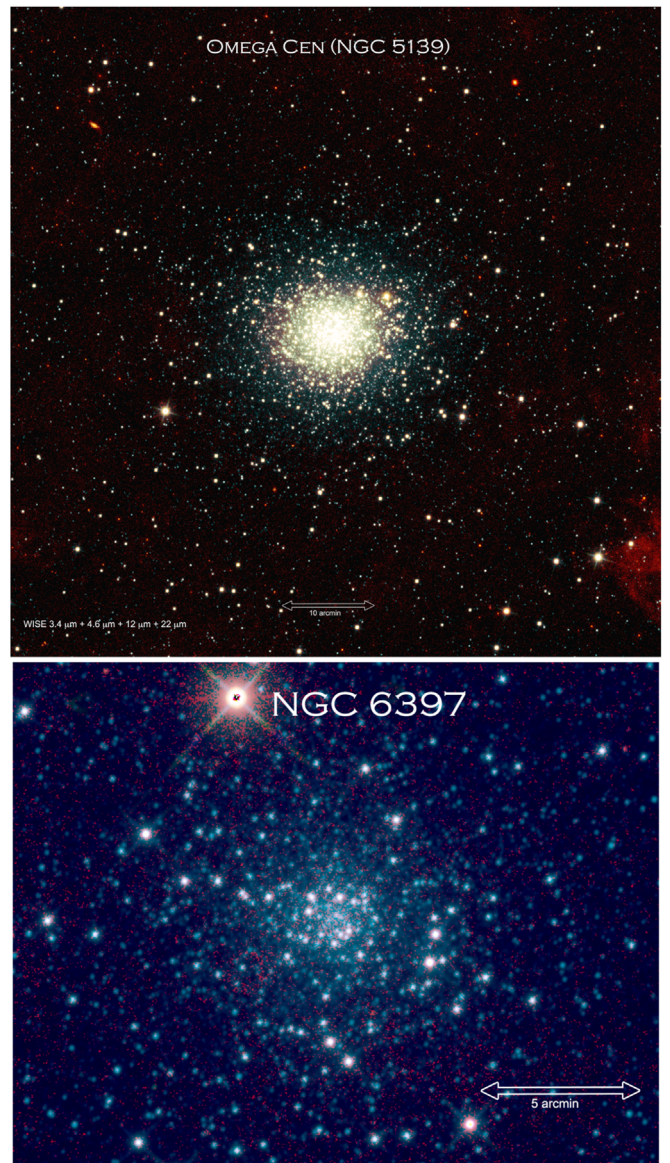

Figure 18. Nearby GCs Omega Centaurus (top) and NGC 6397 (bottom), as seen with *WISE* in all four bands. Omega Cen is the brightest GC and likely a dwarf galaxy; NGC 6397 has unusually "warm" *W2*–*W3* colors for a GC, indicating the presence of 11.3 μm PAH emission and significant dust mass, possibly arising from post-AGB shell ejection from a second generation of stars.

One of the closest GCs relative to the Sun (∼2.2 kpc; Alcaino et al. 1997), NGC 6397 has the typical GC appearance of a strongly contracted core; see the bottom panel of Figure 18. Upon closer inspection of the *W3* (12 μm) band, there is diffuse emission in the inner ∼3′, consistent with the high(est) surface brightness (SBw3) seen in the sample (see Table 5). The presence of 11.3 μm PAH or mid-IR continuum emission indicates significant dust in the inter-GC medium and consequently moves NGC 6397 to the right of the GC mean in the color plot (Figure 10). Possibly arising from post-AGB shell ejection from a second generation of stars (Milone et al. 2012), this dust emission is diffuse and relatively weak (compared to *W1* and *W2*), but the relatively close proximity allows clear detection with *WISE*. Note that M4, the closest GC system to the Sun (also ∼2 kpc), does not indicate any excess *W3* emission—18.08 versus 16.08 mag arcsec^{-2} in comparison to NGC 6397 (see Table 5)—and hence is unlikely to have a significant post-AGB population (see also MacLean et al. 2016).

Table 5
Brightest GCs

Cluster	R.A. (deg)	Decl. (deg)	R_{W1} (arcmin)	$m1 \pm \Delta m1$ (mag)	SB1 (mag s^{-2})	$m2 \pm \Delta m2$ (mag)	SB2 (mag s^{-2})	$m3 \pm \Delta m3$ (mag)	SB3 (mag s^{-2})	$m4 \pm \Delta m4$ (mag)	SB4 (mag s^{-2})
NGC 5139	201.69121	−47.47686	27.50	0.84 0.01	18.17	0.84 0.01	18.17	1.02 0.01	17.03	0.96 0.02	16.71
NGC 0104	6.02233	−72.08144	25.00	1.17 0.01	18.29	1.20 0.01	18.33	1.13 0.01	16.89	0.99 0.01	15.73
M22	279.10086	−23.90341	10.83	1.92 0.01	17.23	1.82 0.01	17.12	1.70 0.01	16.44	−0.25 0.01	14.00
M04	245.89751	−26.52552	9.83	2.72 0.01	17.81	2.61 0.01	17.71	2.99 0.04	18.08	2.22 0.05	16.47
NGC 6397	265.17233	−53.67369	11.67	3.11 0.01	18.58	3.03 0.01	18.50	2.47 0.01	16.43	3.42 0.06	17.38
NGC 2808	138.01060	−64.86282	9.17	3.13 0.01	18.08	3.13 0.01	18.07	2.73 0.01	17.47	1.95 0.01	16.46
NGC 6752	287.71576	−59.98185	10.00	3.16 0.01	18.29	3.13 0.01	18.26	3.26 0.01	18.20	3.67 0.10	18.18
M05	229.64064	2.08268	12.50	3.49 0.01	19.11	3.50 0.01	19.12	3.34 0.01	18.08	3.88 0.04	17.11
M13	250.42139	36.45853	10.83	3.57 0.01	18.88	3.58 0.01	18.89	3.66 0.01	17.91	3.67 0.07	17.63
M10	254.28746	−4.09933	10.17	3.58 0.01	18.75	3.57 0.01	18.74	3.69 0.02	17.94	3.69 0.03	15.81
M14	264.40067	−3.24592	8.75	3.65 0.01	18.50	3.65 0.01	18.49	3.73 0.02	17.36	3.05 0.03	15.80
NGC 0362	15.80930	−70.84821	8.67	3.98 0.01	18.80	3.98 0.01	18.80	3.88 0.01	18.39	3.83 0.05	17.06
M55	294.99750	−30.96208	8.67	4.02 0.01	18.84	4.01 0.01	18.84	4.20 0.01	18.31	5.13 0.19	17.88
M03	205.54803	28.37712	10.83	4.06 0.01	19.37	4.07 0.01	19.38	3.98 0.01	17.61	3.95 0.04	16.70
M15	322.49323	12.16683	9.00	4.13 0.01	19.03	4.12 0.01	19.02	4.14 0.01	18.65	4.47 0.08	17.22
M12	251.81049	−1.94782	8.33	4.14 0.01	18.87	4.14 0.01	18.87	4.43 0.03	18.55	4.27 0.11	17.89
M02	323.36255	−0.82332	7.50	4.15 0.01	18.66	4.16 0.01	18.66	4.29 0.01	17.92	4.21 0.07	16.96
M92	259.28030	43.13652	9.58	4.34 0.01	19.38	4.33 0.01	19.37	4.58 0.02	17.04	4.54 0.04	16.67
M80	244.26045	−22.97511	5.83	4.53 0.01	18.49	4.52 0.01	18.49	4.83 0.03	16.96	4.14 0.04	15.59
M54	283.76364	−30.47850	5.42	4.63 0.01	18.43	4.55 0.01	18.35	4.27 0.01	17.50	3.94 0.04	16.06
M107	248.13298	−13.05363	7.50	4.79 0.01	19.30	4.82 0.01	19.33	5.54 0.10	18.00	7.03 0.54	18.27
M53	198.23013	18.16912	10.42	5.43 0.02	20.66	5.43 0.04	20.66	5.35 0.02	19.32	5.15 0.08	16.87
M79	81.04414	−24.52423	5.17	5.60 0.01	19.30	5.60 0.01	19.30	6.42 0.10	19.17	5.41 0.17	18.15
NGC 0288	13.19106	−26.58730	7.83	5.80 0.01	20.40	5.80 0.01	20.41	5.97 0.03	19.45	6.26 0.43	19.01
M72	313.36630	−12.53706	2.92	7.02 0.01	19.48	7.05 0.01	19.51	7.35 0.03	18.36	7.47 0.35	17.21

Note. Coordinates are in J2000; photometry is with circular apertures, radius R_{W1}; and SB is the mean surface brightness for the photometric aperture.

(This table is available in machine-readable form.)

A detailed analysis of the GC properties is beyond the scope of the present work, but this exercise of measuring the brightest GCs shows that interesting outliers, such as NGC 6397, can be discerned and identified from the general photometric properties.

8. Summary

Building upon the early pilot study of Jarrett et al. (2013), this is the first paper in a series that encompasses the WXSC data release, here showcasing the 100 largest angular diameter galaxies. These objects are unique in that we are able to discern parsec and subkiloparsec scales with high S/N due to their apparent brightness and proximity, notably for the LG ($D < 1$ Mpc) and local volume (<10 Mpc), enabling high-fidelity study of their internal composition and galactic "ecosystem." In this study, we measure their global properties, including flux, surface brightness, and colors, as well as their two-component axisymmetric radial distribution.

The largest of the large are the Magellanic Clouds and the Andromeda galaxy, which are also the (integrated) brightest galaxies in the sky by several orders of magnitude. From their apparent measurements and estimated distance, we derive physical properties such as luminosity, stellar mass, and SFR and compare the largest galaxies with a statistically significant sample of bright nearby galaxies. We have created a visual diagram for each galaxy that simultaneously depicts the key global properties, which we envision using to categorize and group galaxies with common evolutionary traits. Finally, we present the largest and brightest Milky Way GCs and their integrated measurements of size, flux, color, and surface brightness.

To summarize the main results, we have investigated and presented the following.

1. We have constructed a whole-sky atlas of (chiefly) nearby, bright galaxies and GCs called the WXSC. For each source, we have constructed new—deep and wide—mosaics from which to measure and characterize the target galaxy, as well as sources that are nearby in projected radial distance. To date, we have measured over 70,000 sources. For the first release, we choose the largest angular galaxies in the sky, starting from the Magellanic Clouds, to the major LG galaxies such as M31 and M33, to nearby galaxy groups and clusters (Virgo and Fornax). The WXSC will allow us to compare the most well-studied galaxies with large and more distant galaxy samples from *WISE*, *Spitzer*, *Herschel*, *Euclid*, LSST, *JWST*, and the SKA pathfinders.

2. We have measured the global and internal radial brightness properties of the 100 largest galaxies based on the *WISE W1* (3.4 μm) $1 - \sigma_{sky}$ isophotal radius (about 23 mag arcsec^{-2}), which typically reaches axisymmetric-averaged depths of 25 mag arcsec^{-2}, or approximately 28 mag arcsec^{-2} in the AB system. We present the results for angular diameters, integrated flux from isophotes, and "total" extractions from both asymptotic apertures and fitting to the radial profile to levels below the noise, surface brightness, and colors, *W1–W2* and *W2–W3*. The Magellanic Clouds, M31, and M33 are large enough that special methods were required to extract their light from the intervening foreground Galactic emission.

3. Because of the high-quality measurements from the largest and brightest galaxies in the sky (WXSC), the *WISE* color–color diagram reveals a tight sequence that represents galaxy morphology and star formation history, including present-day activity. We use the rest-frame-corrected measurements from the largest and highest-S/N galaxies to fit the functional form of this *WISE* color–color "sequence," given by $(W1 - W2) = [0.015 \times e^{\frac{(W2-W3)}{1.38}}] - 0.08$. Offsets from the sequence arise from the usual photometric scatter and, more meaningfully, from excess infrared emission associated with nuclear activity from AGNs and starbursts.

4. The sample is subdivided by the *WISE* colors, which serve as proxies for four general types of galaxies: bulge-dominated spheroidals, intermediate semi-quiescent disks, SF spirals, and AGN-dominated systems. Physical properties and attributes are computed based on their distance, notably the diameter, aggregate stellar mass, and dust-obscured SFR. We use this classification scheme to study their global properties: effective surface brightness, size, bulge-to-disk ratio, and luminosity. We compare the half-light radii and surface brightnesses between *WISE W1* (3.4 μm) and 2MASS (2.2 μm) measurements, showing that *W1* radii are much larger and surface brightnesses much fainter than those extracted from the less sensitive 2MASS imaging, notably for dwarf and low surface brightness galaxies.

5. We find that the global properties are not remarkable compared to galaxies in the local universe, except in the sense that we can detect and discern the smallest and lowest-mass dwarf and satellite galaxies because of their close proximity. Nevertheless, the 100 largest galaxies include bright cluster galaxies (Virgo and Fornax, which have enormous diameters of >100 kpc, very high B/Ts, and aggregate stellar masses; NGC 1316 is the most massive), starbursts (such as NGC 253 and M82, with SFRs 10 times the rate of the Milky Way), and AGNs (e.g., Circinus and NGC 1068, with surface brightnesses that are so bright that they image-saturate in the mid-IR).

6. In terms of star formation history, the 100 largest galaxies tend to have lower specific SFRs compared to field galaxies and compared to deeper redshift-selected samples, such as those from GAMA G12 (Jarrett et al. 2017).

7. The low-mass end is dominated by dwarf spheroids (e.g., NGC 0185), which have very low SFRs and hence are slowly building their bulge population. Early-type disk galaxies, such as M81, are passively building with rates that fall below the sequence trend. Late-type spirals, such as M83, are actively building with rates perfectly consistent with the star formation history sequence observed in the GAMA G12 study.

8. To efficiently display the attributes that we are capable of estimating with *WISE* measurements, we introduce a "pinwheel" diagram that depicts the physical properties with respect to the median value observed for galaxies in the WXSC. These six attributes are the physical diameter, surface brightness, two colors, SFR, and stellar mass. We show that with this diagram, it is possible to delineate between different kinds of galaxies, identifying those with similar star formation histories, for example. The pinwheel diagrams will be a featured product as part of the WXSC image, catalog, and ancillary data archive.

9. Finally, we present the 25 brightest GCs in the sky, of which many are also the largest and brightest objects outside of the Milky Way, most notably Omega Centauri, 47 Tucanae, and a number of famed night-sky targets

(e.g., Hercules/M13). The GCs have mid-IR color properties that are similar to spheroidal galaxies; indeed, Omega Centauri is essentially this type of object, indicative of their dominant evolved stellar populations.

Appendix A
Total Fluxes: Large-aperture and Radial Profile Fitting Photometry

This appendix is comprised of Table 6 that lists the "total" fluxes for the 100 largest galaxies and LG galaxies detected by

Table 6
Asymptotic and Total Integrated Brightness

iS	Galaxy	$R_{W1}\ A_{W1} \pm \Delta$ (arcmin mag mag)	$R_{W2}\ A_{W2} \pm \Delta$ (arcmin mag mag)	$R_{W3}\ A_{W3} \pm \Delta$ (arcmin mag mag)	$R_{W4}\ A_{W4} \pm \Delta$ (arcmin mag mag)	$T_{W1} \pm \Delta$ (mag mag)	$T_{W2} \pm \Delta$ (mag mag)	$T_{W3} \pm \Delta$ (mag mag)	$T_{W4} \pm \Delta$ (mag mag)
(1)	(2)	(3)	(4)	(5)	(6)	(7)	(8)	(9)	(10)
3	M31	149.39 0.08 0.01	132.78 0.13 0.01	148.80 −1.95 0.01	99.38 −3.11 0.01	0.06 0.01	0.10 0.01	−2.00 0.01	−3.13 0.01
4	M33	65.32 3.03 0.01	38.83 3.00 0.01	37.28 −0.17 0.01	30.55 −1.94 0.01	3.08 0.01	3.02 0.01	−0.22 0.01	−2.02 0.01
5	NGC 0253	25.27 3.46 0.01	24.39 3.26 0.01	25.13 −0.55 0.03	25.33 −2.94 0.03	3.46 0.01	3.25 0.01	−0.56 0.03	−2.95 0.03
6	NGC 5128	23.45 2.99 0.01	23.36 2.98 0.01	9.08 0.41 0.01	8.32 −1.29 0.01	2.98 0.01	2.97 0.01	0.44 0.01	−1.26 0.01
7	NGC 0055	23.36 5.42 0.01	23.31 5.33 0.01	18.76 2.80 0.01	18.66 0.29 0.01	5.43 0.01	5.30 0.02	2.70 0.03	0.22 0.02
8	M81	16.57 3.60 0.01	16.97 3.60 0.01	10.34 1.82 0.03	10.61 0.44 0.03	3.60 0.01	3.59 0.01	1.79 0.03	0.35 0.03
9	M101	13.01 5.22 0.01	13.62 5.10 0.01	10.38 1.61 0.01	10.28 −0.30 0.01	5.19 0.01	5.03 0.02	1.56 0.02	−0.38 0.02
10	NGC 4945	15.49 4.06 0.01	14.72 3.87 0.01	12.76 0.31 0.01	13.70 −1.57 0.01	4.06 0.01	3.86 0.01	0.30 0.01	−1.58 0.01
11	IC 0342	15.48 3.95 0.01	15.42 3.88 0.01	11.40 0.22 0.01	10.96 −1.83 0.01	3.93 0.01	3.85 0.01	0.09 0.03	−1.84 0.01
12	NGC 1316	15.21 5.06 0.01	12.80 5.11 0.01	8.32 4.27 0.01	4.05 3.18 0.02	5.06 0.01	5.10 0.01	4.36 0.03	3.13 0.05
13	M49	15.03 4.94 0.01	12.71 5.03 0.01	9.75 4.04 0.02	3.10 3.82 0.03	4.94 0.01	5.03 0.01	4.17 0.10	3.74 0.09
14	M86	14.23 5.45 0.01	11.85 5.52 0.01	5.87 5.43 0.02	2.08 4.99 0.06	5.45 0.01	5.51 0.02	5.70 0.05	4.92 0.10
15	Maffei 1	13.82 3.91 0.01	12.32 3.93 0.02	7.05 3.22 0.02	2.54 2.68 0.01	3.90 0.01	3.92 0.02	3.26 0.08	2.50 0.13
16	M110	13.53 5.29 0.01	12.06 5.36 0.01	12.12 4.57 0.02	12.12 3.16 0.07	5.28 0.01	5.35 0.01	4.48 0.08	3.25 0.08
17	M104	13.05 4.60 0.01	11.05 4.64 0.01	9.30 3.54 0.01	4.36 2.53 0.02	4.60 0.01	4.62 0.01	3.63 0.02	2.42 0.03
18	NGC 2403	13.11 5.67 0.01	12.95 5.57 0.01	12.77 2.25 0.01	10.92 0.28 0.01	5.66 0.01	5.53 0.02	2.21 0.02	0.19 0.02
19	NGC 0247	13.02 6.45 0.01	12.88 6.49 0.01	12.91 4.04 0.01	12.16 2.27 0.03	6.44 0.01	6.42 0.02	3.85 0.06	2.08 0.08
20	M106	12.52 5.22 0.01	11.95 5.18 0.01	9.93 2.75 0.01	10.57 1.09 0.01	5.22 0.01	5.16 0.01	2.68 0.02	1.00 0.03
21	M87	12.39 5.29 0.01	10.38 5.41 0.01	6.75 4.75 0.02	2.22 3.79 0.02	5.28 0.01	5.41 0.01	4.96 0.06	3.73 0.08
22	NGC 3628	12.02 5.75 0.01	10.21 5.62 0.01	9.79 2.42 0.01	9.78 0.50 0.01	5.74 0.01	5.61 0.01	2.39 0.02	0.46 0.02
23	NGC 0300	11.91 5.70 0.01	11.43 5.72 0.01	9.93 3.13 0.01	12.00 1.27 0.02	5.69 0.01	5.65 0.02	Null Null	Null Null
24	NGC 4736	11.37 4.75 0.01	9.67 4.74 0.01	7.34 2.03 0.01	7.47 0.32 0.01	4.75 0.01	4.74 0.02	1.99 0.01	0.28 0.02
25	NGC 6822	11.41 5.73 0.01	11.38 5.76 0.01	11.40 3.41 0.01	11.07 1.13 0.02	5.71 0.02	5.66 0.03	3.36 0.09	1.13 0.11
26	NGC 1532	11.28 6.42 0.01	9.38 6.38 0.01	8.85 3.58 0.01	8.85 1.97 0.02	6.42 0.01	6.37 0.01	3.52 0.04	1.90 0.04
27	NGC 5236	10.53 4.24 0.01	9.52 4.12 0.01	10.94 0.32 0.01	9.27 −1.86 0.01	4.24 0.01	4.11 0.01	0.31 0.01	−1.88 0.01
28	NGC 0147	11.12 6.50 0.01	9.30 6.57 0.01	9.02 4.55 0.01	Null Null Null	6.47 0.02	6.52 0.05	Null Null	Null Null
29	NGC 6744	10.77 5.47 0.01	10.88 5.45 0.01	8.94 2.27 0.01	10.02 0.68 0.01	5.47 0.01	5.44 0.01	2.12 0.04	0.58 0.03
30	M63	10.36 5.25 0.01	9.94 5.19 0.01	10.17 1.87 0.01	9.89 0.24 0.01	5.24 0.01	5.16 0.01	1.85 0.01	0.20 0.02
31	NGC 1553	10.41 5.85 0.01	8.69 5.95 0.01	5.72 5.19 0.01	2.69 4.24 0.02	5.87 0.01	5.96 0.01	5.26 0.02	4.13 0.05
32	NGC 1399	10.23 5.80 0.01	8.68 5.90 0.01	6.00 5.28 0.02	2.45 4.77 0.04	5.80 0.01	5.88 0.01	5.51 0.04	4.69 0.06
33	NGC 4236	10.36 7.84 0.01	10.32 7.94 0.01	10.38 5.93 0.03	10.35 3.06 0.04	7.81 0.02	7.80 0.05	5.67 0.09	Null Null
34	NGC 4565	10.01 5.75 0.01	9.73 5.71 0.01	10.19 3.19 0.01	10.23 1.63 0.01	5.75 0.01	5.70 0.01	3.15 0.02	1.58 0.02
35	Maffei 2	10.12 4.74 0.01	9.99 4.57 0.01	10.04 1.05 0.01	10.15 −1.06 0.01	4.74 0.01	4.57 0.01	1.01 0.02	−1.07 0.01
36	NGC 4631	9.88 5.99 0.01	9.41 5.80 0.01	9.92 1.98 0.01	9.72 −0.07 0.01	5.99 0.01	5.78 0.01	1.96 0.01	−0.10 0.01
37	M60	9.69 5.37 0.01	8.18 5.42 0.01	6.31 4.33 0.02	2.59 3.85 0.04	5.36 0.01	5.41 0.02	4.76 0.11	3.77 0.12
38	NGC 4636	9.59 6.05 0.01	8.04 6.13 0.01	6.47 5.00 0.02	1.98 4.69 0.05	6.04 0.01	6.11 0.01	5.11 0.13	4.78 0.17
39	NGC 2768	9.52 6.74 0.01	7.97 6.77 0.01	5.90 6.20 0.03	2.15 5.50 0.06	6.72 0.01	6.76 0.02	6.45 0.07	5.41 0.09
40	NGC 3585	9.43 6.26 0.01	7.97 6.35 0.01	5.70 5.74 0.03	1.61 5.28 0.07	6.25 0.01	6.34 0.02	5.90 0.07	5.10 0.08
41	ESO 270-G017	9.52 8.41 0.01	7.96 8.51 0.01	7.26 6.10 0.02	7.26 3.91 0.04	8.36 0.03	8.45 0.08	6.09 0.10	3.85 0.07
42	M51a	9.22 5.07 0.01	9.09 4.96 0.01	9.09 1.18 0.01	8.98 −0.62 0.01	5.08 0.01	4.94 0.01	1.16 0.01	−0.65 0.01
43	NGC 3115	9.06 5.58 0.01	7.67 5.60 0.01	5.68 4.55 0.01	1.88 4.52 0.03	5.58 0.01	5.59 0.02	4.68 0.08	4.49 0.04
44	NGC 3923	9.15 5.95 0.01	7.66 6.07 0.01	5.91 5.43 0.03	1.58 5.29 0.07	5.95 0.01	6.06 0.02	5.93 0.09	5.16 0.09
45	NGC 4365	8.92 6.25 0.01	7.54 6.38 0.01	1.25 6.75 0.01	1.02 5.77 0.05	6.24 0.01	6.38 0.02	6.75 0.03	5.56 0.12
46	NGC 1313	8.91 6.68 0.01	8.93 6.62 0.01	8.96 3.44 0.01	8.96 0.98 0.01	6.66 0.01	6.57 0.02	3.35 0.05	0.90 0.04
47	M84	8.93 5.71 0.01	7.45 5.76 0.01	4.68 5.42 0.02	1.56 4.77 0.05	5.70 0.01	5.79 0.01	5.64 0.04	4.72 0.09

Table 6
(Continued)

iS	Galaxy	R_{W1} A_{W1} $\pm$ Δ (arcmin mag mag)	R_{W2} A_{W2} $\pm$ Δ (arcmin mag mag)	R_{W3} A_{W3} $\pm$ Δ (arcmin mag mag)	R_{W4} A_{W4} $\pm$ Δ (arcmin mag mag)	T_{W1} $\pm$ Δ (mag mag)	T_{W2} $\pm$ Δ (mag mag)	T_{W3} $\pm$ Δ (mag mag)	T_{W4} $\pm$ Δ (mag mag)
(1)	(2)	(3)	(4)	(5)	(6)	(7)	(8)	(9)	(10)
48	NGC 0185	8.92 6.19 0.01	7.44 6.27 0.01	5.84 5.25 0.02	2.47 4.55 0.04	6.16 0.02	6.26 0.02	5.36 0.03	4.38 0.08
49	NGC 6946	8.84 5.00 0.01	8.88 4.82 0.01	7.96 0.94 0.01	8.71 −1.04 0.01	5.00 0.01	4.80 0.01	0.93 0.01	−1.07 0.01
50	NGC 1395	8.88 6.43 0.01	7.43 6.51 0.01	5.67 5.85 0.02	1.52 5.37 0.07	6.42 0.01	6.51 0.02	6.24 0.06	5.28 0.10
51	IC 0010	8.73 5.08 0.01	8.38 5.01 0.01	5.53 2.28 0.01	4.62 −0.35 0.01	5.07 0.01	5.01 0.01	2.30 0.01	−0.35 0.01
52	NGC 4517	8.57 7.07 0.01	8.55 6.98 0.01	8.64 3.89 0.01	8.61 2.10 0.02	7.07 0.01	6.96 0.01	3.84 0.03	2.02 0.02
53	NGC 1291	8.62 5.34 0.01	8.65 5.39 0.01	6.22 4.29 0.01	8.09 3.09 0.05	5.33 0.01	5.37 0.01	4.20 0.06	3.02 0.10
54	NGC 2683	8.40 6.13 0.01	7.46 6.08 0.01	7.47 3.77 0.01	3.88 2.56 0.01	6.13 0.01	6.06 0.01	3.73 0.02	2.56 0.03
55	NGC 4697	8.51 5.98 0.01	7.12 6.05 0.01	4.98 5.50 0.02	1.58 4.72 0.04	5.96 0.01	6.03 0.02	5.83 0.06	4.61 0.14
56	NGC 3521	8.39 5.43 0.01	7.13 5.35 0.01	5.87 1.96 0.01	5.90 0.31 0.01	5.42 0.01	5.35 0.01	1.94 0.01	0.27 0.02
57	NGC 3109	8.50 7.93 0.01	8.49 7.95 0.01	8.26 6.63 0.05	Null Null Null	7.89 0.03	7.80 0.05	Null Null	Null Null
58	NGC 0891	8.27 5.50 0.01	8.43 5.29 0.01	8.49 1.95 0.01	8.47 0.22 0.01	5.50 0.01	5.29 0.01	1.93 0.01	0.19 0.01
59	M85	8.43 5.78 0.01	7.08 5.82 0.01	5.33 5.29 0.02	2.07 4.41 0.04	5.77 0.01	5.81 0.01	5.45 0.05	4.36 0.10
60	NGC 4244	8.47 7.48 0.01	8.45 7.43 0.01	8.46 5.32 0.01	7.52 3.26 0.03	7.47 0.01	7.39 0.03	5.18 0.05	3.11 0.07
61	NGC 4762	8.41 7.09 0.01	7.09 7.14 0.01	5.18 6.43 0.03	1.92 5.98 0.10	7.09 0.01	7.12 0.02	6.73 0.07	5.88 0.09
62	NGC 5084	8.13 6.81 0.01	8.15 6.83 0.01	8.22 5.41 0.02	8.15 3.93 0.08	6.80 0.01	6.79 0.02	5.44 0.09	4.08 0.08
63	NGC 5907	7.91 6.46 0.01	8.04 6.34 0.01	8.05 3.22 0.01	8.03 1.55 0.01	6.46 0.01	6.34 0.01	3.20 0.01	1.52 0.02
64	NGC 4395	8.04 7.70 0.01	8.02 7.73 0.01	7.98 5.43 0.03	7.77 2.99 0.05	7.67 0.02	7.58 0.07	5.34 0.09	2.97 0.11
65	NGC 1407	7.92 6.19 0.01	6.61 6.28 0.01	5.28 5.55 0.03	1.53 5.38 0.08	6.18 0.01	6.27 0.02	5.95 0.09	5.25 0.10
66	NGC 3627	7.83 5.55 0.01	6.56 5.45 0.01	6.14 2.02 0.01	6.15 0.01 0.01	5.54 0.01	5.44 0.01	2.00 0.01	−0.02 0.02
67	NGC 4438	7.76 6.77 0.01	6.58 6.77 0.01	5.53 5.03 0.01	2.23 3.78 0.02	6.76 0.01	6.71 0.02	5.20 0.05	3.73 0.05
68	NGC 1365	7.79 6.03 0.01	7.43 5.74 0.01	7.65 2.11 0.01	7.40 −0.46 0.01	6.02 0.01	5.73 0.01	2.09 0.01	−0.48 0.01
69	NGC 2903	7.57 5.66 0.01	7.75 5.57 0.01	7.70 2.06 0.01	7.68 0.09 0.01	5.66 0.01	5.56 0.01	2.03 0.01	0.05 0.02
70	NGC 5846	7.68 6.38 0.01	6.45 6.47 0.01	4.59 6.08 0.03	1.41 5.69 0.07	6.36 0.01	6.47 0.03	6.37 0.08	5.52 0.10
71	NGC 4725	7.67 6.07 0.01	6.46 6.12 0.01	5.22 3.99 0.01	4.09 2.60 0.02	6.06 0.01	6.11 0.01	3.90 0.02	2.50 0.03
72	NGC 1549	7.66 6.33 0.01	6.80 6.43 0.01	5.63 5.64 0.01	2.27 5.16 0.04	6.33 0.01	6.41 0.01	5.90 0.08	5.04 0.07
73	WLM	7.70 8.85 0.01	7.68 8.93 0.02	7.69 8.17 0.22	4.97 5.36 0.17	8.79 0.03	8.75 0.07	Null Null	Null Null
74	NGC 2841	7.68 5.88 0.01	6.33 5.89 0.01	4.68 3.78 0.01	5.90 2.17 0.02	5.87 0.01	5.88 0.01	3.74 0.01	2.10 0.03
75	Circinus Galaxy	7.62 4.39 0.01	7.61 3.74 0.01	11.02 −0.31 0.04	10.28 −2.59 0.04	4.37 0.02	3.73 0.01	−0.31 0.04	−2.60 0.04
76	NGC 3621	7.58 6.32 0.02	6.32 6.18 0.02	6.24 2.55 0.01	6.24 0.83 0.01	6.31 0.02	6.15 0.02	2.52 0.01	0.78 0.02
77	NGC 5078	7.56 6.69 0.01	6.32 6.65 0.01	4.59 4.00 0.01	3.26 2.44 0.01	6.68 0.01	6.64 0.01	4.01 0.01	2.40 0.02
78	NGC 1023	7.53 6.03 0.01	6.27 6.09 0.01	3.69 5.62 0.02	1.92 4.93 0.05	6.03 0.01	6.09 0.01	5.72 0.07	4.78 0.08
79	NGC 7331	7.45 5.69 0.01	7.21 5.60 0.01	7.25 2.35 0.01	7.18 0.66 0.01	5.69 0.01	5.59 0.01	2.33 0.01	0.62 0.01
80	M64	7.18 5.18 0.01	6.14 5.17 0.01	5.95 2.95 0.01	5.96 1.19 0.01	5.18 0.01	5.17 0.01	2.91 0.02	1.15 0.02
81	M59	7.21 6.43 0.01	6.11 6.51 0.01	4.53 5.31 0.02	1.73 5.09 0.07	6.42 0.01	6.51 0.02	5.41 0.12	5.06 0.07
82	NGC 4696	7.18 6.64 0.01	6.05 6.70 0.01	5.09 5.92 0.02	1.94 5.37 0.06	6.63 0.01	6.69 0.01	6.35 0.09	5.32 0.14
83	M82	6.92 4.06 0.01	6.82 3.61 0.01	9.00 −0.96 0.01	8.81 −4.14 0.01	4.06 0.01	3.61 0.01	−0.97 0.01	−4.14 0.01
84	ESO 274-001	7.07 7.82 0.01	7.07 7.85 0.01	3.29 6.36 0.03	3.38 3.01 0.01	7.77 0.33	7.77 0.09	6.65 0.09	2.98 0.02
85	M77	6.60 4.59 0.01	5.01 2.89 0.01	6.94 −0.68 0.04	7.33 −2.45 0.04	4.59 0.01	2.89 0.01	−0.68 0.04	−2.45 0.04
86	NGC 3077	6.95 6.77 0.01	5.84 6.71 0.01	4.53 3.98 0.01	3.16 1.61 0.01	6.76 0.01	6.69 0.02	4.00 0.02	1.58 0.02
87	M65	6.95 5.89 0.01	5.88 5.91 0.01	5.85 4.14 0.01	5.88 2.74 0.03	5.89 0.01	5.90 0.01	4.09 0.02	2.64 0.04
88	NGC 7213	6.91 6.46 0.01	5.82 6.41 0.01	4.02 4.23 0.01	2.64 2.42 0.01	6.45 0.01	6.41 0.02	4.26 0.02	2.38 0.07
89	IC 0356	6.74 5.76 0.01	5.92 5.76 0.01	3.09 3.74 0.01	5.96 1.91 0.02	5.74 0.01	5.75 0.01	3.56 0.02	1.81 0.04
90	NGC 1560	6.90 8.56 0.01	5.82 8.69 0.01	3.03 7.15 0.05	1.88 5.35 0.04	8.55 0.01	8.67 0.02	Null Null	Null Null
91	NGC 2663	6.90 6.22 0.01	6.00 6.32 0.01	5.06 5.86 0.03	1.43 4.90 0.04	6.21 0.01	6.29 0.02	6.30 0.04	4.83 0.04
92	NGC 4216	6.92 6.36 0.01	5.73 6.37 0.01	5.62 4.22 0.01	5.30 2.89 0.02	6.35 0.01	6.36 0.01	4.16 0.02	2.78 0.03
93	NGC 1055	6.79 6.74 0.01	6.49 6.63 0.01	6.82 3.06 0.01	6.77 1.30 0.01	6.74 0.01	6.60 0.01	3.04 0.01	1.27 0.02
94	NGC 5170	6.73 7.42 0.01	5.67 7.40 0.01	5.68 5.21 0.01	5.19 3.79 0.03	7.41 0.01	7.39 0.01	5.14 0.03	3.61 0.04
95	M98	6.62 6.70 0.01	6.69 6.66 0.01	6.77 3.81 0.01	6.73 2.19 0.02	6.70 0.01	6.64 0.01	3.77 0.02	2.11 0.03
96	NGC 2997	6.73 6.13 0.01	6.54 6.02 0.01	6.57 2.34 0.01	6.74 0.53 0.01	6.13 0.01	6.00 0.01	2.30 0.01	0.48 0.02
97	NGC 4125	6.68 6.48 0.01	5.62 6.55 0.01	3.89 5.98 0.02	1.42 5.20 0.04	6.48 0.01	6.54 0.01	6.10 0.05	5.00 0.07
98	NGC 7793	6.72 6.50 0.01	6.62 6.41 0.01	5.99 3.21 0.01	4.68 1.54 0.01	6.50 0.01	6.38 0.01	3.16 0.01	1.47 0.02
99	NGC 5363	6.65 6.55 0.01	5.60 6.58 0.01	3.55 5.46 0.01	1.79 4.30 0.03	6.54 0.01	6.56 0.02	5.57 0.03	4.23 0.07
100	NGC 4217	6.69 7.21 0.01	5.60 7.05 0.01	5.01 3.72 0.01	5.02 2.05 0.01	7.20 0.01	7.05 0.01	3.71 0.01	2.04 0.02
101	IC 1613	5.62 8.35 0.01	5.56 8.59 0.02	2.53 8.31 0.12	Null Null Null	8.26 0.06	8.41 0.09	Null Null	Null Null
102	M32	4.32 5.01 0.01	3.56 5.07 0.01	3.49 4.42 0.01	1.90 3.57 0.03	5.01 0.01	5.06 0.01	4.37 0.02	3.49 0.04
103	UGC 05373	3.46 9.65 0.01	2.92 9.66 0.02	Null Null Null	2.11 6.39 0.33	9.57 0.04	9.56 0.09	Null Null	Null Null
104	ESO 245-007	2.61 10.88 0.02	2.61 11.12 0.04	Null Null Null	Null Null Null	10.53 0.10	Null Null	Null Null	Null Null

Note. Columns: (1) order of *W1* 3.4 μm isophotal angular size, see Table 1; (2) galaxy name; (3)–(6) *W1, W2, W3,* and *W4*, respectively, asymptotic measurements (radius (in arcmin) and magnitude and its uncertainty); (7)–(10) total magnitude and its uncertainty (*W1, W2, W3,* and *W4,* respectively) estimated using a double Sérsic fit to the radial surface brightness profile.

(This table is available in machine-readable form.)

WISE (except the Magellanic Clouds). Two methods are used to estimate total fluxes: large asymptotic apertures from curve-of-growth measurements and double Sérsic function fitting to the axisymmetric radial profile. The method and results are described in Section 4.1, with some statistical comparison results presented in Table 2.

Appendix B
SEDs of Classic Galaxy Types

Four examples of galaxies that represent the *WISE* color sets (Figure 19) are spheroids, intermediate SF, active SF disks, and AGN-dominated. The SEDs are constructed from 2MASS XSC and *WISE* global measurements and templates that best fit the data. Since these Brown et al. (2014b) templates have real mid-infrared spectral data from *Spitzer*-IRS, they are accurate

representations of the emission and continuum features. Also indicated are the *WISE* relative system response curves (RSRs), here normalized to unity for easy comparison. Note that the actual throughput quantum efficiency is significantly different, with *W1* the most sensitive band, followed closely by *W2*, and the long wave bands considerably less sensitive (Jarrett et al. 2011). The 12 μm *W3* detector, however, makes up for less sensitivity by having a very wide band, enclosing molecular emission and dust continuum components.

Appendix C
Data Products of the WXSC

Images. The foundation of the WXSC is the native-resolution mosaics, constructed specifically for resolved galaxies. For each galaxy, the images range in size from
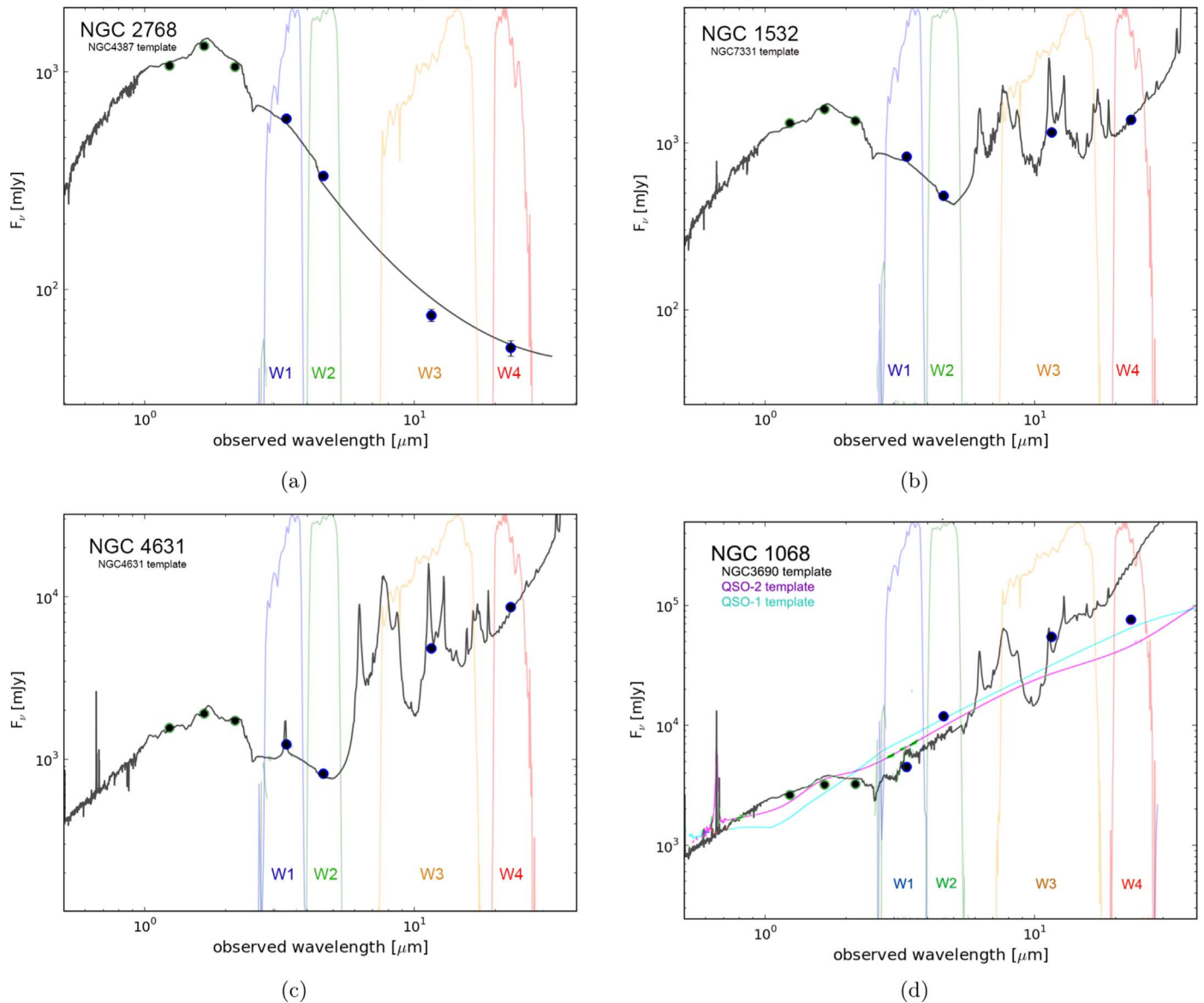
Figure 19. Infrared SEDs of four galaxies, demonstrating the broad classification revealed by *WISE* colors. (a) The first is a typical early-type elliptical galaxy, stellar bulge–dominated; (b) the second is an intermediate (Sb) galaxy; (c) the third is a late-type (Sd), SF-dominated spiral; and (d) the last demonstrates an AGN-dominated host galaxy. The data points are global measurements from 2MASS XSC and *WISE* (this study). The "template" is a best fit to the data from the Brown et al. (2014b) and GRASIL (cSil98) suite of spectral templates. The *WISE* filter bands (normalized to unity) are indicated for each.
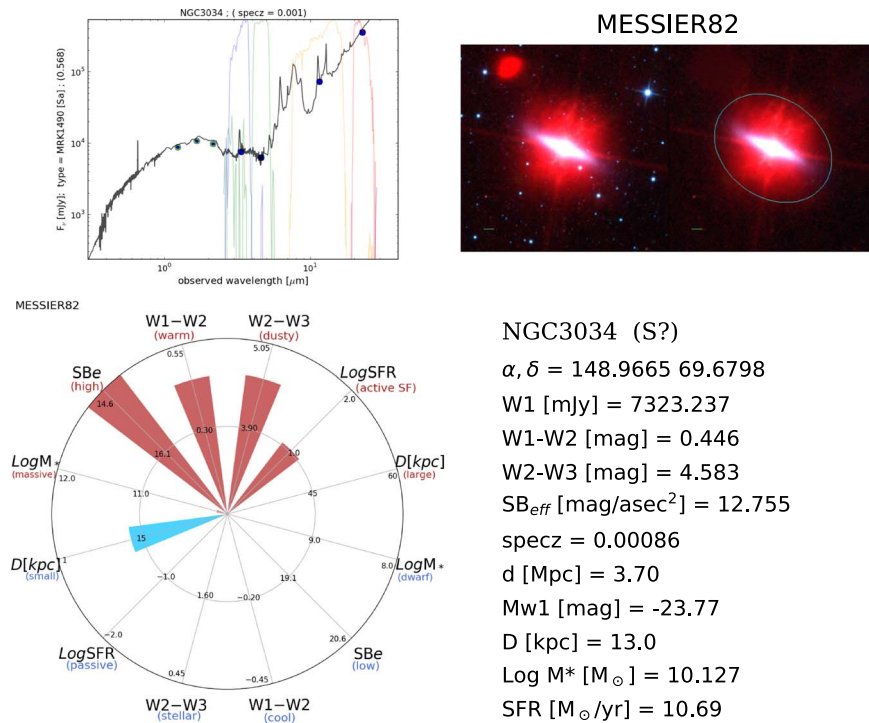
Figure 20. Physical properties of starburst NGC 3034 (M82). The image shows the *WISE* view before/after star subtraction. The ellipse denotes the $1 - \sigma_{sky}$ isophote aperture. The SED includes the four *WISE* band measurements, three 2MASS measurements, and best-fit galaxy template.

$0°\!.25$ to many degrees (e.g., LG galaxies), large enough to encompass the galaxy and its local environment. The pixel scale is $1''$, except for the Magellanic Clouds ($8''$) and M31 ($1''\!.5$). The flux calibration is in the Vega system, and the zero-point magnitude is in the FITS header. The orientation is standard, and the headers have full WCS information.

There are four bands of *WISE*, and for each band, we construct three kinds of images: the integrated signal (INT), the corresponding uncertainty (UNC), and the frame coverage (COV).

Processing includes identification and removal of foreground stars, background galaxies, and neighboring (satellite) galaxies, as well as the (rare) artifact or image glitch. These "cleaned" images are also part of the available data products and used to measure and study the target galaxy.

Photometry and cataloged values. Full source characterization is carried out on the cleaned images, featuring size, shape, integrated fluxes, surface brightness, and a number of other measurements. A README detailing the catalog columns is part of the data release. For those galaxies with a distance (either redshift-independent or a redshift-based luminosity distance), physical attributes (luminosities, SFRs, stellar mass) are derived from *k*-corrected fluxes. The *k*-correction is carried

out using templates and SED fitting (see Jarrett et al. 2017 for more details). Likewise, there is a README file that details the physical values in a separate "derived" catalog.

Ancillary products. The images and catalogs are the primary data products, but there are a number of other useful products. Three-color (RGB) images of the WXSC galaxies show the before and after star removal SEDs where the flux data are plotted and compared with the best-fit SED template, and the pinwheel diagrams (see Figure 20) graphically show the physical attributes of the galaxy with respect to the mean values of the greater WXSC sample (Table 4).

Appendix D
Three-color Images of the Largest Galaxies

The 100 largest galaxies in WISE are shown Figures 21–25, row by row in order of angular extent. The blue, green, and red colors represent *W1, W2,* and *W3* bands, respectively, and indicate the host galaxy emission is dominated by old stars (appearing blue), active star formation (appearing red), or combinations between. The angular scale of each image is specified by the one-arcminute green line in the lower left corner.
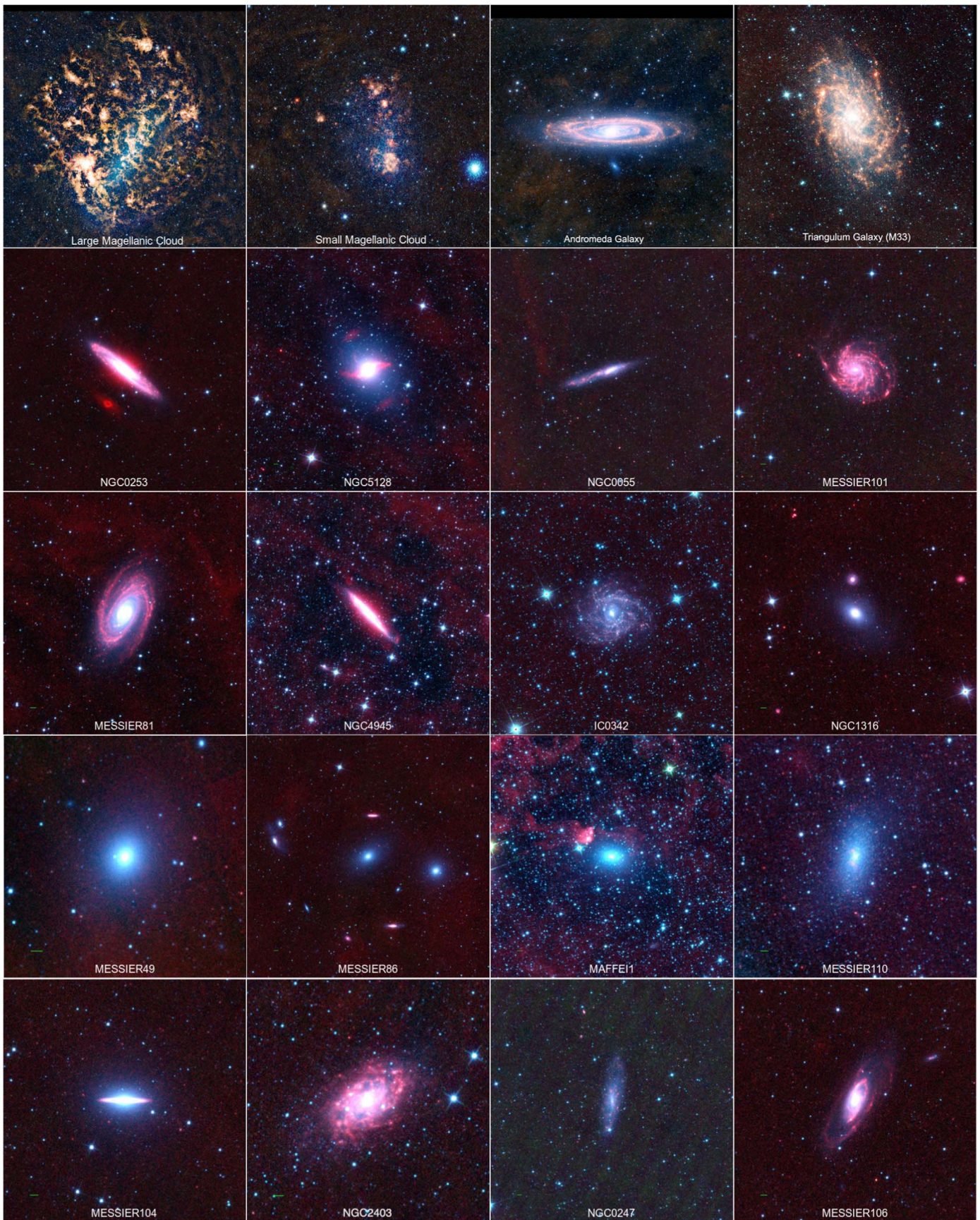
Figure 21. Color combination of the *W1*, *W2*, and *W3* bands. Assigning the blue (*W1*) and green (*W2*) renders the stellar-dominated light as having a blue–cyan hue. Assigning red to *W3* highlights the star formation sites, appearing as yellow–orange–red. Sources that have strong AGN emission will have strong *W2* relative to *W1* and hence appear yellow/green. In the lower left corner, the green line specifies 1′ in scale.
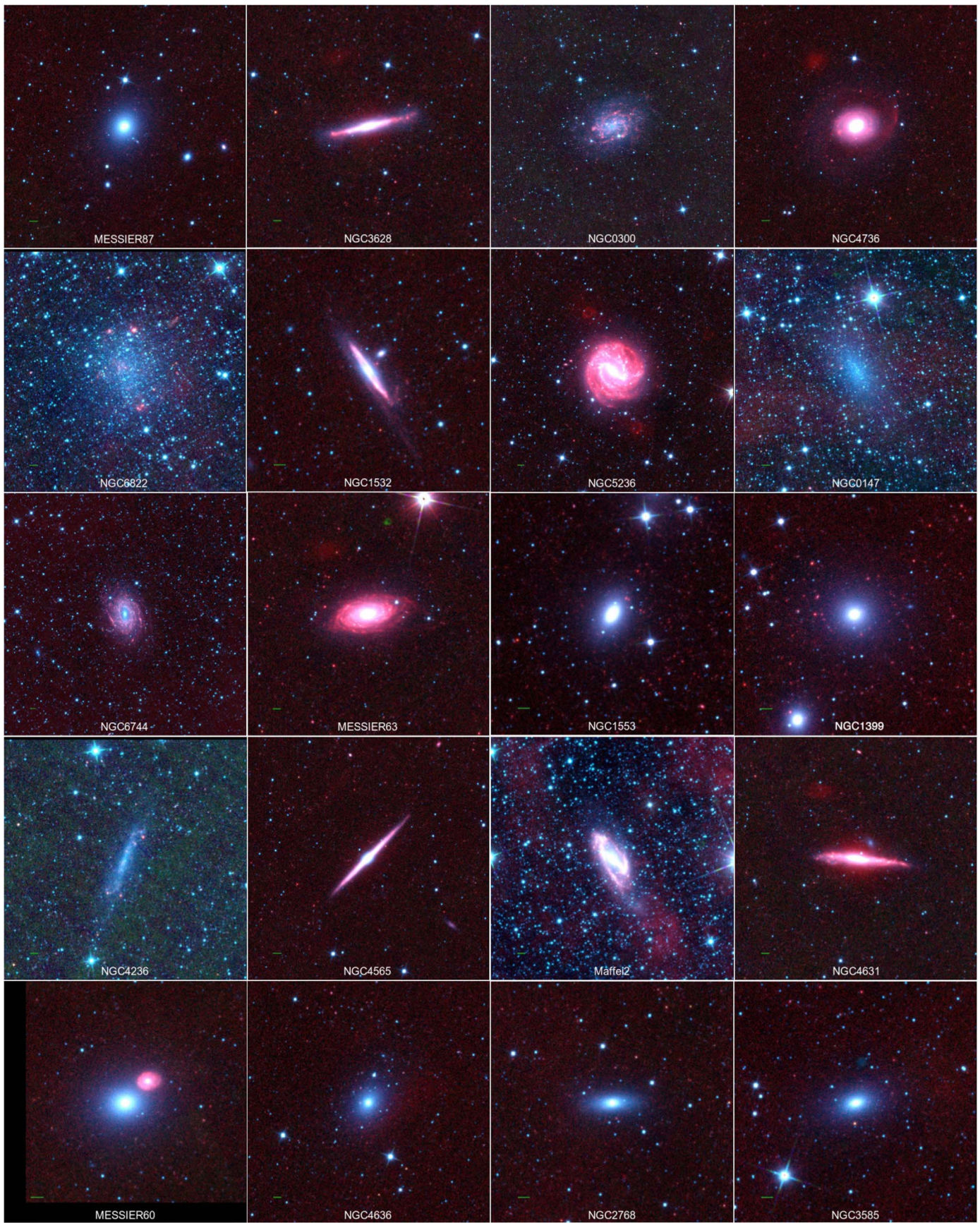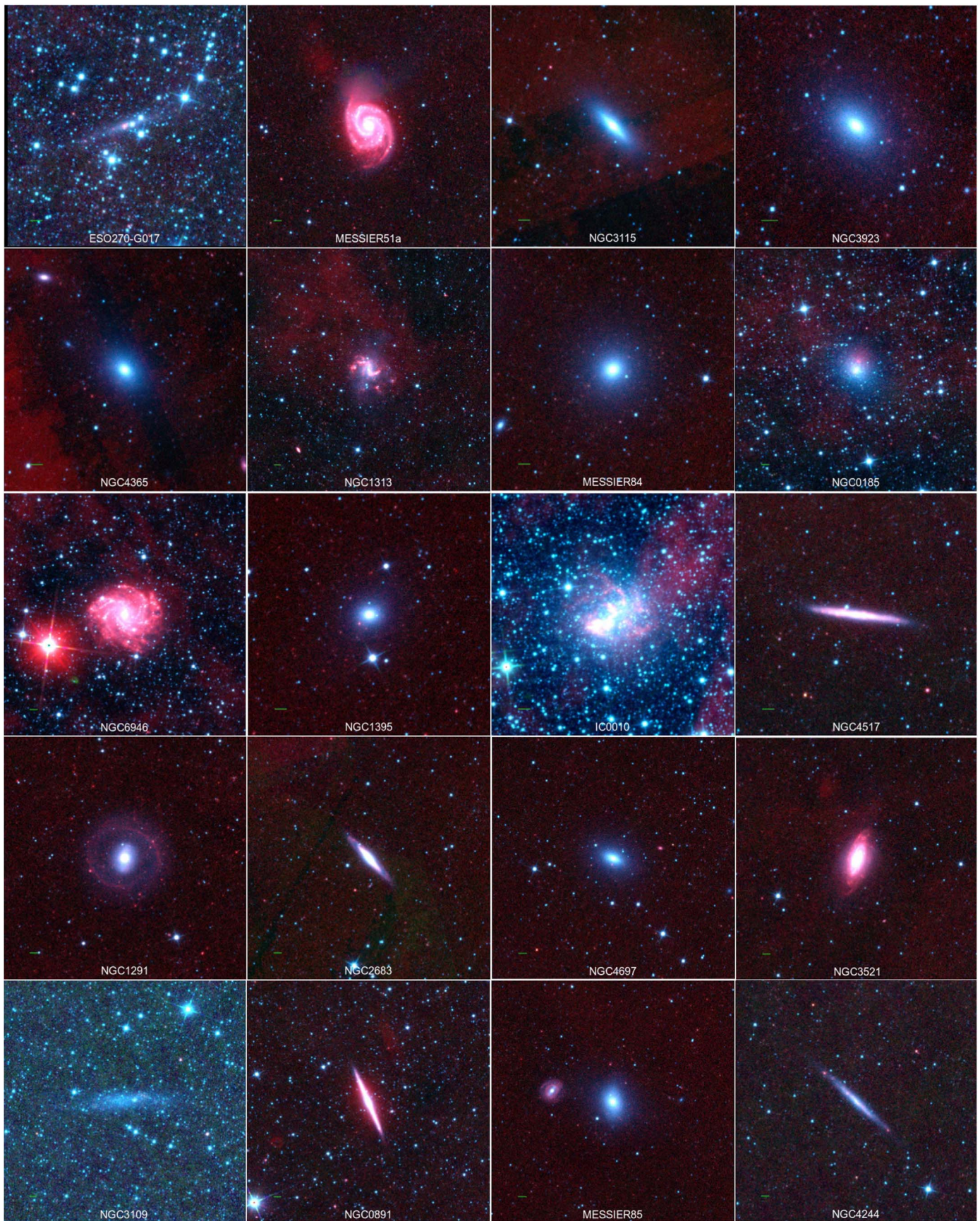
33

Figure 22. See Figure 21 for details.

Figure 23. See Figure 21 for details.
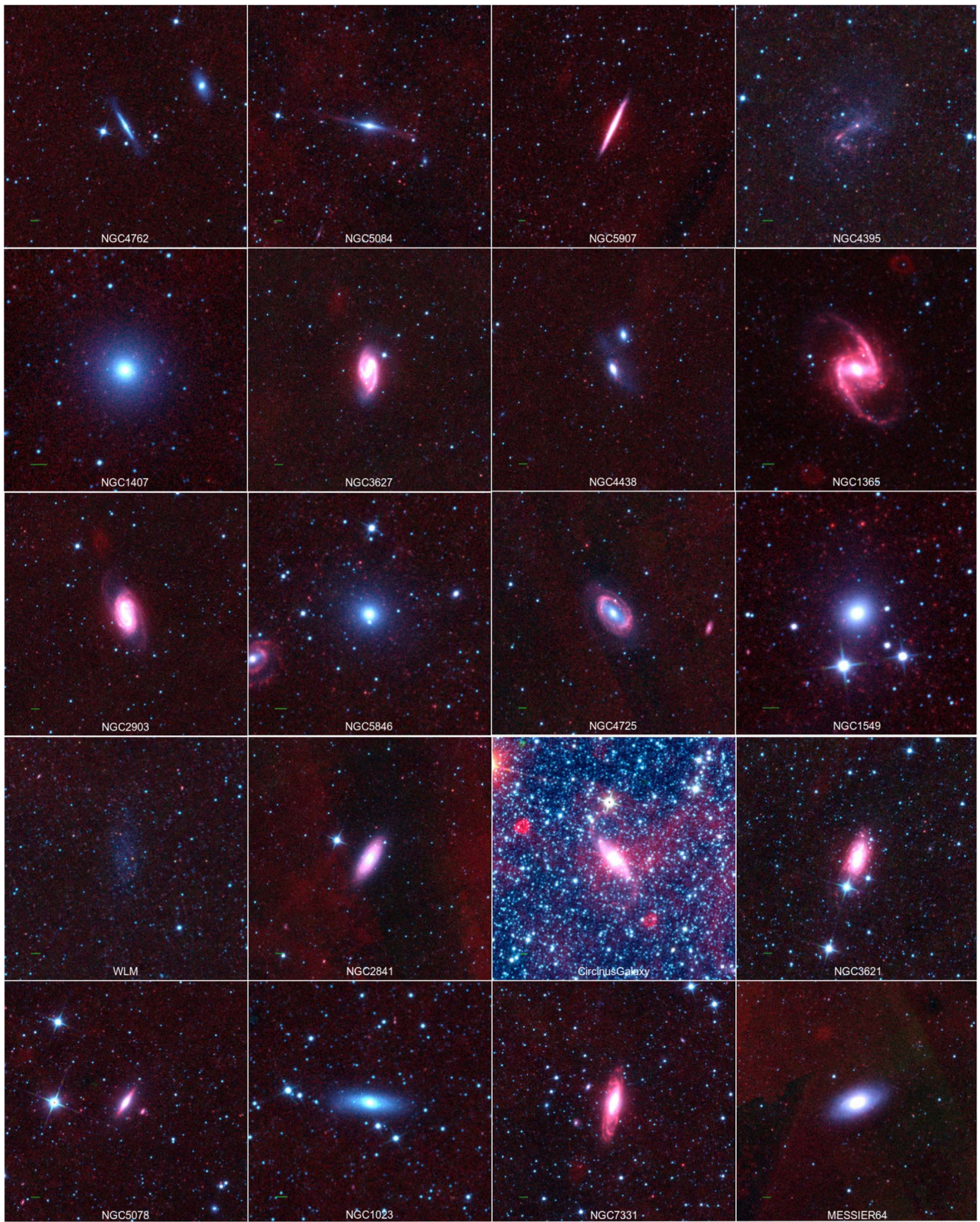
Figure 24. See Figure 21 for details.
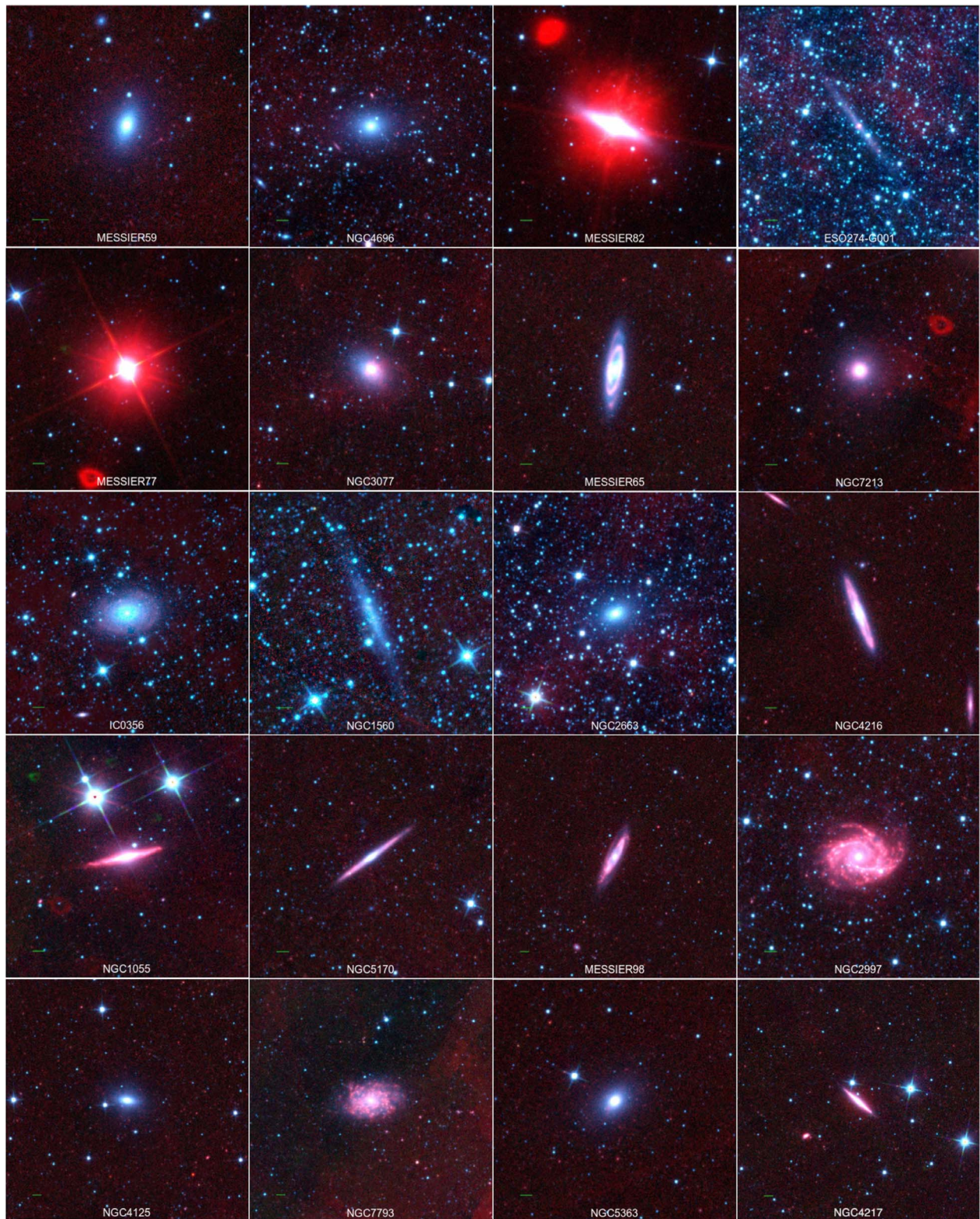
Figure 25. See Figure 21 for details.

ORCID iDs

T. H. Jarrett ⓘ https://orcid.org/0000-0002-4939-734X
M. E. Cluver ⓘ https://orcid.org/0000-0002-9871-6490
M. J. I. Brown ⓘ https://orcid.org/0000-0002-1207-9137
D. A. Dale ⓘ https://orcid.org/0000-0002-5782-9093
C. W. Tsai ⓘ https://orcid.org/0000-0002-9390-9672
F. Masci ⓘ https://orcid.org/0000-0002-8532-9395

References

Alcaino, G., Liller, W., Alvarado, F., et al. 1997, AJ, 114, 1067
Asabere, B., Horellou, C., Jarrett, T., & Winkler, H. 2016, A&A, 592, 20
Besla, G., Martinez-Delgado, D., van der Marel, R., et al. 2016, ApJ, 825, 20
Bouch'e, N., Dekel, A., Genzel, R., et al. 2010, ApJ, 718, 1001
Brown, M. J. I., Jarrett, T. H., & Cluver, M. E. 2014a, PASA, 31, 49
Brown, M. J. I., Moustakas, J., Smith, J. D., et al. 2014b, ApJS, 22, 18
Chauke, P. 2013, MSc Dissertation, Univ. Cape Town
Ching, J. H. Y., Sadler, E. M., Croom, S. M., et al. 2017, MNRAS, 464, 1306
Cluver, M. E., Appleton, P. N., Ogle, P., et al. 2013, ApJ, 765, 93
Cluver, M. E., Jarrett, T. H., Dale, D., et al. 2017, ApJ, 850, 68
Cluver, M. E., Jarrett, T. H., Hopkins, A. M., et al. 2014, ApJ, 782, 90
Cutri, R. M., Wright, E. L., Conrow, T., et al. 2012, Explanatory Supplement to the WISE All-Sky Data Release Products (Pasadena, CA: IPAC)
da Cunha, E., Hopkins, A. M., Colless, M., et al. 2016, PASA, 34, 47
de Vaucouleurs, G., de Vaucouleurs, A., Corwin, H. G., et al. 1991, Third Reference Catalogue of Bright Galaxies, Vol. I, II, and III (New York: Springer)
Eisenhardt, P., Marocco, F., Fowler, J. W., et al. 2019, arXiv:1908.08902
Elbaz, D., Daddi, E., Le Borgne, D., et al. 2007, A&A, 468, 33
Elson, E. C., Kam, S. Z., Chemin, L., Carignan, C., & Jarrett, T. H. 2019, MNRAS, 483, 931
For, B. Q., Koribalski, B. S., & Jarrett, T. H. 2016, MNRAS, 425, 1934
Hall, C., Courteau, S., Jarrett, Thomas, et al. 2018, ApJ, 865, 154
Heald, G., de Blok, W. J. G., Lucero, D., et al. 2016, MNRAS, 462, 1238
Hopkins, A. M., & Beacom, J. F. 2006, ApJ, 651, 142
Huang, T., Goto, T., Hashimoto, T., et al. 2017, MNRAS, 471, 4239
Jarrett, T. H., Chester, T., Cutri, R., et al. 2000, AJ, 119, 2498
Jarrett, T. H., Chester, T., Cutri, R., et al. 2003, AJ, 125, 525
Jarrett, T. H., Cluver, M. C., Magoulas, C., et al. 2017, ApJ, 836, 182
Jarrett, T. H., Cohen, M., Masci, F., et al. 2011, ApJ, 735, 112
Jarrett, T. H., Masci, F., Tsai, C. W., et al. 2012, AJ, 144, 68
Jarrett, T. H., Masci, F., Tsai, C. W., et al. 2013, AJ, 145, 6

Johnson, K. E., Hibbard, J. E., Gallagher, S. C., et al. 2007, AJ, 134, 1522
Kam, S. Z., Carignan, C., Chemin, L., et al. 2017, AJ, 154, 41
Kennicutt, R. C., Calzetti, D., Aniano, G., et al. 2011, PASP, 123, 1347
Kennicutt, R. C., Jr., Armus, L., Bendo, G., et al. 2003, PASP, 115, 928
Kettlety, T., Hesling, J., Phillipps, S., et al. 2018, MNRAS, 473, 776
Kollmeier, J., Zasowski, G., Rix, H.-W., et al. 2017, arXiv:1711.03234
Konstantopoulos, I. 2015, A&C, 10, 116
Korsaga, M., Carignan, C., Amram, P., Epinat, B., & Jarrett, T. H. 2018, MNRAS, 478, 50
Kroupa, P. 2002, Sci, 295, 82
Lacy, M., Storrie-Lombardi, L. J., Sajina, A., et al. 2004, ApJS, 154, 166
Leroy, A. K., Sandstrom, K. M., Lang, D., et al. 2019, ApJS, 244, 24
Licquia, t., & Newman, J. 2015, ApJ, 806, 96
Lucero, D. M., Carignan, C., Elson, E. C., et al. 2015, MNRAS, 450, 3935
MacLean, B. T., Campbell, S. W., De Silva, G., et al. 2016, MNRAS, 460, L69
Mainzer, A., Bauer, J., Cutri, R. M., et al. 2014, ApJ, 792, 30
Masci, F. 2013, ICORE: Image Co-addition with Optional Resolution Enhancement, Astrophysics Source Code Library, ascl:1302.010
Meidt, S., Schinnerer, E., van de Ven, G., et al. 2014, ApJ, 788, 144
Meidt, S. E., Schinnerer, E., Knapen, J. H., et al. 2012, ApJ, 744, 17
Meixner, M., Gordon, K., Indebetouw, R., et al. 2006, AJ, 132, 2268
Milone, A. P., Marino, A. F., Piotto, G., et al. 2012, ApJ, 745, 27
Mingo, B., Watson, M., Rosen, S., et al. 2016, MNRAS, 462, 2631
Neill, J. D., Seibert, M., Tully, B., et al. 2014, ApJ, 792, 129
Nilsson, P. 1973, UppAn, 6
Noeske, K. G., Weiner, B. J., Faber, S. M., et al. 2007, ApJL, 660, L43
Noyola, E., Gebhardt, K., & Bergmann, M. 2008, ApJ, 676, 1008
Ogle, P., Jarrett, T. H., Lanz, L., et al. 2019, ApJL, 884, L11
Parkash, V., Brown, M. J., Jarrett, T. H., et al. 2019, MNRAS, 485, 3169
Parkash, V., Brown, M. J., Jarrett, T. H., & Bonne, N. J. 2018, ApJ, 864, 40
Peng, Y., Maiolino, R., & Cochrane, R. 2015, Natur, 521, 192
Ponomereva, A. A., Verheijen, M. A. W., Reynier, F., & Bosma, A. 2017, MNRAS, 469, 2387
Querejeta, M., Meidt, S. E., Schinnerer, E., et al. 2015, ApJS, 219, 5
Sheth, K., Regan, M., Hinz, J., et al. 2010, PASP, 122, 1397
Silva, L., Granato, G. L., Bressan, A., & Danese, L. 1998, ApJ, 509, 103
Stern, D., Assef, R. J., Benford, D. J., et al. 2012, ApJ, 753, 30
Taylor, E. N., Hopkins, A. M., Baldry, I. K., et al. 2011, MNRAS, 418, 1587
Tomicic, N., Ho, I., Kreckel, K., et al. 2019, ApJ, 873, 3
Tsai, C. W., Eisenhard, P. R., Wu, J., et al. 2015, ApJ, 805, 90
Walker, L. M., Johnson, K. E., Gallagher, S. C., et al. 2010, AJ, 140, 1254
Wickramasinghe, T., & Ukwatta, T. N. 2010, MNRAS, 406, 548
Wright, E. L., Eisenhardt, P. R. M., Mainzer, A. K., et al. 2010, AJ, 140, 1868
Yan, L., Donoso, E., Tsai, C.-W., et al. 2013, AJ, 145, 55
Yew, M., Filipovi, M., Roper, Q., et al. 2017, PASA, 35, 15